In presenting this thesis in partial fulfillment of the requirements for an advanced degree at Idaho State University, I agree that the library shall make it freely available for inspection. I further state that permission to download and/or print my thesis for scholarly purposes may be granted by the Dean of the Graduate School, Dean of my academic division, or by the University Librarian. It is understood that any copying or publication of this thesis for financial gain shall not be allowed without my written permission.

Signature _____

Date _____

Mass Movement Monitoring and Susceptibility Mapping Using Unmanned Aerial Systems along Railway Corridors

By

Dana E. Drinkall

A thesis

submitted in partial fulfillment

of the requirements for the degree of

Masters of Science in the Department of Geosciences

Idaho State University

Fall 2022

To the Graduate Faculty:

The members of the committee appointed to examine the thesis of Dana E. Drinkall find it satisfactory and recommend that it be accepted.

_____

Dr. Donna M. Delparte, Major Advisor,

Associate Professor at Idaho State University

Department of Geosciences

_____

Dr. Benjamin Crosby, Committee Member,

Professor and Department Chair of Idaho State University

Department of Geosciences

_____

Dr. Zachery Lifton, Committee Member,

Hazards Geologist at the Idaho Geological Survey

_____

Dr. Paul Bodily, Graduate Faculty Representative

Assistant Professor at Idaho State University

Department of Computer Science

Acknowledgements

I would like to thank Dr. Donna Delparte for her help, patience, and mentorship throughout this project. I would also like to thank my committee, Dr. Zachery Lifton and Dr. Benjamin Crosby for their guidance and support. I give my thanks to Matthew Belt, Dr. Carrie Bottenberg, Dr. James Mahar, and Dr. Di Wu for their help and advice. My family and friends have my heartfelt thanks for their support over the last few years. In addition, thank you to Nicholas Dryer for aid in our fieldwork logistics. This thesis is funded in part by AmericaView under U.S. Geological Survey Grant/Cooperative Agreement No. G18AP00077.

Table of Contents

List of Figures

List of Tables

Abstract

In northern Idaho (USA), landslides along railway transportation corridors pose a threat for derailments and potential for pollution. One such derailment occurred in 2017 along the Moyie River and in 2020 a rockslide caused a train engine to derail into the Kootenai River resulting in diesel fuel contamination. In 2017 and 2021, mass movement sites were flown with Unmanned Aerial Systems (UAS) equipped with LiDAR along the Kootenai River, Moyie River, and Deep Creek in order to: (1) measure mass movement change using a Multiscale Model-to-Model Cloud Comparison (M3C2) and (2) model mass movement susceptibility and characterization along these river corridors with object-based image analysis (OBIA). This study prototypes a methodology for railway companies to map geohazards along railway corridors using repeat LiDAR to facilitate long term monitoring and mitigate future derailments, service interruptions, and environmental contamination.

Keywords: Repeat LiDAR, OBIA, UAS, Landslides, Rockfall

Chapter 1. Introduction

1.1 Background

On average, landslides annually cause around 25 deaths and 3.5 billion dollars of damage a year to infrastructure across the United States (US) (Idaho Office of Emergency Management, 2018; Lifton et al., 2020). The critical infrastructure and transportation routes across the US are at risk to these dangerous and potentially deadly geohazards. In 2020, the United States government recognized the national threat from geohazards by announcing funding of over $971 million to prioritize natural hazard assessment and monitoring and upgrades to scientific facilities and infrastructure within the Department of the Interior and the United States Geological Survey (United States Geological Survey, 2020). Subsequently, the new National Landslide Preparedness Act (P.L.116-323) was enacted on January 5, 2021 and established the USGS National Landslide Hazards Reduction Program (United States Congress). This act intends to save lives and prevent property damage by characterizing and identifying landslide hazards. The National Landslide Preparedness Act includes the USGS 3D elevation program, an initiative to collect high resolution elevation data using Light Detection and Ranging (LiDAR) to help states and local communities across the country plan for and respond to geohazards (Congressional Research Service, 2020).

To address landslide hazards at the state level, the Idaho Department of Transportation recently completed over $15.8 million dollars' worth of landslide mitigation projects along state managed highway transportation corridors from 2013 to 2018 (Idaho Office of Emergency Management, 2018). Furthermore, the Idaho Geological Survey (IGS) is mapping geohazards across the state and has identified landslides along transportation corridors as a serious risk (Lifton et al., 2020; Idaho Geological Survey, 2020). In northern Idaho, for example, landslides

along the Kootenai and tributary river systems are a threat to not only railroad workers but also to the environment and community water supply. In the last few years there have been multiple train derailments in this part of Idaho. One was caused by a mudslide on March 15, 2017 along the Moyie River and another was caused by a rockslide on January 2, 2020 (Hanrahan, 2020; Sokol, 2017). In 2020, a debris flow derailed a train engine into the Kootenai River resulting in diesel fuel contamination of the river (Hanrahan, 2020). This thesis will address how railroad companies and local governments can map and monitor these geohazards along transportation corridors by leveraging high resolution LiDAR datasets. This thesis will demonstrate how analysis of UAS LiDAR can enable effective and efficient monitoring of landslide activity and map landslide susceptibility using examples from active landslide and rockfall sites in northern Idaho.

1.2 Types of Landslides

There are many different types of landslides or mass movements, the general definition given in the USGS Landslide Handbook (2008) is the landform and movement of organic material, soil, and rock in the downslope direction because of gravity. The USGS Landslide Handbook also classifies different types of mass movements depending on the characteristics and mechanics of the slope failure (Table 1). One of the characteristics used to classify a mass movement is the material that is moved, whether earth, debris, or rock. The next step is to classify it based on the type of movement or the mechanics; these categories include flow, spread, fall, slide, and topple (Highland and Bobrowsky, 2008; Varnes, 1978) . *Flows* are a downslope movement that is continuous in nature, with closely spaced, short-lived shear surfaces. *Spreads* are a combination of the subsidence of a ruptured mass of soil or rock into the

softer material beneath as well as the extension of the material mass. A *fall* is when the material either rolls, bounces, or falls downslope after detaching without a lot of shear displacement. Another type of mass movement is a slide. *Slides* require intense shear strain on the surface area where the downslope movement of the rock or soil occurs. A slide can be further divided into either a planar rupture, referred to as a *translational slide* or a *rotational slide* which describes a curved rupture. *Topples* are defined as a displaced mass that rotated forward around an axis below its center of gravity. Any mass movement can be a combination of more than one type (Highland and Bobrowsky, 2008). The two reported landslides at the sites along the Moyie River and Kootenai river were classified as a rockslide and debris flow, respectively (Hanrahan, 2020; Sokol, 2017).

Table 1. Classification of mass movements. Varnes' abbreviated classification of slope movements (Adapted from Varnes, 1978).

Type of Movement		**Debris (Finer Soil)**	**Earth (Coarser Soil)**	**Rock**
Flow		Debris Flow	Earth Flow	Rock Flow
Spread		Debris Spread	Earth Spread	Rock Spread
Fall		Debris Fall	Earth Fall	Rock Fall
Slide	Translational Rotational	Debris Slide	Earth Slide	Rock Slide
Topple		Debris Topple	Earth Topple	Rock Topple

1.3 Factors Influencing Landslide Susceptibility

1.3.1 Lithology

Lithology is a very important parameter to a slope's landslide susceptibility. Competent rocks are commonly less susceptible to mass movement than unconsolidated materials such as alluvium (Sarkar and Kanungo, 2004; Wachal and Hudak, 2000). This is due to the lack of friction and cohesion in unconsolidated materials allowing greater infiltration of water, thereby reducing the shear strength that prevents the movement of rock (Wachal and Hudak, 2000). The surficial deposits at the study area are mostly composed of landslide-prone glacial and alluvial deposits formed along with the Kootenai River (Burmester et al., 2010; McFaddan et al., 2009; Link, 2002). The formation of the Kootenai River and its tributaries began with the Purcell Lobe of the Cordilleran Ice Sheet and its interactions with the Glacial Lake Kootenai, MT and Glacial Lake Purcell, ID. Glacial Lake Kootenai experienced sudden drainage during the Pleistocene, when the Cordilleran Ice Sheet began to retreat and Glacial Lake Kootenai flooded into Glacial Lake Purcell via the Kootenai River. This created the Kootenai River alluvial fan delta where the Kootenai and Purcell Trench converged (Peters, 2012; Peters and Brennand, 2020).

The underlying bedrock geology of the study area consist of the clay-rich Mesoproterozoic Belt-Purcell Supergroup to the east, and the metamorphic and igneous rocks of the Priest River metamorphic core complex and intrusive Mesozoic rocks of the Kaniksu Batholith to the west. The Belt Supergroup contains the Prichard Formation and the Missoula Group as well as Cretaceous intrusions. The Priest River core complex is composed of granitic and metamorphic rock that was exhumed during crustal extension and faulting in the Eocene (Burmester et al., 2010; Peters, 2012; Link, 2002; Doughty and Price, 2000; McFaddan et al., 2009).

1.3.2 Faulting and Seismicity

Eocene faulting in the study area can also lead to high landslide susceptibility in materials with low permeability such as the metamorphic and igneous bedrock. Faulting not only indicates the possibility of seismicity but also the presence of weak, broken, and weathered rock (Sarkar and Kanungo, 2004). The two normal faults dipping east in the Purcell Trench area, the northern and southern Purcell Trench faults, act as a boundary separating the mafic plutons and the Belt Supergroup. These faults mark the boundary of the Priest River metamorphic complex uplift and formed the Purcell Trench basin after preferential erosion by rivers and glaciers. Another fault can be found farther southeast, trending northwest to southeast is a west-dipping thrust fault that lies roughly along the same route as the Moyie River and Kootenai River, suggesting preferential river incision along the thrust fault (Peters, 2012; Link, 2002).

Seismicity is another possible trigger mechanism. There have been some earthquakes in the area linked to the nearby faults. According to the Idaho Bureau of Homeland Security (2005), there have been three earthquakes above a 2.5 magnitude near the study sites since 1952. This includes a 4.0 magnitude near Bonners Ferry in September of 1952 and two earthquakes in 1984. In 1984, one earthquake was a 4.1 magnitude near Moyie Springs and the other was ten miles north of Bonners Ferry and a 3.2 magnitude (Boundary County, 2005). Since then, there have been 12 earthquakes ranging from magnitude 2.5 to 3.9 near Sandpoint, Idaho approximately 30 miles south of Bonners Ferry. The largest of these earthquakes, the 3.9 magnitude, had an estimated intensity of four and the shaking could be lightly felt in Bonners Ferry (Murray and Svarc, 2017).

1.3.3 Hydrology

River incision is a likely trigger for the numerous landslides occurring in the area because of the proximity of the sites to major rivers. There have been numerous studies on the coupling of landslides, erosion rates, and river incision (Egholm et al., 2013; Golly et al., 2017; Larsen and Montgomery, 2012; Ouimet et al., 2007; Highland and Bobrowsky, 2008). There are two types of river incision: vertical and lateral (Larsen and Montgomery, 2012). According to Egholm et al., incision from the rivers steepens the slopes of the surrounding hillsides; the steepening of these slopes as the channel elevation lowers continues until it eventually reaches a threshold slope. After reaching this threshold slope, the slope can fail and landslides occur. The sediment input from landslides into incising rivers can either protect the riverbed from further erosion by forming a sediment layer on the bottom or provide more abrasion and accelerating of the erosion rate and incision process. Eventually, a protective sediment layer is built up on the bottom of the channel slowing the erosion rate and reducing the number of landslides (Egholm et al., 2013).

1.3.4 Anthropogenic Activity

Human activity is also a possible triggering method, as these landslides occur along railroad corridors where rail construction, repairs, vegetation removal, and changing drainage patterns have destabilized the hillslopes (Highland and Bobrowsky, 2008). Undercutting slopes through river incision or human activity and leaving more mass on the top of the slope can lead to over steepening; once it meets the required threshold slope, landslides may occur (Egholm et al., 2013; Highland and Bobrowsky, 2008). Other human activities that can lead to landslides include creating or draining reservoirs, irrigation, improper slope grading, leaking pipes, and

improper excavation (Highland and Bobrowsky, 2008). Given that all the sites in this study are railroad corridors, they have undergone construction that has altered the natural slopes. The combination of the geomorphological history, underlying geology, and numerous trigger mechanisms makes these railroad corridors in northern Idaho very susceptible to landslide driven derailments; threatening the environment and necessitating a methodology that can map and monitor these potentially deadly geohazards.

1.4 Study Site Characterization

The Kootenai River is part of the international Kootenai River Drainage Basin, which is 721 kilometers long and drains an area of 28,324 square kilometers stretching from British Columbia, Canada down into parts of northern Idaho and Montana, United States (Columbia Basin Trust, 2021; Polzin and Rood, 2000). The study area for this thesis is located in the Purcell Trench section of the Kootenai River near Bonners Ferry and Moyie Springs, Idaho. This area experiences on average 20.47 in of precipitation and 52 in of snow annually (U.S. Climate Data, 2022). Specifically, there are three main areas of interest consisting of one landslide site along the Moyie River, three sites of interest along the main Kootenai River, and one site along Deep Creek (Figure 1). Each of these sites have recently experienced a mass-movement event and two of them led to train derailments (Hanrahan, 2020; Sokol, 2017).

The Kootenai River carves through the glacial and flood deposits (~1-50 m thick) and into the Belt Super group creating very steep tall corridors along the section of river from the Idaho – Montana border to Bonners Ferry, Idaho. Sections are also composed of exposed intrusive mafic sills or members of the Prichard Formation that are Mesoproterozoic age (Breckenridge et al., 2012; Burmester et al., 2010b). Near the junction with the Kootenai, the Moyie River cuts into

the glacial and flood deposits (~20m thick) as well as the underlying plutons and metamorphic rocks (Burmester et al., 2010; Link, 2002). The river incision created the steep canyon reach along the Kootenai and Moyie Rivers shown in Figure 1.

Deep Creek is a tributary connected to the meandering reach of the Kootenai River that incises into mostly colluvial deposits (~10 m thick) near steep hills of intrusive rock and sections of alluvial and glacial deposits (Barton et al., 2004; Burke et al., 2009; McFaddan et al., 2009). These river corridors are used by railway companies with the rail tracks often placed at the base or top of the steep hillslopes. The steep slope angle and unconsolidated flood and glacial deposits at the surface makes the slopes susceptible to landslides and other mass movements (Peters, 2012; Sarkar and Kanungo, 2004).

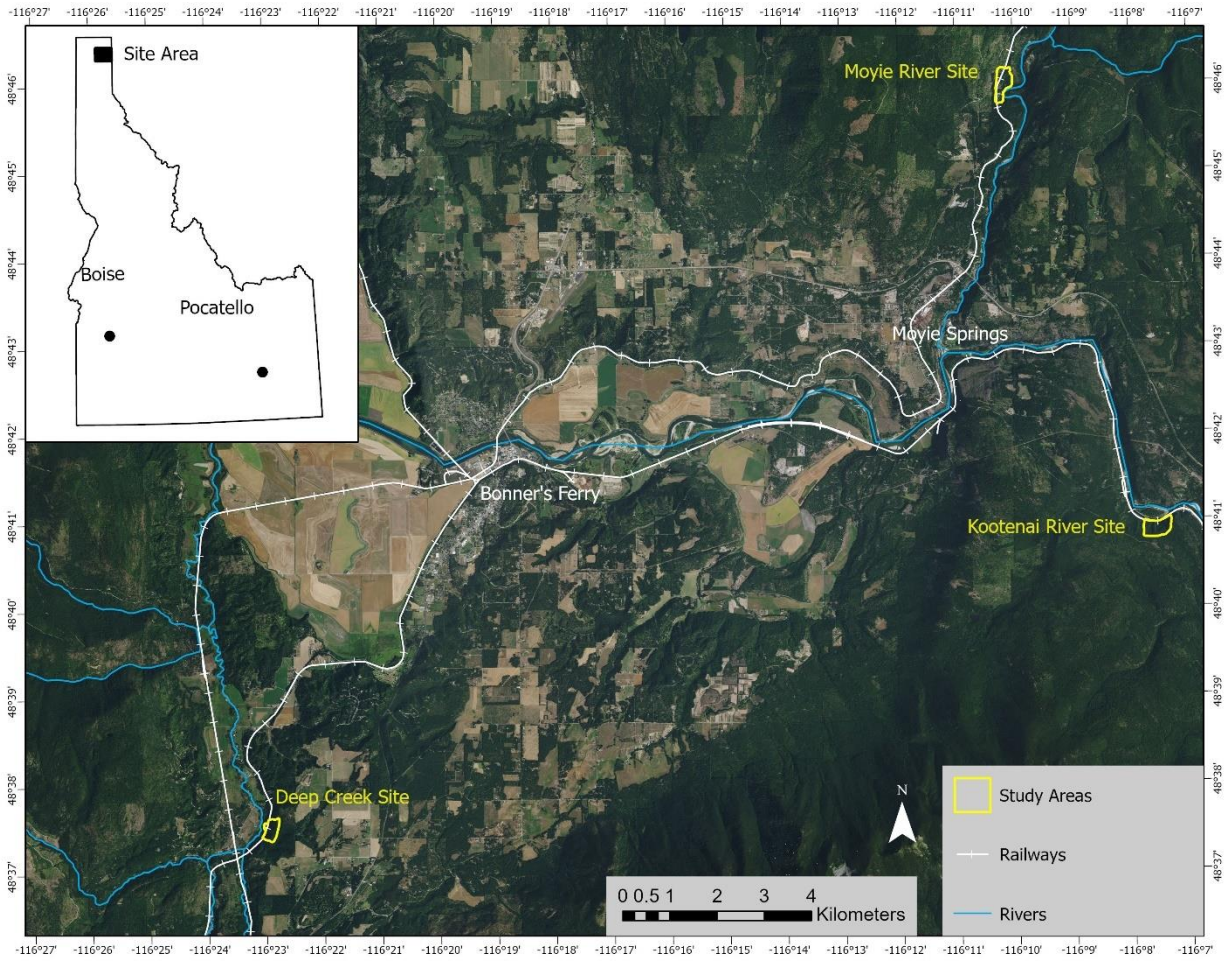

Figure 1. Study area map of the three sites in northern Idaho near the towns of Bonners Ferry and Moyie Springs. There are three sites along the Kootenai River, one site along the Moyie River, and another one along Deep Creek. (Image Source: 2019 National Agriculture Imagery Program)

1.5 Thesis Objectives

The Idaho Geological Survey (IGS) is mapping geohazards across the state and has identified landslides along transportation corridors as a serious risk for derailment (Lifton et al., 2020; Idaho Geological Survey, 2020). In northern Idaho, the combination of various environmental factors such as the presence of faults, unconsolidated surficial deposits, the incision of nearby rivers forming steep slopes, and railroad construction has left the study site area predisposed to landslide hazards. This has led to multiple derailments along the railway corridors, including a

rockslide and debris flow. In partnership with the Idaho Geological Survey, study sites were selected located along the Kootenai River, Moyie River, and Deep Creek in northern Idaho (Figure 1) for preliminary analysis of landslide potential and flown with Unmanned Aerial Vehicles (UAS) LiDAR in 2017 by Idaho State University.

In August 2021, we recollected UAS LiDAR data at these pilot sites. Our objectives were to: (1) measure mass movement change at the sites using a point cloud-to-point cloud comparison and (2) model mass movement susceptibility at the sites along these river corridors with object-based image analysis (OBIA). The main outcome of this project was the development of an accurate and cost-effective method for railway companies to monitor known mass movement sites using a temporal point cloud-to-point cloud comparison and to characterize the mass movement susceptibility with object-based image analysis (OBIA). This methodology aims to facilitate the long-term monitoring and management of these geohazards; thereby, preventing future derailments, service interruptions, and environmental contamination.

Chapter 2. Change Detection with Point-to-Point Cloud Comparison

2.1 Introduction

2.1.1 Mass movement hazard along transportation corridors

Recent landslide mitigation projects in Idaho from 2013 to 2018 along state managed highway transportation corridors from have cost over $15.8 million dollars (Idaho Office of Emergency Management, 2018). However, these geohazards are not isolated to just the highway network but another major transportation method in Idaho, the railroad corridors, many of which run along rivers. This potentially catastrophic interaction between mass movements and railroads is especially prevalent in northern Idaho along the Kootenai and tributary river systems, where landslides pose a threat to not only railroad workers but to the environment as well. Over the last few years there have been multiple train derailments in this part of Idaho, including one caused by a mudslide in 2017 along the Moyie River and another caused by a rockslide in 2020 (Hanrahan, 2020; Sokol, 2017). In 2020, the rockslide knocked the train engine into the Kootenai River resulting in diesel fuel contamination (Hanrahan, 2020). Effective and efficient monitoring methods are important for long-term management of these geohazards and prevention of future derailments.

2.1.2 Airborne and UAS LiDAR Scanning for Mass movement monitoring

Light Detection and Ranging (LiDAR)-equipped UASs are a practical method of imaging vegetated slopes where landslides are a potential hazard. By using LiDAR imagery, we can measure and analyze changes in slopes over time. These changes can indicate potential landslide activity and is an important aspect of landslide monitoring (Eker et al., 2018). LiDAR uses laser pulses and their calculated return times to compile accurate elevation data. Although LiDAR

data requires more post-processing compared to other sensors, it is the ideal sensor to use for this study because of its high resolution and ability to penetrate vegetation (Carey et al., 2019). The railway corridors of interest are heavily vegetated, so we need the ability to image the ground through the thick vegetation.

A UAS platform provides numerous benefits to the study. Using preprogrammed flight plans, UASs can autonomously fly through remote and hazardous sites (Hung et al., 2019). A UAS is a more efficient and cost-effective platform than airplanes or satellites. A manned aircraft, although having a longer flight time than a UAS, is more expensive to operate due to aviation fuel costs and aviator fees; it also requires more time to plan flights. In contrast, a UAS is more flexible to schedule, relies on rechargeable batteries instead of fuel, has lower remote pilot fees, and is compact for travel (Carey et al., 2019). Point clouds generated by LiDAR can be used to process elevation changes over time directly and to determine topographic variability including surface roughness, allowing for the analysis of patterns in movement history, types of material, and morphology of landslides (Glenn et al., 2006).

2.1.3 Challenges in change detection comparison between LiDAR point clouds

Issues often arise when comparing LiDAR datasets collected at various time periods with different sensors and procedures. These include conflicts between the earth surface model used such as geoids or ellipsoids, poor coregistration of flightlines, variations in data resolution, changes in post processing steps, differences in georeferencing, and inconsistent methods to quantify uncertainty (Schaffrath et al., 2015; Okyay et al., 2019; Cucchiaro et al., 2020). These disparities can lead to vertical and horizontal biases, as well as poor uncertainty measurements that under or overestimate change (Schaffrath et al., 2015; Bernard et al., 2021).

There are some potential solutions to these issues; studies have shown a vertical bias attributed to both different geoid models and localized offset strips occur from poor coregistration of the flight lines. One method of correcting geoid issues is to ascertain the difference with calculators such as the National Geodetic Survey interactive calculator or the National Ocean Services vertical datum transformation tool (Schaffrath et al., 2015; Cooper et al., 2013). When attempting to identify any horizontal bias, x and y coordinates of well-defined structures on both datasets can be compared (Schaffrath et al., 2015). There are issues with this solution at sites where ground control points cannot be used, either due to dense vegetation or hazardous conditions. Even after reprocessing the LiDAR data with the same georeferencing system poor coregistration of the flights can still cause alignment issues. This last issue of poor coregistration has multiple solutions; the common way to address this problem is to use the original GPS and LiDAR data to recalibrate the new raw data (Schaffrath et al., 2015). This can be difficult in areas where ground control points cannot be laid out. Methods such as the "Align" tool in CloudCompare software require the user to be able to identify multiple sets of equivalent points before even a fine registration can be used (CloudCompare, 2016).There are multiple algorithms that can be used for the calibration without ground control points, a popular method is to use the iterative closest point algorithm, which is a two-step registration process relying on minimum distance (Kuçak et al., 2022, Booth et al., 2020; Cucchiaro et al., 2020). Other common tools to correct for coregistration used in repeat LiDAR studies include the mathematical Generalized Procrustes Analysis, the plane structure based 4-point Congruent sets technique, or a Bayesian approach to realign the flight strips for both flights (Fotsing et al., 2020; Cucchiaro et al., 2020; BayesMap Solutions LLC, 2022).

2.1.4 Change detection with UAS LiDAR

There are multiple methods for calculating the change of a hill slope: the point cloud-to-point cloud methods, point cloud-to-model (C2M), and the DEM of difference methods (DiFrancesco et al., 2020; Esposito et al., 2017). The DEM of difference methods uses two rasters of elevation data and subtracts one of these rasters from the other to calculate the difference. Since this method projects the point cloud onto the two-dimensional x-y plane, the change detected in this method is one dimensional only along the z-axis (DiFrancesco et al., 2020). This method, while computationally efficient, lacks accuracy when it comes to complex terrain where the surface orientation is greatly varied (DiFrancesco et al., 2020). The C2M method compares a point cloud to a triangulated mesh surface of a second point cloud. The distance is calculated from each point in the cloud to the nearest point on the surface mesh. For this reason, the accuracy of this method is dependent on the quality of the triangulated surface (DiFrancesco et al., 2020).

There are two methods of comparing point clouds; the cloud-to-cloud (C2C) change detection and the Multiscale model-to-model cloud comparison (M3C2). The distance is measured between the points from one cloud to the nearest point of another cloud. Due to the arbitrary nature of simply using the closest point this method requires dense point clouds and low surface roughness. Furthermore, this method has one major drawback in that it does not calculate sign direction which is necessary for identifying erosion or deposition.

However, a variation on this C2C, known as the multiscale model-to-model cloud comparison (M3C2) is ideal for measuring material loss and gain (DiFrancesco et al., 2020). The M3C2 method is a direct comparison between two point clouds collected at different times, using an algorithm that calculates distance of a normal vector. Instead of limiting itself to just the nearest point in the next cloud, the vector is calculated using the points nearest neighbors

(DiFrancesco et al., 2020). This method avoids the uncertainty of vertical height that is often intrinsic to using DEM-to-DEM analysis (Esposito et al., 2017).

2.1.5 Multiscale Model-to-Model Cloud Comparison

For this study we used the opensource software CloudCompare which has a M3C2 plugin. This tool works by first computing the surface normal orientations for the reference point cloud (2017) over a specified diameter; for these sites we used a diameter of 1m. Once these normals are calculated the plugin creates a cylinder around each core point to calculate the distance (Figure 8). The diameter of this cylinder is determined by the user-specified projection scale and the cylinder height is determined by the max depth parameter. For all sites the projection scale and max depth was one meter, with the exception of the Deep Creek site that had a max depth of 2 m due to the large volume loss along the cliff face. These 1 m parameters were determined from looking at the point cloud densities and the RMS errors (Barnhart et al., 2013; Lague et al., 2013). Selecting 1-2m as the max depth cutoff was also based on the necessity of detecting small scale movements on the slope that could cause derailments or require material to be removed from the tracks.

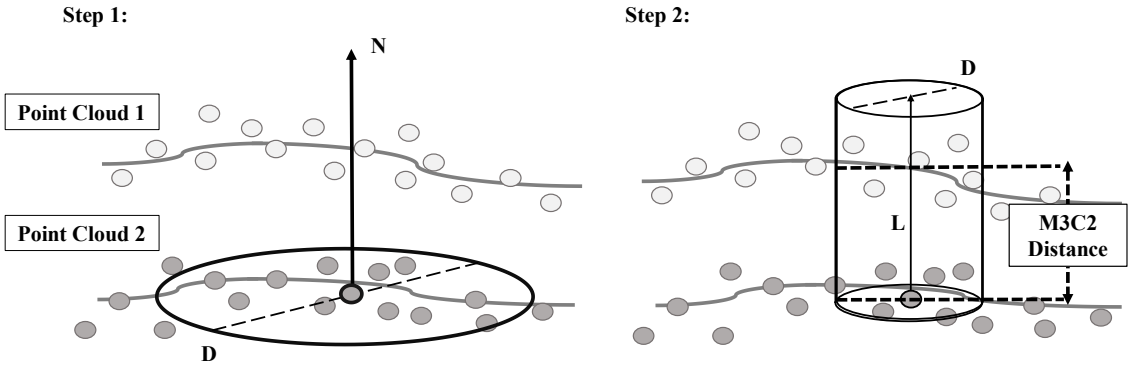

Figure 2. Multiscale Model to Model Cloud Comparison (M3C2) adapted from Lague et al., 2013 and DiFrancesco et al., 2020.

The M3C2 Algorithm does not require any meshing or gridding to detect changes at a site. The only parameters necessary are: two point clouds, a defined normal scale, the projection, clearly defined registration error, and at least four core points (Eker et al., 2018). From these parameters, software such as the CloudCompare plugin calculates the distances between two point clouds, measuring the change for each site and displaying this change as a new point cloud. Additionally, the software will generate a scalar field for significant change. In this case, significant change is the local limit of detection at 95% confidence (DiFrancesco et al., 2020; Esposito et al., 2017). Using the precision map variant, the M3C2 plugin will generate a scalar field for distance uncertainty. According to the CloudCompare website (https://www.cloudcompare.org/doc/wiki/index.php?title=M3C2_(plugin)), this variant uses the precision values stored in the LiDAR point clouds instead of estimations calculated by CloudCompare.

2.1.5 Goals and Objectives

Accurate and efficient monitoring methods are an important aspect for long-term management of mass movements. In this study, we used UAS based LiDAR combined with the M3C2 algorithm to prototype a methodology for using repeat LiDAR to measure change at a site that avoids the common bias of other repeat LiDAR studies. We chose three study sites along the Kootenai River, Moyie River, and Deep Creek which we flew in 2017 and again in 2021. We then applied a stripping correction using BayeStripAlign2.1 software. We were able to align the two flights and calculate precise changes at the site using CloudCompares M3C2 plugin. This methodology avoids the common issues surrounding repeat LiDAR as well as identifies and

measures significant change at the sites, allowing for accurate monitoring of the slopes for renewed mass movement activity.

2.2 Methodology

2.2.1 Landslide Study Sites

For this study three sites in northern Idaho were chosen for analysis. These railroad sites have all recently undergone mass movement activity and run along important rivers. The three sites are located along the Kootenai River (Figure 2), Deep Creek (Figure 3), and Moyie River (Figure 4). UAS collected LiDAR at all three sites over the course of multiple flights, first in 2017 and again in 2021.

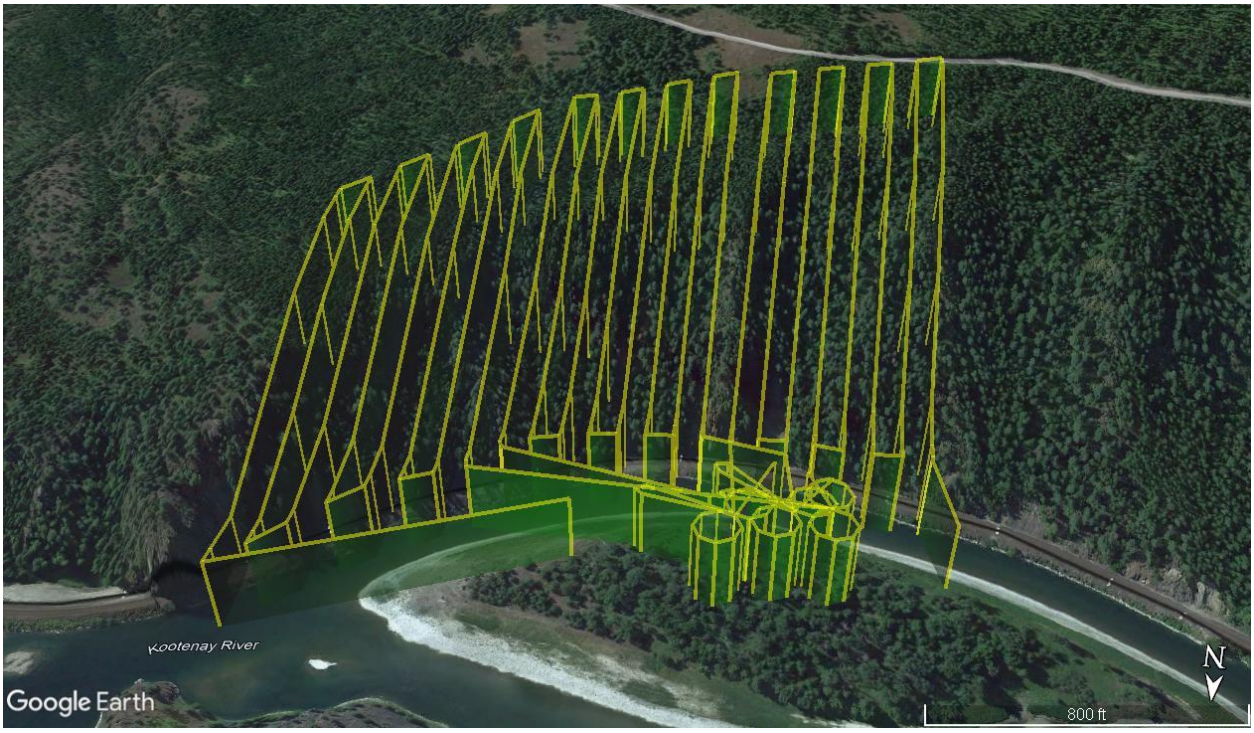

Figure 2. Kootenai River site with UAS flightpaths shown in yellow. Imagery: Google Earth Pro Idaho, USA. 48° 40’ 54.03’’N 116° 07’ 32.00” W, Eye alt 3945 ft.

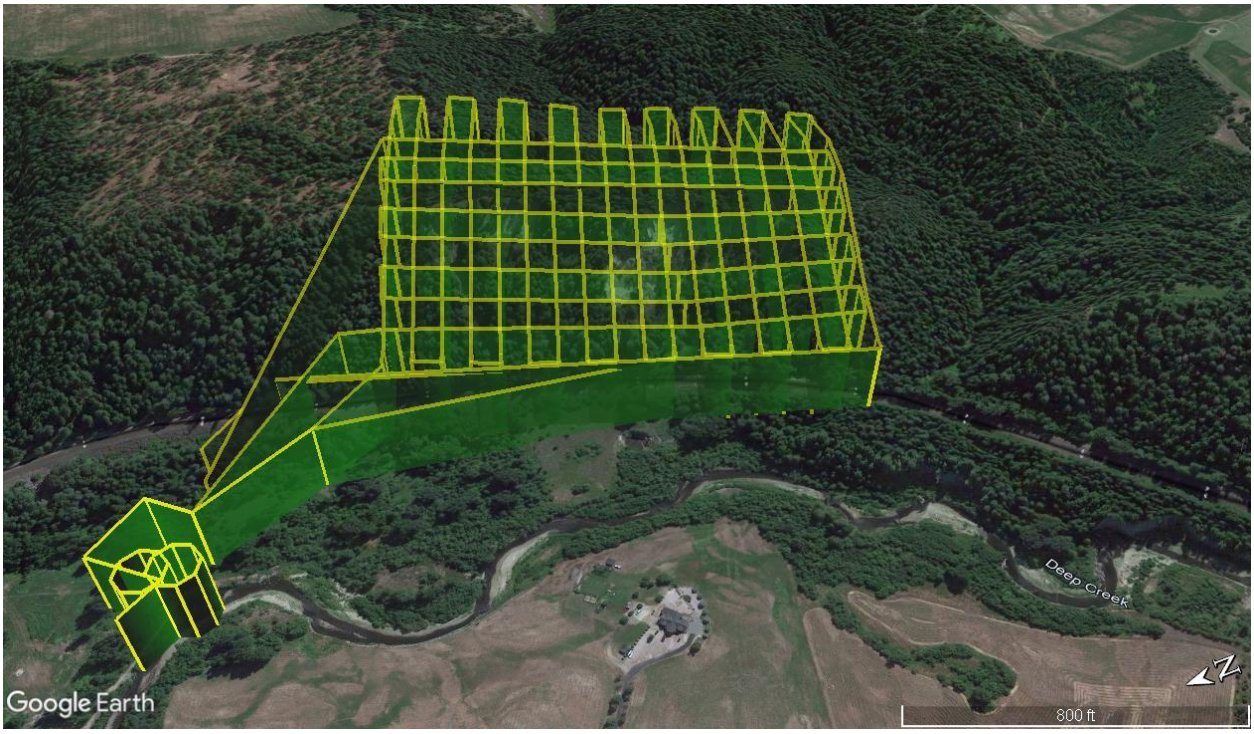

Figure 3. Deep Creek site with UAS flightpaths shown in yellow. Imagery: Google Earth Pro Idaho, USA. 48° 37’ 31.78’’N 116° 22’ 56.67” W, Eye alt 4233 ft.

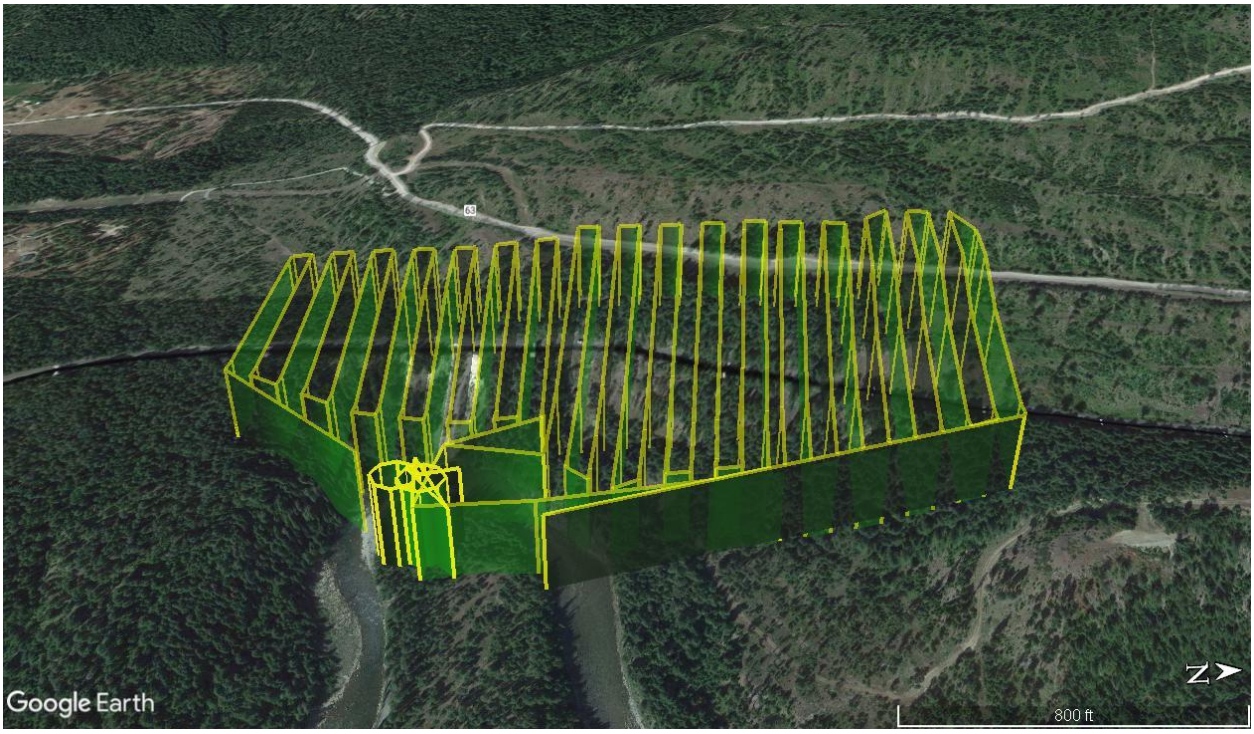

Figure 4. Moyie Site with UAS flightpaths shown in yellow. Imagery: Google Earth Pro Idaho, USA. 48° 45’ 55.39’’N 116° 10’ 12.74” W, Eye alt 4192 ft.

2.2.1 2017 UAS LiDAR Configuration

In 2017 we flew a DJI Matrice 600 Pro equipped with a lightweight Geodetics Inc. Geo-MMS Velodyne (VLP-16) LiDAR sensor configuration (Figure 5). Both the 2017 and 2021 campaigns used the same LiDAR sensor (VLP-16); however, the sensors were configured by two different manufacturers. The VLP-16 is a 16 channel, dual return LiDAR sensor that generates 300,000 points per second, and has an accuracy of 3 cm at a range of 100 m. The VLP-16 rotating lasers are equally spaced between -15 and +15 to create a 30° vertical field of view and a horizontal view of 360° (Jacobs et al., 2021; Hyper-Tech Systems, 2017; Andrew Lassiter et al., 2020). For both campaigns, the LiDAR sensor was mounted to the UAS with the vertical field of

view parallel to the ground surface. This sensor setup is commonly used with UASs for mapping as described in Jacobs et al. (2021).

Figure 5. DJI Matrice 600 Pro equipped with a lightweight Geodetics Inc. Geo-MMS Velodyne LiDAR sensor configuration used in 2017 Campaign. Image credit: Aevex Aerospace (https://geodetics.com/product/geo-mms/)

For the 2017 campaign, the Geo-MMS uses a proprietary Geo-MMS navigational unit for GPS and inertial measurement unit (IMU) data attached to the LiDAR sensor. The Geo-MMS system for georeferencing uses a dual antenna configuration to collect the GNSS logs. This system aids in the georeferencing the LiDAR datasets by recording a timestamp for every LiDAR pulse as well as information regarding the latitude, longitude, yaw, pitch, roll, and altitude (Jacobs et al., 2021). This data is collected at a measurement rate of 200 Hz (Trimble, 2019; Jacobs et al., 2021). We used the nearby Boundary County Airport-65s as the base station for the Post Processed Kinematic (PPK) processing. The Airport is 9.94 km away from the Moyie Site, 13.25 km away from Kootenai Site 1, and 13.18 miles away from the Deep Creek Site. PPK is a technique where the base station and rover global navigation satellite system

(GNSS) location data logs are corrected after the flight instead of the Real-time kinematic (RTK) technique which applies the positioning algorithm corrections in real time during the flights (Eker et al., 2021).

2.2.2 2021 LiDAR UAS LiDAR Configuration

As in the 2017 flight campaigns, we equipped the DJI Matrice 600 Pro with a lightweight Velodyne LiDAR sensor, however this VLP-16 is co-mounted with the Headwall Nano hyperspectral sensor (Figure 6). In the Headwall configuration the LiDAR sensor is paired with an Applanix APX-15 GNSS inertial sensor collecting data at a measurement rate of 200 Hz (Trimble, 2019; Jacobs et al., 2021). The LiDAR sensor was mounted to the UAS with the vertical field of view parallel to the ground (Jacobs et al., 2021). The Applanix GPS sensor is used in tandem with a Trimble R10 GNSS base station. The Trimble receiver and antenna were set up at each site to run as a base station corresponding with the Headwall GPS. The Trimble continuously captured data for at least two hours at each site while the drone recorded its own location. Unlike the 2017 sensor configuration, we attached an independently mounted RGB camera (Ricoh GR II) triggering every two seconds to capture aerial images during the LiDAR surveys.

Figure 6. Image of DJI Matrice 600 Pro equipped with a lightweight Velodyne LiDAR sensor and co-mounted with the Headwall Nano hyperspectral sensor used in 2021 campaign. Image: Delparte, 2021

2.2.3 Flight Planning and Data Acquisition

We conducted our fieldwork at the landslide sites August 28-30, 2021. We flew a total of three landslide sites: one along the Kootenai River and the other two along Deep Creek and Moyie River. The sites along the Kootenai River were accessible by boat and we flew from nearby sandbars. The flights maximized coverage of the mass movement sites while remaining cognizant of the limited flight time of the drone (~15 minutes from takeoff to landing). To improve the density of the point cloud from the 2017 campaign which flew the sites with a side distance of 50 m, we collected the 2021 LiDAR with a side distance of either 21 m or 25 m. The LiDAR flights for both 2017 and 2021 were flown at a speed of 5 m/s and an altitude of 65 m.

The side distance for the 2021 LiDAR flights was 25 m for each site except for the Moyie site which had a side distance of 21 m. The Deep Creek site, Kootenai Site, and the Moyie Site

each required three flights to cover the entire slide area. At the start of each flight in 2017 and 2021, we calibrated the LiDAR sensor IMU using a couple of maneuvers including a figure eight pattern and a straight line forward and back which is flown at a faster speed. These calibrations help improve the accuracy and density of the point clouds.

Table 2. 2021 LiDAR Flight Information and Collection Parameters

Site	**# of Flights**	**Altitude (m)**	**Speed (m/s)**	**Sidelap (m)**	**Point Density (per m^2)**	**Ground Point Density (per m^2)**
Deep Creek	3	65	5	25	2478.9	116.2
Kootenai	3	65	5	25	1882.6	61.6
Moyie	3	65	5	21	1631.1	69.2

2.2.3 Workflow to Reduce Repeat LiDAR Issues

To address repeat LiDAR issues we used the following workflow (Figure 7) that combines four different softwares for post processing LiDAR: LiDARTools, PosPac UAV, Bayes Strip align, and LAStools. First generating the Smoothed Best Estimate of Trajectory (SBET) in PosPac UAV, correcting the yaw, pitch, and role in LiDARtools to generate the LAS file. These LAS files are then processed through Bayesian Inference and classified. The final products generated in this workflow are ground surface classified models ready for comparison. This workflow is further described with detailed command instructions used in Appendix II.

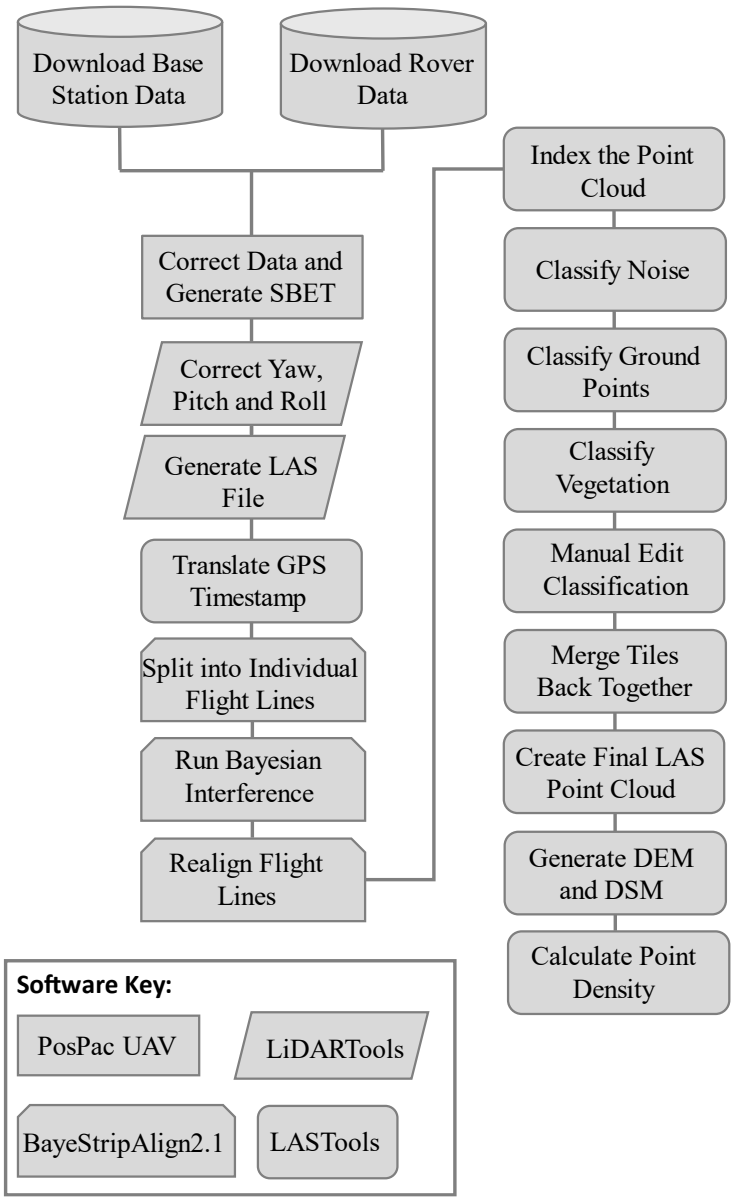

Figure 7. LiDAR Post Processing Workflow Diagram

2.2.3.1 Step 1. LiDAR Post-Processing

The first step in processing the 2021 LiDAR data was to create SBET files from the flight GPS data using the software PosPac UAV (v. 8.4). PosPac UAV software uses the IMU and GNSS data to georeference the flight data without the use of ground control points, since the sites were too hazardous for the placement of ground control points. This method not only

improves the accuracy but can also fill any gaps in the GNSS data that are caused when the connection is temporarily lost with the rover during a flight (Applanix, 2020). As we placed our R10 Trimble base station over an unknown reference location, we used Trimble's CenterPoint RTX Post-Processing service to accurately reference the position from which the base data was collected. In PosPac we load in the Rover and Base station data files captured during each flight and adjust the base station location to the corrected position obtained from Trimble's CenterPoint RTX service report. Next, we ran the GNSS-Inertial Processor to compute the trajectory from the raw data. This process matches the timestamps of the position and altitude data with those of the LiDAR returns. We then exported these flight trajectories as SBET files. With these SBET files and the timestamps of the LiDAR sensor returns we used Headwall's propriety LiDARTools software to generate LAS point cloud files. LiDARtools georeferences the point clouds by matching the timestamps from the LiDAR returns with the timestamps from the Applanix APX-15 base station data in the SBETs (VanValkenburgh et al., 2020; Jacobs et al., 2021). Before exporting the LAS files, we had to adjust the roll of the UAS to 86.8° and the pitch to 0.12° in LiDAR tools.

Since the LiDAR data comes out of LiDARTools in a GPS time format specific to LiDAR Tools the global encoding needs to be set and the GPS time translated to a format that can be read by other softwares using Rapid Lasso's LASTools. Before continuing to process the point clouds in LASTools the flightlines need to be aligned. In order to make sure that the flight lines of the UAS are as closely aligned as possible to increase the accuracy of the data and remove any bias from the repeat LiDAR we used a stripping correction software called BayeStripAlign2.1 to align the flight strips.

We processed our 2017 LiDAR data with the Geodetics LiDAR Tool proprietary software that generates a PPK trajectory file (SBET) from the matching CORS base station data and onboard Geo-MMS navigational GNSS IMU unit data. The LiDAR Tool software exports .las outputs (AEVEX Aerospace).

2.2.3.2 Step 2. Strip Alignment

Both the 2017 and 2021 LiDAR datasets were run through BayeStripAlign2.1. This software splits the flight up into individual flightlines before running a Bayesian inference to adjust the flight strips and correct geometric errors (BayesMap Solutions LLC, 2020). The uncertainty of the point cloud is improved by assigning a larger weight to the more accurate points (BayesMap Solutions LLC, 2020). Finally, the flight lines are realigned into a new point cloud. This paired with the use of the geodetic grade GPS and PPK to reduce the RMS Error for the point clouds.

StripAlign corrects the absolute and relative geometric errors of LiDAR swaths that are caused by IMU altitude and position errors. This required us to input LAS files with timestamps as well as the SBET trajectory files. These timestamps are used to register overlapping flight lines and correct low or high frequency IMU drifts, boresight misalignment, lever arm errors or internal geometry miscalibration (BayesMap Solutions LLC, 2020). Using this software, we first cut each site into individual strips of flightlines before realigning the cuts based on the corrections. The 2021 data had an additional step of channel splitting before realignment because of the IMU system used. The Geodetics IMU used in the 2017 flight did not label the channels and therefore channel splitting could not be applied. For these multibeam scanners the flightline swaths can be divided up into multiple channels based on the scan direction either forward or backwards. For these sites a 4-channel map was used, which is the maximum number of

channels. This improves the accuracy of the dataset by increasing the overlap of the swaths (BayesMap Solutions LLC, 2020). The corrections we applied to the swaths included a Bayesian Inference to adjust the strips and improve any systematic geometric errors. In order to improve the uncertainty, the more accurate points are given a larger weight (BayesMap Solutions LLC, 2022). The software then generates accuracy assessments and intensity maps for the sites. The displacement errors in the z direction coming out of the BayesStripAlign2.1 for the 2017 flights are as follows: 0.011 m for the Kootenai River Site, 0.005 m for the Moyie River site, and 0.019 m for Deep Creek. The displacement errors for the 2021 flights were 0.003 m for the Kootenai River site, 0.008 m for the Moyie River site, and 0.004 m for the Deep Creek site (Table 3).

Table 3. BayesStripAlign Displacement in the Z-Direction Results for 2017 and 2021

2021 Site	**Displacement in Z-Direction Before BayesStripAlign (m)**	**Displacement in Z-Direction After BayesStripAlign (m)**
Kootenai Site	0.192	0.003
Deep Creek	0.283	0.004
Moyie River	0.277	0.008
2017 Site		
Kootenai Site	0.621	0.011
Deep Creek	0.353	0.019
Moyie River	0.897	0.005

2.2.3.3 Step 3. Point Cloud Classification

The .las point clouds are then processed in rapidlasso's LASTools to classify the points in the cloud and create the bare earth models and digital surface models. This processing required multiple steps and tools in LASTools. The first step is to run the LASindex tool which creates and appends a file containing the spatial indexing information for the point cloud. This includes information on what points are in each spatial region which is useful when running spatial queries (rapidlasso, 2012; rapidlasso). The next step is to break the site up into smaller more

easily processed pieces, to do this, we used LAStiles to create 100 m square tiles with 10 m buffers. When the site was tiled, we were able to start the classification process. To start, we ran LASnoise to classify the noise with the default settings. After classifying the noise, we ran LASground making sure to specify that all returns will be used since the default only uses the second return. This tool classifies certain points in a tile as ground points and computes the height of the ground points. The next tool we ran was LASclassify where we set the ground offset to 1 m to classify the vegetation in the point cloud. Now that the majority of the processing was done, we removed the buffers around the tiles using LAStile. We then ran the LASnoise tool again using a gridding method that classified a point whose nearest neighbor was 20 m away as noise. This helped to classify the high noise that was mistakenly classified as vegetation. With the LASview tool we were able to manually edit any points that were misclassified and remove sporadic points along the edges of the clouds. These edited tiles are saved as Lay files and need to be converted into Laz files with the LASlayers tool. These tiles are then merged into one cloud using the LASmerge tool and exported as a LAS file that can then be loaded into either CloudCompare or ArcGIS Pro. This tool was ran twice, once using only the ground points to create a DEM and the second time using the ground points and vegetation points to create a DSM. At this point we then used the Blast2DEM tool to create merged TIFF files of the DEM and DSM. All data was exported from LAStools to WGS84 UTM 11 for analysis.

2.2.5 Point-to-Point Cloud Comparison

To perform a point cloud-to-point cloud comparison between the 2017 and 2021 point clouds we imported the cleaned point clouds into CloudCompare. After StripAlign processing only a minor alignment of the two point clouds using the fine registration tool was needed. This tool ran

10,000 iterations with a 2-million-point random sampling limit using the 2017 cloud as the reference cloud. The overlap of the point clouds was estimated to be between 15% and 40% for the sites. The CloudCompare M3C2 plugin was then used to calculate the distance between the points of the 2017 point cloud and the points of the 2021 point cloud and, therefore incorporated any elevation changes during that timeframe.

2.2.5 Volume Calculation

The M3C2 plugin identifies significant change and displacement. However, it does not calculate any volumetric change. In order to determine the volume of material that has been lost or gained from 2017 to 2021 another CloudCompare tool called the 2.5D Volume tool was used. This tool creates a grid for each point cloud before it computes the volume between two point cloud grids. When running this tool the main parameters that have to be determined are: the before and after point clouds, the step size, projection direction, and the value of the empty cells. For this project the "Before" point clouds are the 2017 point clouds and the "After" point clouds are the 2021 point clouds. The "step" for these grids are set to 1m. For the volume calculation the length and width of each square in the grid are 1 m, therefore, the volume equation is 1 m multiplied by 1 m multiplied by the height of the cell (CloudCompare, 2015). The projection direction is z direction because we are interested in the movement of the material downslope indicated by a loss and gain in volume. We experimented with leaving the empty cells empty or having the tools interpolate the cell's value and determined that having the value interpolated with the average height provided a much more useful result for mitigation and monitoring then simply relying on the individual points, since only non-empty cells are used in the calculations.

For the areas of interest at each site we ran the 2.5D Volume tool on the aligned 2017 and 2021 point clouds. These areas of interest were first segmented from the rest of the cloud to improve accuracy and diminish the number of empty cells. The total volume, base surface, volume added, and volume lost values were recorded.

2.3 Results

2.3.1 Point Cloud Generation for 2017 and 2021

The point clouds were aligned with a fine scale Iterative Close Point alignment for an average RMS error of ~14 cm. The Deep Creek site had the lowest RMS error at ~12 cm, Kootenai site had an RMS error of ~14 cm, the, and the Moyie site had the highest RMS error due to the sparseness of the point cloud at 18 cm. After the clouds were aligned and the scale adjusted, we used the M3C2 plugin for CloudCompare.

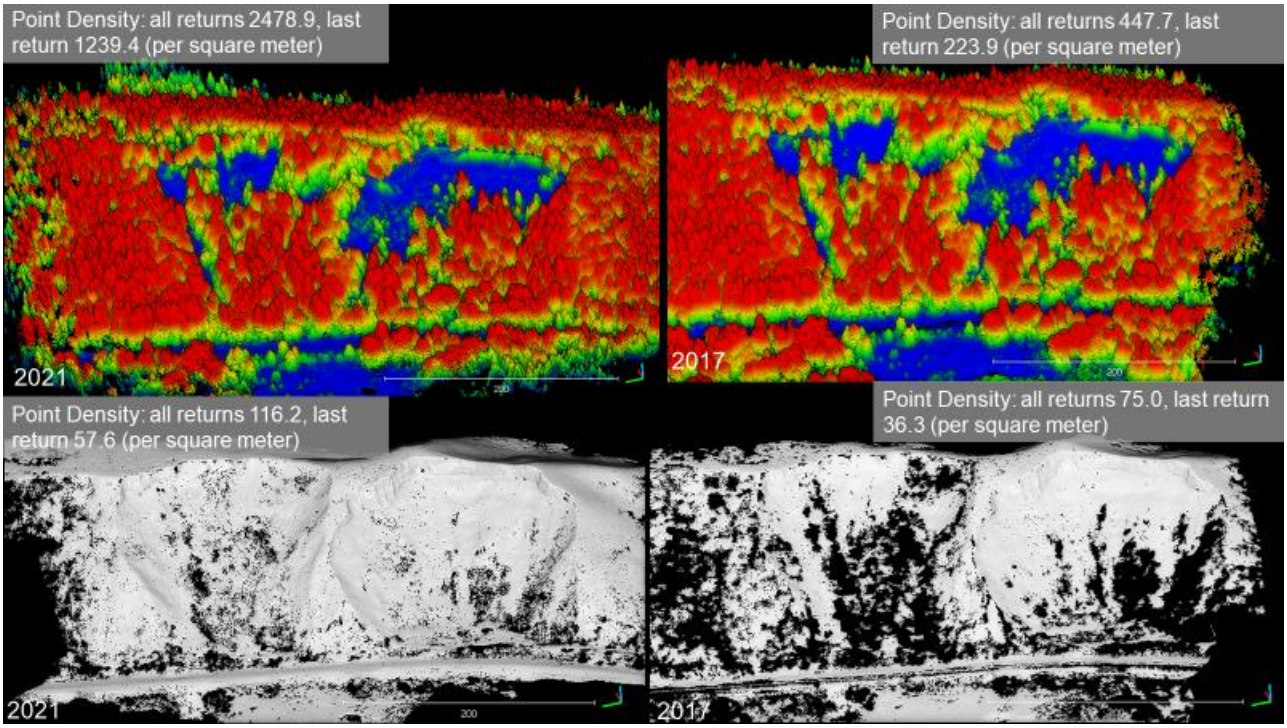

Figure 8. Deep Creek 2021 (left) and 2017 (right) Point Clouds. The top to images are the DSMs for the site with the color scale based on elevation. The grey images below are the DEMs.

This alignment method was able to align the 2017 and 2021 point clouds despite the differences in point cloud density. A bare earth point cloud and a classified point cloud with vegetation for each of the sites. The Deep Creek site final point clouds had a per square meter point density of 2478.9 and 447.7 for the 2021 and 2017 classified point clouds respectively. The bare ground point clouds had sparser density of 116.2 points per square meter and 75 points per square meter for the 2021 and 2017 campaigns (Figure 8).

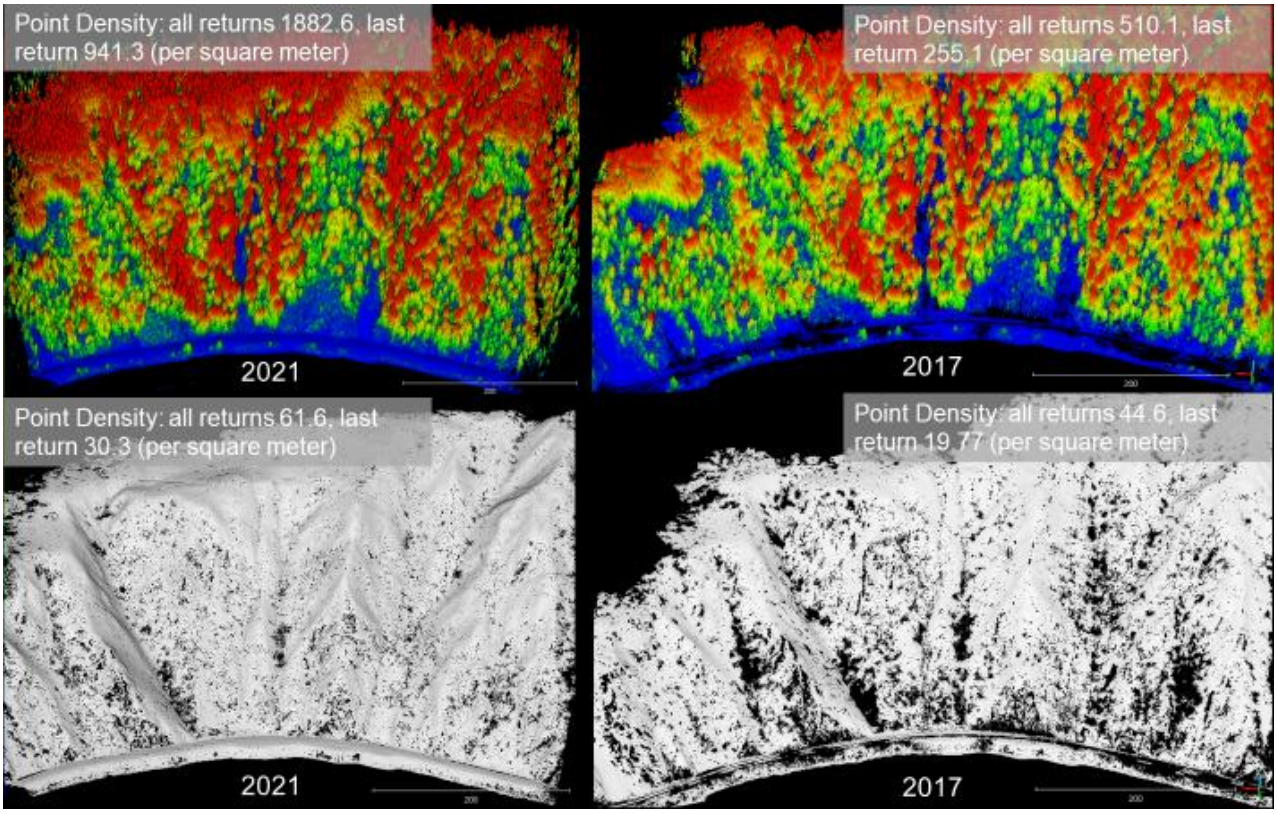

Figure 9. Kootenai River 2021 (left) and 2017 (right) Point Clouds. The top two images are the DSMs for the site with the color scale based on elevation. The grey images below are the DEMs.

The Kootenai River site final point clouds had a per square meter point density of 1882.6 and 510.1 for the 2021 and 2017 classified point clouds respectively. The bare ground point clouds had sparser density of 61.6 points per square meter and 44.6 points per square meter for the 2021 and 2017 campaigns (Figure 9).

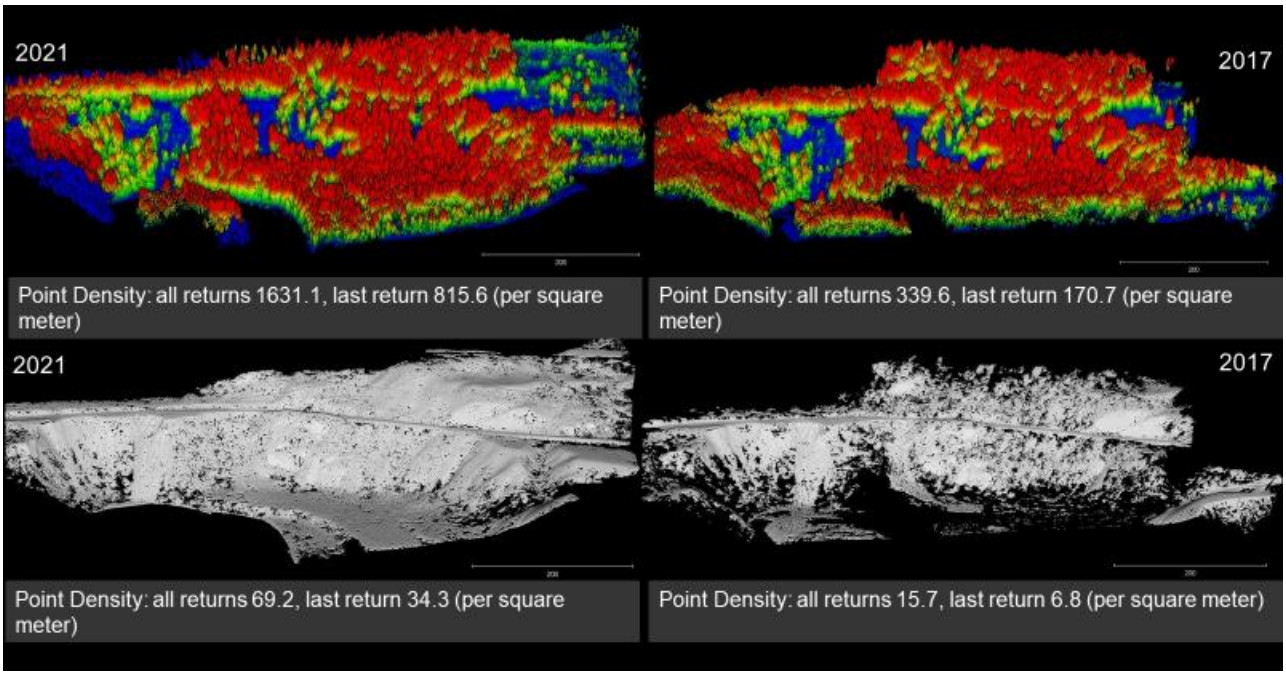

Figure 10. Moyie River 2021 (left) and 2017 (right) Point Clouds. The top to images are the DSMs for the site with the color scale based on elevation. The grey images below are the DEMs.

The Moyie River site final point clouds had a per square meter point density of 1631.1 and 339.6 for the 2021 and 2017 classified point clouds respectively. The bare ground point clouds had sparser density of 69.2 points per square meter and 15.7 points per square meter for the 2021 and 2017 campaigns (Figure 10).

2.3.2 M3C2 Measured Change between 2017 and 2022 LiDAR

The M3C2 plugin outputs four new point clouds: M3C2 distance, significant change, nearest neighbors, and distance uncertainty. The M3C2 cloud shows the displacement between the two point clouds with blue areas correspond with loss and red areas with gain. The significant change shows a displacement with the local limit of detection at 95% confidence (DiFrancesco et al., 2020; Esposito et al., 2017). For the section I will focus on one area of interest per site; these

areas are where there has been significant change that poses the most immediate threat to the railroad tracks.

2.3.2.1 Deep Creek M3C2 and Volume Results

The significant change values for the site ranged between ~0.25–1.9 m (Figure 11). The main area of interest was along the near vertical cliff face; along this cliff face there was about ~1.5-1.9 m of loss at the area of interest with a corresponding deposit of material with an average between ~1-1.5 m (Figure 12).

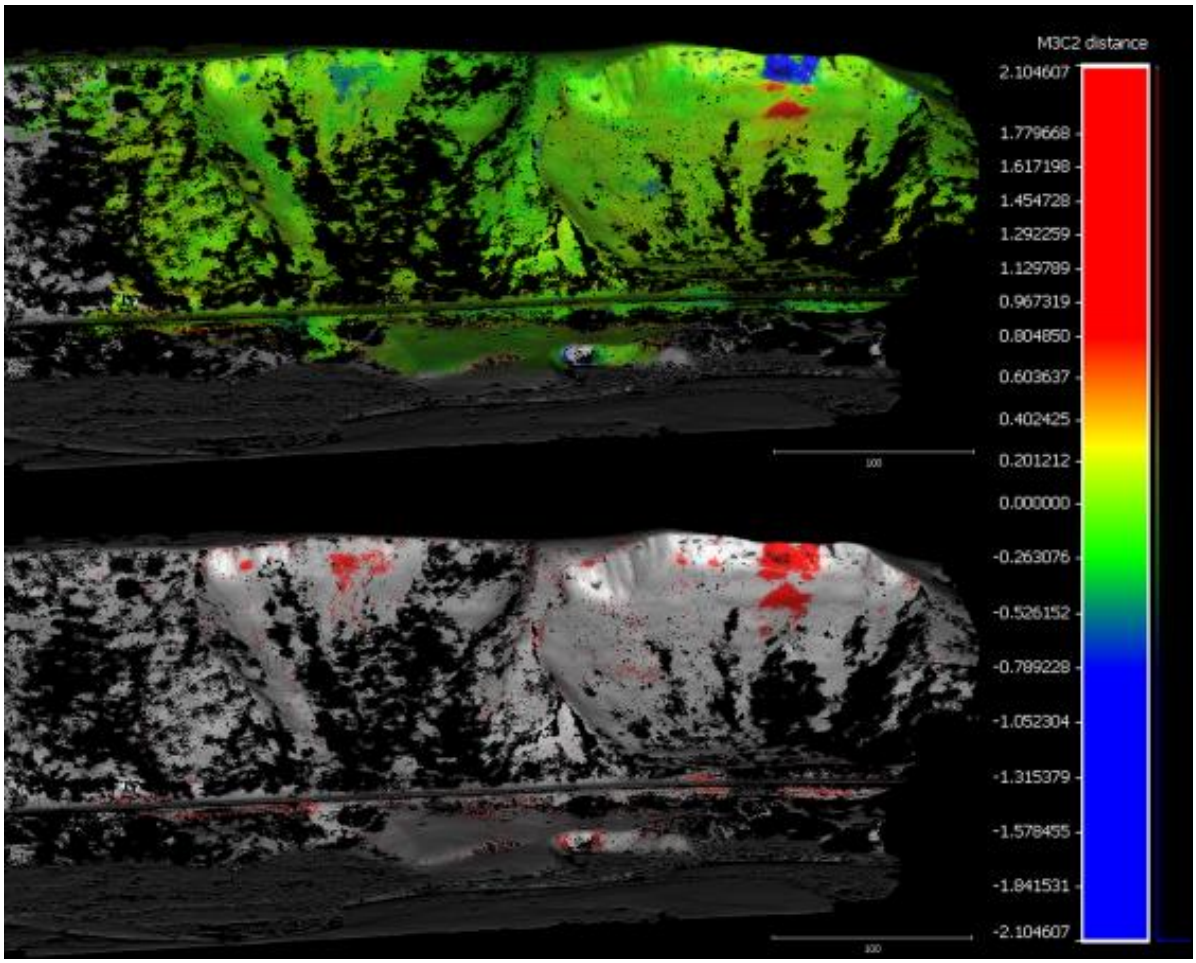

Figure 11. Deep Creek M3C2 (Top) and Significant Change results (Bottom)

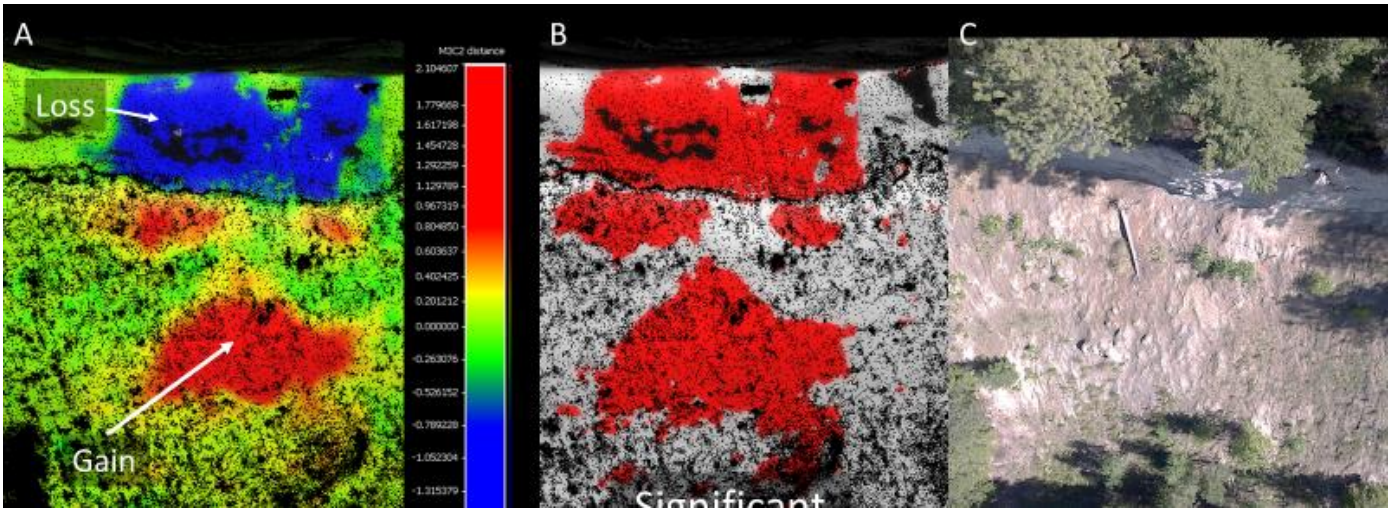

Figure 12. Deep Creek main area of interest along cliff face. (A) M3C2 results showing loss along the cliff face and deposition below (B) both of these displacements were identified as significant change. (C) RGB nadir image of the area.

The total volume change for this area of interest was a loss of ~13 m^3 with the total surface area of this section of the site is ~1,469 m^2. The total volume loss for the area was ~472 m^3 with a similar amount of gain at ~460 m^3.

2.3.2.2 Kootenai River M3C2 and Volume Results

For the Kootenai River Site the significant change values for the site ranged between ~0.25–1 m (Figure 13).

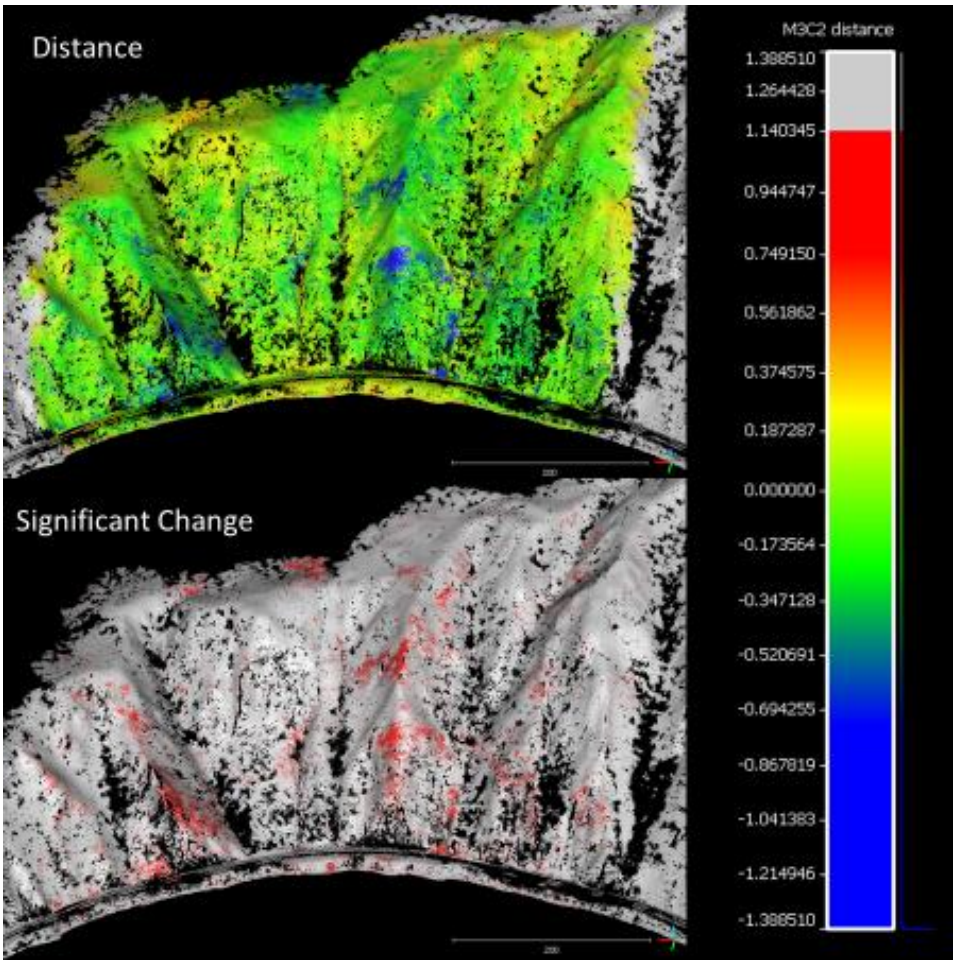

Figure 13. Kootenai River M3C2 (Top) and Significant Change results (Bottom)

The main area of interest at the Kootenai River site was a gulley near the railroad tracks, any debris that would flow down this gully would be deposited directly onto the railroad tracks.

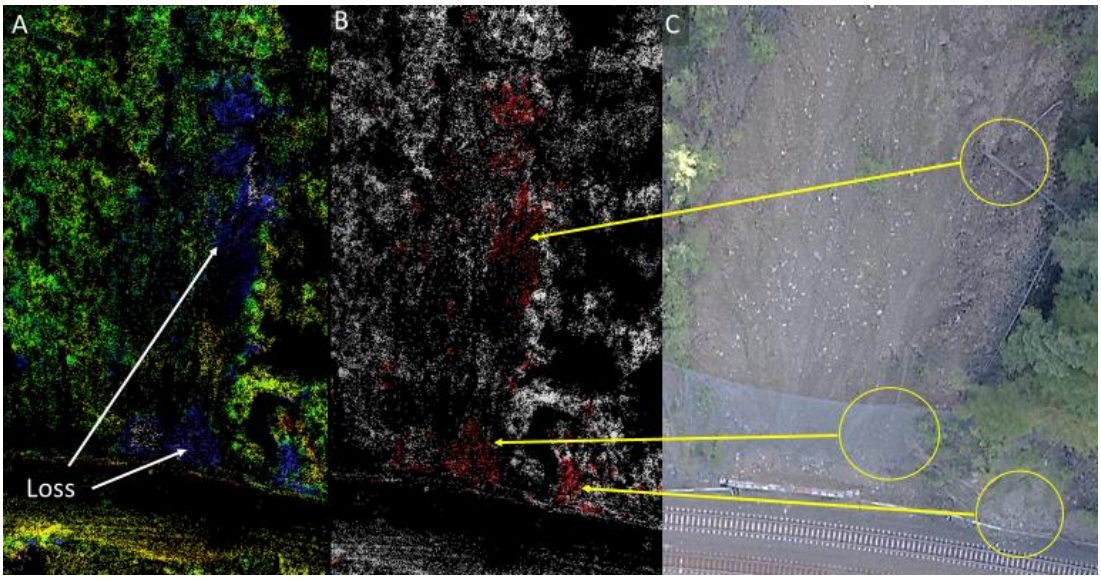

Figure 14. Area of interest at the Kootenai River site (A) M3C2 results showing loss along the railroad (B) All three of these displacements were identified as significant change. (C) Matching RGB nadir image of the area.

The three sections of significant change identified by the yellow arrows in the above image ranges from ~40-90 cm of displacement between the clouds (Figure 14). The total volume change for this area of interest was a loss of ~553 m^3 with the total surface area of this section of the site is ~2,434 m^2. The total volume loss for the area was ~733 m^3 with about 179 m^3 of volume gain near the bottom of the track.

2.3.2.3 Moyie River M3C2 and Volume Results

The significant change for the Moyie River site ranged between ~0.3–1 m (Figure 15).

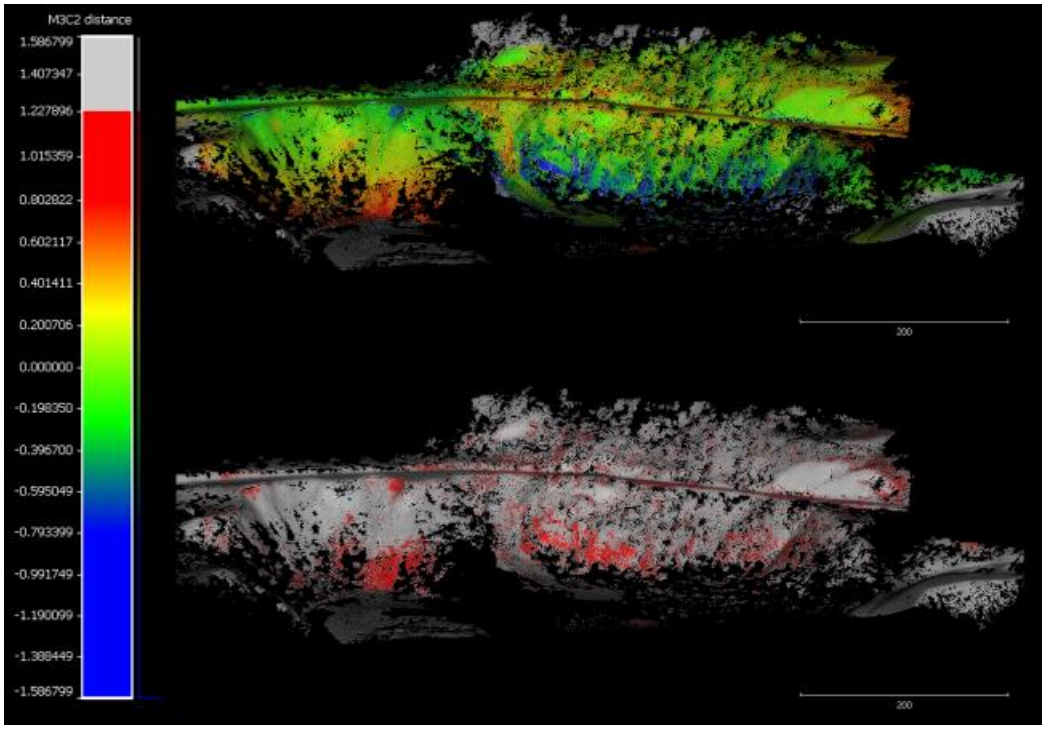

Figure 15. Moyie River M3C2 (Top) and Significant Change results (Bottom)

The main area of interest for this site is the location of the 2017 derailment on the slope right below the track. In this area the average loss was between ~0.5 and ~1 m (Figure 16). The bottom of the slope below this area of loss has an average gain of material between 0.5-0.8 m of material. The total volume change for the area of the 2017 derailment was a loss of ~ 358m^3 with the total surface area of this section of the site as ~2,513 m^2. The total volume loss for the area was ~500 m^3 with about 143 m^3 of volume gain.

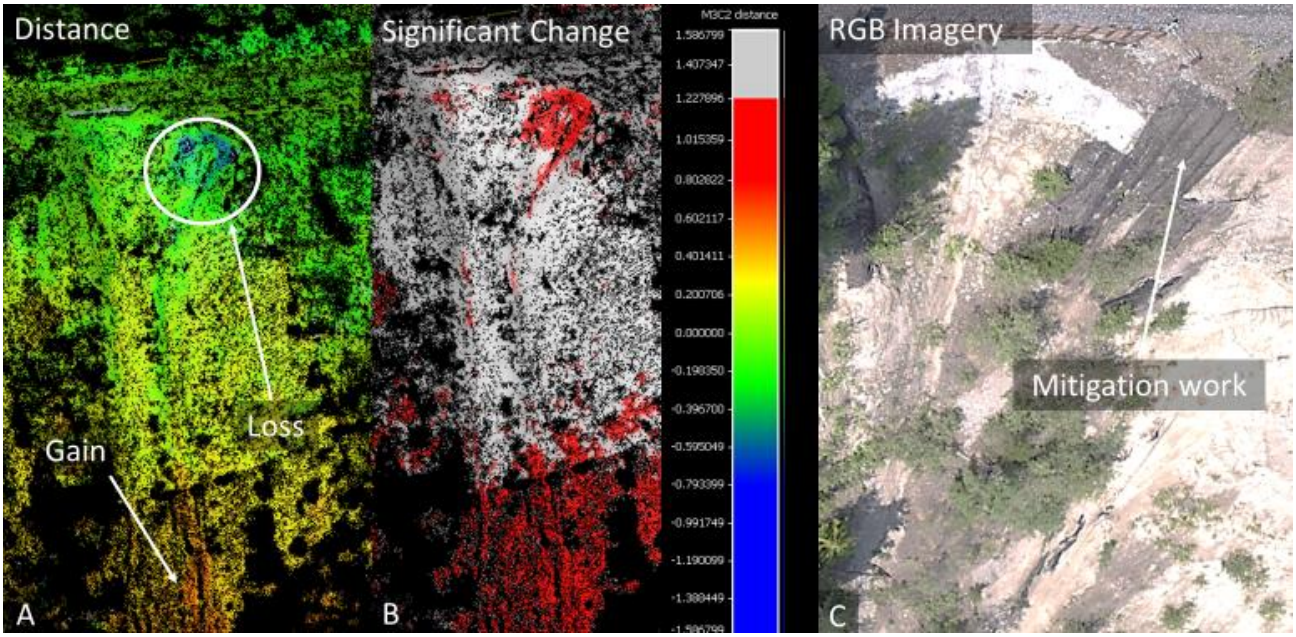

Figure 16. Area of 2017 derailment at the Moyie River site (A) M3C2 results showing loss along the railroad (B) This same area was identified as significant change. (C) Matching RGB nadir image of the area showing mitigation work.

2.3.3 Uncertainty Results

The M3C2 plugin in CloudCompare also generated uncertainty point clouds for each site. The distance uncertainty point clouds and corresponding histograms are displayed below. For the Kootenai River site the highest uncertainty values were found in the heavily vegetated gullies where there were holes in the dataset (Figure 17). As seen in the histogram a majority of the site has a distance uncertainty of less than 0.325 m (Figure 18).

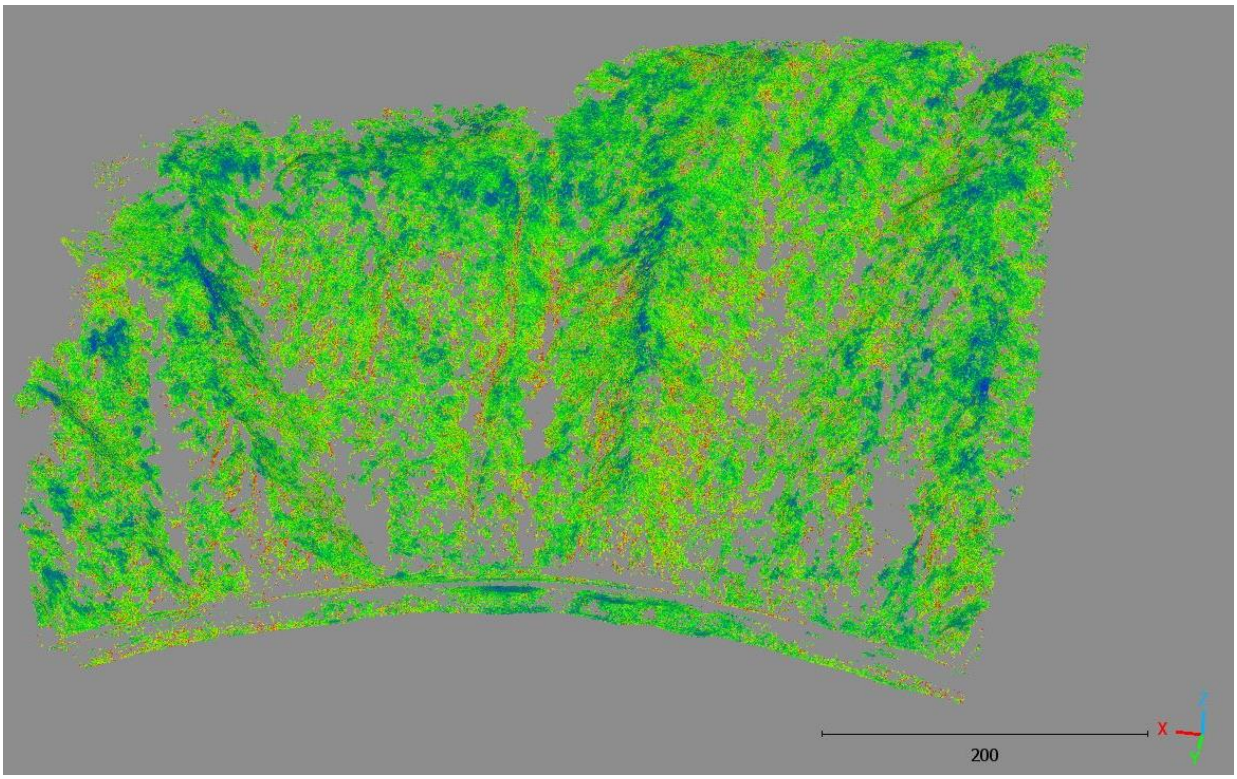

Figure 17. Kootenai River distance uncertainty point clouds

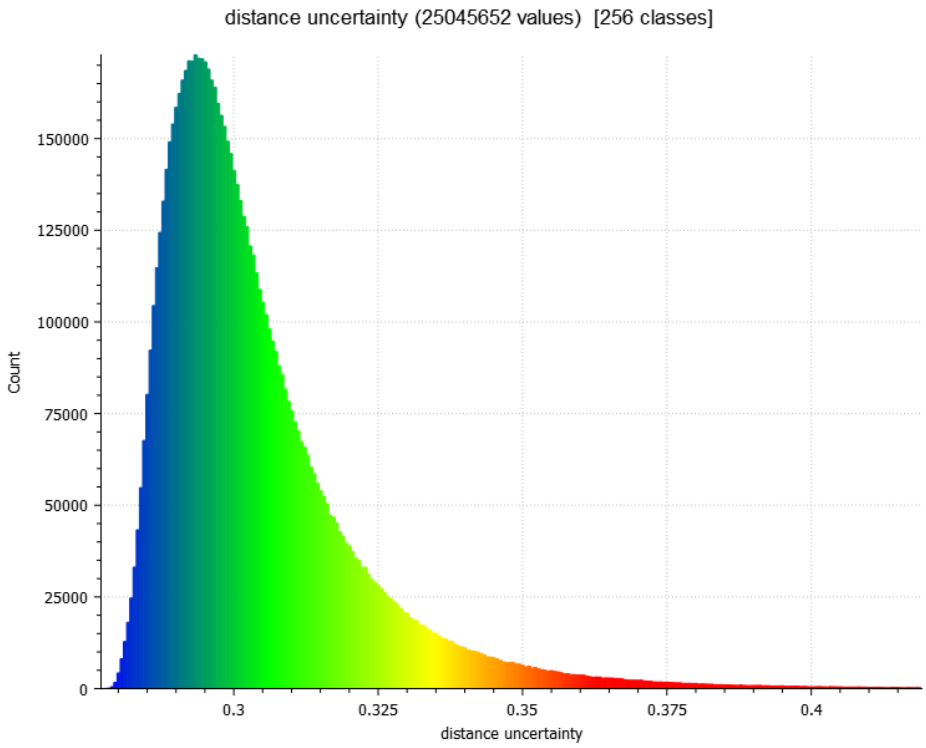

Figure 18. Kootenai River distance uncertainty histogram

The distance uncertainty results for the Deep Creek site are shown below. Similar to the Kootenai River site, the areas of the highest distance uncertainty are the edges of the holes where the vegetation was too thick for the two return LiDAR to penetrate (Figure 19). Overall, for the

site the majority has a distance uncertainty of less than 0.26m (Figure 20).

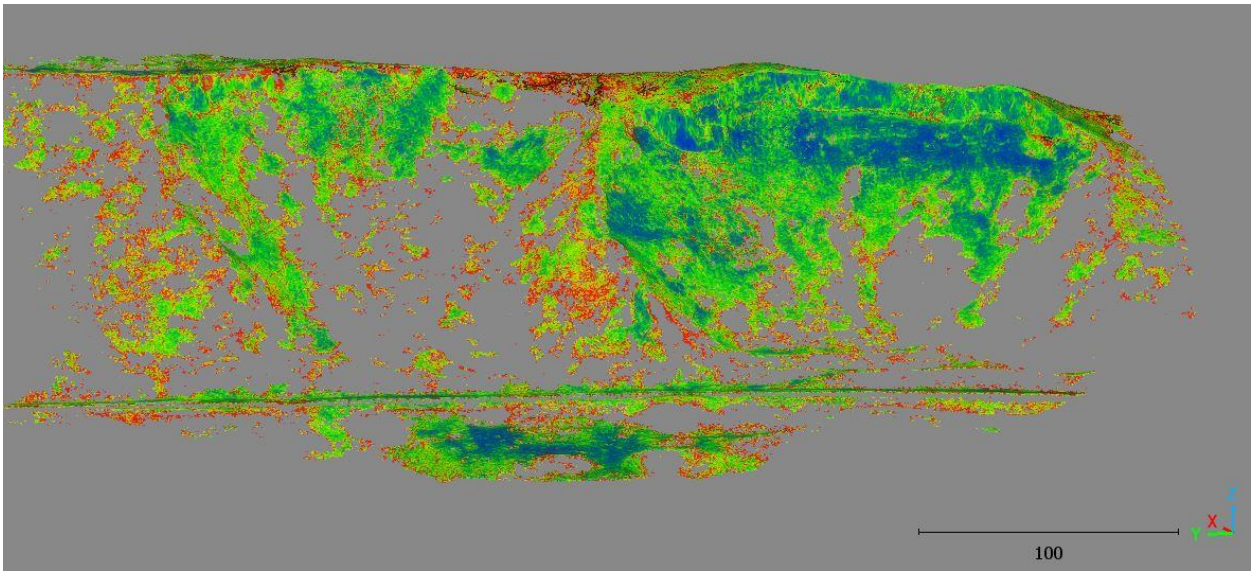

Figure 19. Deep Creek site distance uncertainty point cloud

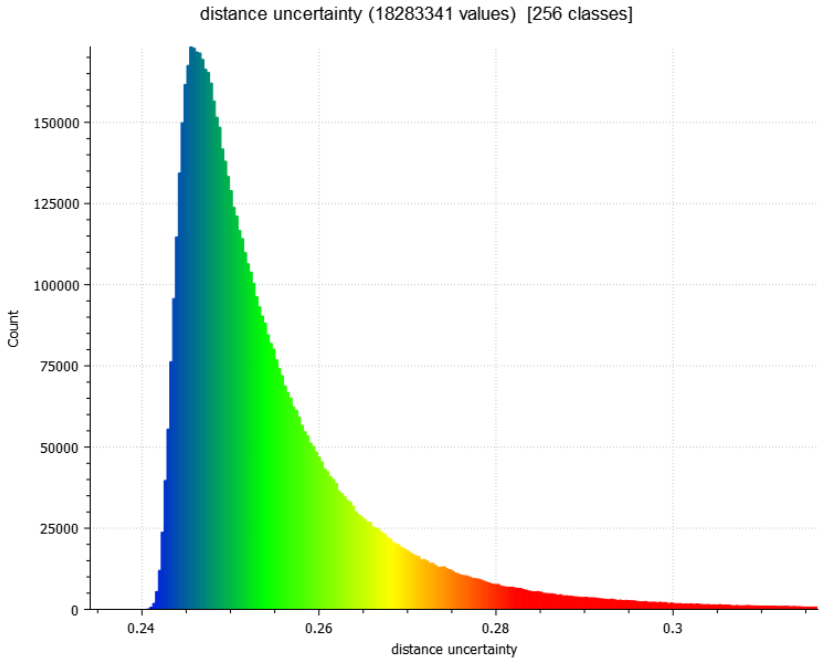

Figure 20. Deep Creek site distance uncertainty histogram

The distance uncertainty results for the Moyie River site are shown below. Similar to the Kootenai River site and the Deep Creek sites, the areas of the highest distance uncertainty are

where the point cloud is sparse (Figure 21). This site has the highest distance uncertainty of the three sites with much of the site having an uncertainty of less than 0.40m (Figure 22). This is likely because of the sparseness of the 2017 point cloud.

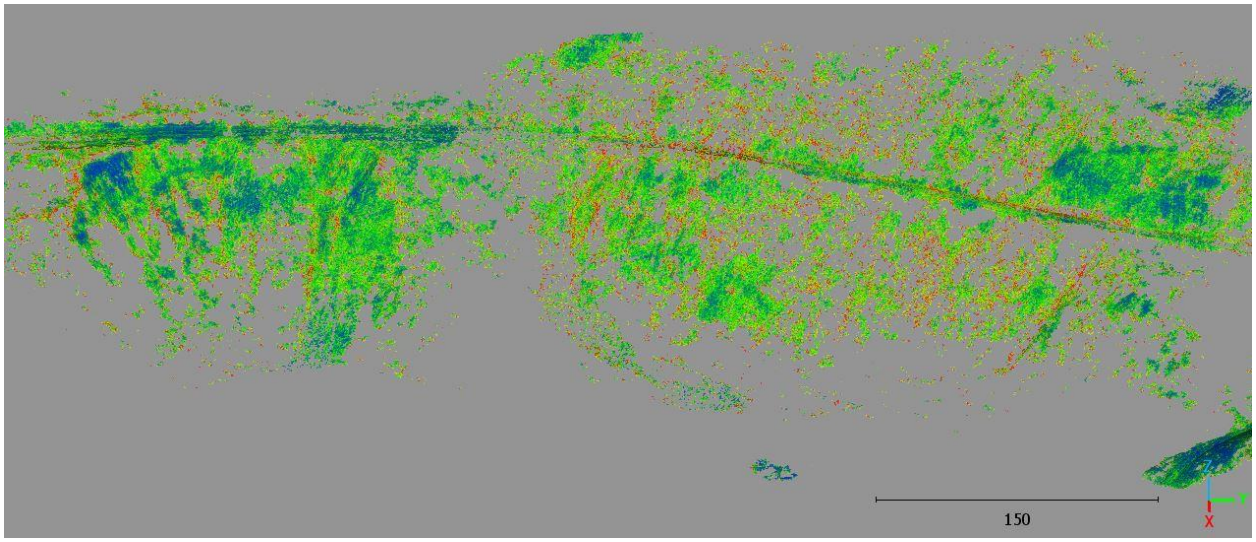

Figure 21. Moyie River site distance uncertainty point cloud

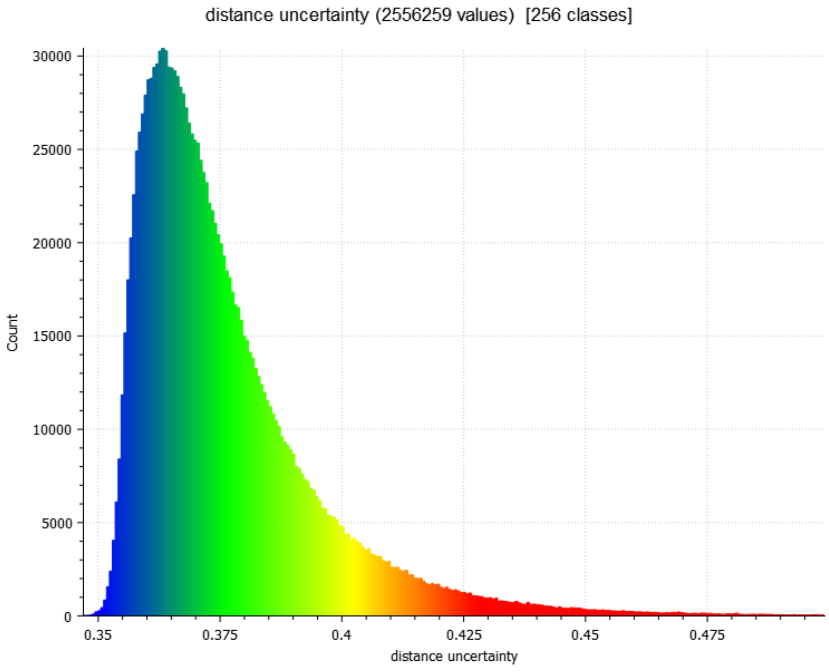

Figure 22. Moyie River site distance uncertainty histogram

2.4 M3C2 Discussion

Our method of post processing the LiDAR data was effective in eliminating the common issues associated with repeat LiDAR studies. The issues of differences in georeferencing information and different quantifications of uncertainty we resolved by processing the 2017 and 2021 LiDAR data with the methodology outlined in this chapter to optimize alignment for LiDAR datasets that do not have ground control. The issues of poor coregistration of flight lines and differences in data quality we solved using the stripping correction software BayeStripAlign2.1 to align the flight strips. This new methodology aligned the flightlines as closely as possible, removing the vertical and horizontal thereby improving the accuracy of the analysis. The overlap of the flightlines was improved and once loaded into CloudCompare, only the fine registration tool was needed.

The results of the M3C2 analysis and volume calculation showed that the workflow developed in this study is able to align repeat LiDAR point clouds accurately enough to detect significant change as low as ~25 cm. At the Kootenai site areas of loss revealed in the point cloud analysis can be visualized in the RGB imagery. While the algorithm measured the significant loss along the slope where there were small scarps; matching deposition of displaced material was missing. Most of the debris from these slides was removed by the railroad maintenance crews, however, there is a small amount of displaced material on the tracks can be seen in the lower right yellow circle (Figure 9). This deposition was not detected by the algorithm due to a hole in the point cloud that was caused by the retaining wall placed by the railroad company in-between 2017 and 2021. The results of the Moyie site could also have been affected by the sensor picking up on the mitigation measures implemented at the site. We measured significant loss in the area of the 2017 derailment with significant deposition at the

bottom of the slope. There have been extensive mitigation efforts on the upper slope, such as the installation of metal netting and retaining walls that could be affecting our measurements. The area at the bottom of the slope appears to act as a catchment for debris coming off the slope, not limited to the area of interest we focused upon (Figure 11). The Deep Creek area had by far the most significant change between all three sites and clearly shows the correlating deposition of the alluvium and colluvial material below the scarp. The fallen tree below this cliff face could also be a result of the material displacement at the site (Figure 7).

The further limitation of this study are the holes in the point clouds caused by the failure of the LiDAR sensor to penetrate dense vegetation. The dense vegetation led to some large holes in the point cloud that increase the error and uncertainty in our alignment and measurements. This issue was compounded for the 2017 flight campaigns which were flown with a larger side distance (50 m for 2017 vs. 21 m in 2021). Despite this limitation the average uncertainty for the three sites ranged from less than 26cm to less than 40cm. The areas of higher uncertainty are mostly located along the edges of the holes caused by the dense vegetation. Flying with a closer side distance improved the point cloud density in 2021 but reduced the coverage area and increased the number of flights required to cover the same area. New technology such as a sensor with more than two returns or a sensor with more laser channels such as the VLP-32 could further penetrate the vegetation and improve accuracy by gathering more points per second. This along with a set altitude above ground for further flight campaigns to match that of the previous flight campaigns would be an improvement to future studies involving repeat LiDAR.

Chapter 3: Object Based Image Analysis

3.1 Introduction

Object-based image analysis (OBIA) is a method of feature extraction at an object level involving multiresolution segmentation and the classification at an object level instead of a pixel level (Karantanellis et al., 2020; Hossain and Chen, 2019; Anders et al., 2013) In their 2013 study, Anders et al, used LiDAR digital terrain models (DTMs) to detect geomorphological change in Gargellen Valley Australia from 2003 and 2011. From these DTMs, the authors mapped seven features: fluvial incisions, glacially eroded bedrock, recent fluvial deposits, alluvial fans, fluvial terraces, flow/slide deposits, and slopes subject to shallow landslides using stratified object-based image analysis, as well as calculating the volumetric change of the features. These seven features were placed into categories using a geomorphogenetic classification scheme and a stratified feature extraction approach with eCognition software (Anders et al., 2013). Karantanellis et al. (2020) used a similar method based on human cognition and the recognition of landslide precursors. In this study, the authors used UAS gathered 3D point clouds in combination with OBIA to conduct site specific landslide assessment. The first step was generating ortho-photos and the DSM derivatives from the collected point clouds. The authors then fused the different layers together before segmenting them. Based on morphological parameters, these segments were then classified into landslide characterization categories using rulesets (Karantanellis et al., 2020). These adaptive rulesets use expert knowledge to create a set of rules that group the objects or segments into useful categories (Karantanellis et al., 2021). This OBIA method was shown to be superior in building a realistic scheme for landslide assessment than other pixel based methods such as weighted overlay model (Karantanellis et al., 2020).

3.1.1 Definition of susceptibility, risk, and hazard for landslide mapping

The terms susceptibility, hazard, and risk are often used interchangeably in literature pertaining to landslides and the threat posed to infrastructure, the environment and people (Wubalem, 2021; Wang et al., 2012; Gorsevski et al., 2016). According to the USGS Landslide handbook (2008) *susceptibility maps* show areas of mass movement potential based on the environmental factors present at the site but not necessarily the probability of the failure occurring (Highland and Bobrowsky, 2008; Abbaszadeh Shahri et al., 2019). *Hazards maps* are expected to include information pertaining to the likelihood or probability of landslide activity over a defined period of time (Highland and Bobrowsky, 2008; Chung and Fabbri, 2003) Thus, a susceptibility map can reveal the spatial occurrence of landslide events and a hazard map describes the spatiotemporal occurrence of events over a terrain (Wubalem, 2021; Azarafza et al., 2021). A hazard map includes areas of mass movement initiation and the runout zone of the movements (Highland and Bobrowsky, 2008). Finally, *risk* is typically defined as the product of the probability of an event to occur and the severity or consequences for human life or damage to infrastructure (Highland and Bobrowsky, 2008; Abdulwahid and Pradhan, 2017). In this study we are generating susceptibility maps based on the presence of environmental factors that contribute to rockfall, landslide initiation, and deposition zones.

Areas prone to mass movement hazards can undergo mitigation or adaptation measures (Oktorie, 2017; Gariano and Guzzetti, 2016). Drawing from climate change and landslide terminology, *adaptation* often refers to actions made at a through policy or regulation to human systems with the goal to reduce or avoid damage from hazards (Kim et al., 2018; IPCC, 2012; Ahmad et al., 2020). For mass movement areas along railway corridors, this includes methods such as changes in land use planning and zoning, climate change regulation, relocation of

buildings, and improvements to drainage (Oktorie, 2017; Jakob, 2022). *Mitigation* refers to structural measures taken to prevent the hazard from reoccurring, for example using rock anchors, shotcrete, and controlled blasting to prevent material from detaching from the cliff face (Jakob, 2022; Oktorie, 2017; IPCC, 2012; Highland and Bobrowsky, 2008; Gariano and Guzzetti, 2016).

3.1.2 Landslide Susceptibility Environmental Factors

We investigated numerous different environmental factors that influence landslide susceptibility at the site to use in the OBIA analysis. These layers included: canopy height, slope, aspect, plan curvature, profile curvature, and flow accumulation. Canopy height is an important aspect of slope stability since vegetation prevents erosion and weathering of slopes (Raghuvanshi et al., 2015) Aspect refers to the direction the slope faces and is another environmental factor that influences landslide potential of a site since it directly impacts weathering and vegetation through evapotranspiration (Esri; Mahalingam et al., 2016). Profile curvature is the curvature that is parallel to the direction of the maximum slope and determines the acceleration of flow downslope (Esri). Plan curvature is the curvature that is perpendicular to the slope, a negative profile curvature indicates a gully (Esri). This curvature influences the convergence of flow, or in this case, those areas that provide an easy avenue for mass movements downslope.

For landslide susceptibility, the traditional belief is that the steeper the slope the greater the landslide potential; this idea is expressed in studies by Hussin et al. (2012) and Sarkar and Kanungo (2004). However, numerous other studies have shown that there is a window of ideal slopes for landslide initiation. A 2002 study in Turkey by Ercanoglu and Gokceoglu (2002) showed that landslide frequency peaked at slopes between 26° and 30° and sharply decreased

over 45°. A similar study by Arnous and Green (2011) generated similar results in that the frequency of landslides was high between 20° to 30° and lower frequency between 12° to 20° and 35° to 41°. The results of this study have even been used to guide classification in another study by Omran et al. (2021). Studies by Wang et al. (2010) and Cao et al., (2021) determined that the the frequency of landslides is highest between 20° to 40°. These are the studies that our slope weights are based off and we used to determine that slopes with an inclination between 20° to 40° have high rockfall susceptibility, an inclination between 40° to 50° have a moderate susceptibility (Cao et al., 2021; Wang et al., 2010; Omran et al., 2021; Arnous and Green, 2011).

As discussed earlier, vegetation helps prevent erosion and weathering as well as improving cohesion and improving shear resistance, so the potential for landslides decrease where vegetation is present (Raghuvanshi et al., 2015; Vorpahl et al., 2012). The larger the vegetation, the better the protection from these processes. A high flow accumulation indicates area where water converges and can saturate the soil, reducing shear strength of the ground (Wachal and Hudak, 2000).

3.1.3 Rockfall Susceptibility Environmental Factors

The second mass movement type modeled in this study is rockfall. There are multiple parameters that increase likelihood for rockfall, this includes things such as lithology, fracturing, cohesion, and friction angles of the rock (Volkwein et al., 2011). However, the determination of these mechanical properties and fracturing of the rocks would require field investigation which was too dangerous for these sites. Therefore, the parameters that we used for this ruleset were slope, vegetation, aspect, profile curvature, and plan curvature.

As with landslides, for rockfall the major parameter is slope, the higher the slope the more likelihood of rockfall (Hussin et al., 2012). A majority of studies agree that the highest risk for rockfall occurred in areas of slopes greater than 45 degrees. A study by Saroglou et al. in 2019 determined that rockfalls occurred in slopes with inclinations between 45° to 90° (Saroglou, 2019). A similar study by Fanos et al. in 2019 described slopes between 51° to 79° to be ideal for rockfall (Fanos et al., 2019). The study by Omran et al. in 2021 determined that slopes with an inclination between 25°-35° have a moderate rock fall susceptibility, an inclination between 35°-45° has a high susceptibility, and greater than 45° has a very high susceptibility (Omran et al., 2021). These studies generally agree that the susceptibility of rockfalls increase as the slope increases; for this reason, two slope categories of increasing weight were used.

Aspect is another important parameter in rockfall susceptibility because of its relation to precipitation, solar radiation, evapo-transpiration, and freeze-thaw cycle. The southern slope historically receives more precipitation and sun, leading to alternatingly wet and dry slopes so are more prone to rockfalls (McClelland et al., 1999; United States Department of Agriculture Forest Service and Boise National Forest, 1995). When looking at the Idaho landslide inventory, recorded landslides in the panhandle occurred more frequently on the southern slopes than other aspects (Lifton et al., 2020). For this, a weight of one was given for slopes with a southern aspect.

Since rockfall occurs mostly where the bedrock is exposed, there should be little to no vegetation in the area. Slope and terrain roughness both influence erosion and water infiltration, which breaks apart the rock, leading to loose pieces of material that can be brought down by gravity. We used the same cutoff values for the rockfall ruleset as the landslide ruleset.

A negative plan curvature, indicates areas of curvature that are concave and flow converges (Esri). These areas of flow convergence can act as a funnel downslope for rocks or debris. Profile curvature determines whether flow down the slope accelerates or decelerates. The concave slopes with a positive profile value indicate that debris would accelerate downslope towards the tracks (Fanos et al., 2019; Kopp, 2021; Esri). Profile curvature was used not only because of the role that it plays in acceleration, but also its ability to identify the small ledges on steep cliff like rock faces.

3.1.4 Deposition Susceptibility Environmental Factors

Slope was again the most important parameter for this ruleset. Based on studies of talus slopes, we were able to determine the likely maximum angle of repose for rock debris to be about 35° (Carson, 1977; Francou and Manté, 1990; Jaboyedoff and Labiouse, 2011). The minimum slope of 10° eliminated the artificially flat railroad area. Vegetation can impede the flow of debris, so areas with little vegetation would provide an easier path for debris to travel. Lack of vegetation can also be indicative of previous deposition in the area. For this model, areas of no vegetation were given a weight of +1. Areas of low slope can also act as a catchment area for upslope debris.

Gullies are often routes for debris to travel down and deposit on the tracks. Flow accumulation shows where the erosion from flowing water is likely to form gullies (Fanos et al., 2019; Mahalingam et al., 2016). This water can easily bring debris along in a flow or when the gullies are dry rocks can easily tumble down. A negative plan curvature, indicates areas of curvature that are concave and flow converges (Esri). These areas of flow convergence can act as a funnel downslope for rocks or debris.

The last parameter used for this ruleset is flow accumulation. Flow accumulation is calculated as the amount of flow into a cell from upslope, a higher value indicates a concentrated flow whereas very low flow accumulation indicates ridges or other topographic high points (Esri). For this ruleset, a high flow accumulation indicates areas where debris, as well as water, might concentrate and settle.

3.1.5 Goals and Objectives

Mapping mass movement susceptibility is an important aspect of managing geohazards along transportation corridors. Knowing where the conditions are ideal for initiating these mass movements and where deposition is likely is important for installing mitigation measures. For this project we modeled mass movement susceptibility at three sites along the Kootenai River, Deep Creek and Moyie River corridors with object-based image analysis (OBIA). We used topographic parameters such as canopy height, slope, aspect, plan curvature, profile curvature, and flow accumulation derived from UAS LiDAR to develop expert system rulesets to classify rockfall, landslides and deposition areas across three study sites using OBIA. We created three classification rulesets for each site: landslide initiation areas, rockfall initiation areas, and deposition areas. To validate these rulesets, the results of the models for each site were compared to areas that had undergone change between 2017 and 2021 as identified in Chapter 2. With these expert-derived rulesets railroad companies can map these susceptible slopes when planning mitigation and adaptation strategies.

3.2 Methods

3.2.1 Landslide Characterization of Study Sites

Three sites along the Kootenai River, Deep Creek, and Moyie River were chosen for this study (Figure 23). The Kootenai River landslide site is composed of till deposits (~1-50 m thick) on top of members of the Belt Super group with sections of the site composed of exposed intrusive mafic sills. These till deposits are composed of material ranging from silt to cobbles while the members of the Belt super group are feldspathic quartzites and argillites of the Prichard Formation (Breckenridge et al., 2012; Burmester et al., 2010b). Based on this information and the imagery of the sites where bedrock and other coarse material was the main ground cover, we concluded that rock and debris are the two most present material types. The next aspect of the site we looked at what type of movements were occurring at the site. The mass movements that were mostly composed of debris material were relatively small failures forming long narrow paths contained mostly to the gullies of the site. While the areas of exposed bedrock are mostly bedded and jointed slopes overhanging the tracks. However, the orientation of these joints and bedding planes indicate that topple is not as likely as a mass movement at the site. Therefore, we concluded that the two types of mass movements at the site were rockfall and debris flow.

The Deep Creek site is composed mostly of alluvial and colluvial deposits (~10 m thick) (Barton et al., 2004; Burke et al., 2009; McFaddan et al., 2009). According to the geological map, these deposits ranged in size from silt to gravel. Looking at the imagery for the site, a majority of the material appears to be very fine with occasional sections of coarser material. We concluded that the material is earth. The movement at the site was determined to be a rotational slide based on the size and slight backward tilt of the displaced material. Therefore, the mass movement was an earthslide with the potential for earthfall along the steep scarp.

The main material at the last site along the Moyie River was mostly glacial outwash deposits with a size range between silty and sandy gravel. The area above the tracks is mostly boulder lodgment till with exposed mafic intrusive rock toward the northern end of the site. The presence of this exposed bedrock has led to larger boulders breaking off and being deposited downslope. These larger chunks of bed rock mixed with gravel sized glacial deposits creates a coarse debris material. The mass movements at the site are thus mostly slides and falls. Looking at the imagery the two mass movements on the northern end of the site, the deposition partner has an interesting hourglass shape reminiscent of flows and are located beneath a manmade drainage pipe yet water does not appear to be a major factor at the site. The 2017 derailment area is large, possibly the result of repeated slides over time and composed mostly of debris material. The areas of exposed bedrock above the track are likely to fall rather than topple because of the positioning of the joint sets and fractures. Therefore, the two mass movement types present at the site are rockfall and debris slides.

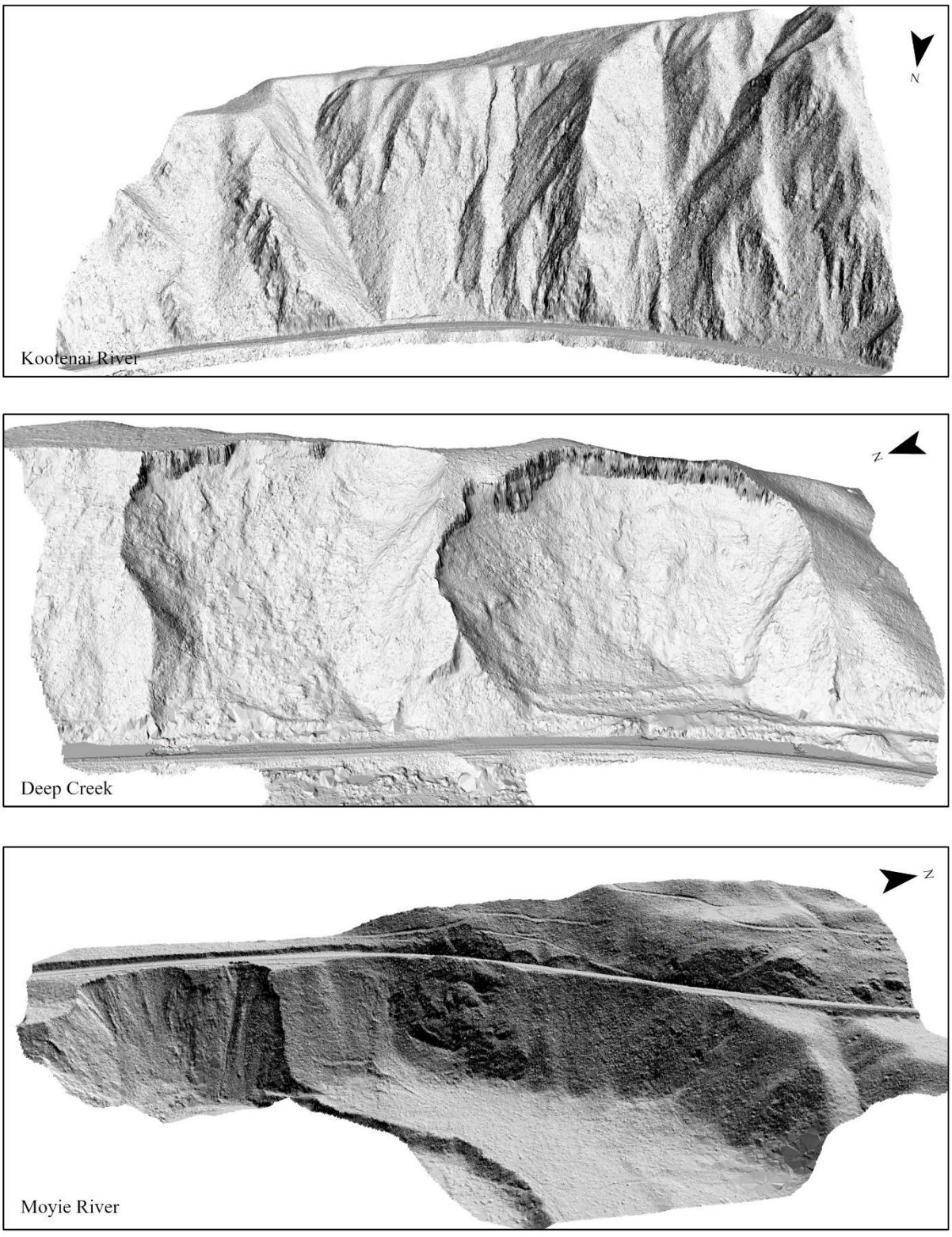

Figure 23. Hillshades of the three study sites

3.2.1 UAS Platforms and Sensors

The UAS platform used in this study was the DJI Matrice 600 Pro. Both are compact and only need a small takeoff and landing site due to their multi-rotor feature, but they are limited by their short flight time (~ 15 minutes), short flight range, and reduced stability in high winds compared to fixed wing UASs. Refer to chapter 2 for UAS platform and sensor information.

3.2.1 LiDAR Post Processing

The first step in processing the LiDAR data was to create Smoothed Best Estimate of Trajectory (SBET) files from the flight GPS data using the software PosPac UAV (v. 8.4). PosPac UAV software uses the IMU and GNSS data to georeferenced the flight data without the use of ground control points, since the sites were too hazardous for the placement of ground control points. This method not only improves the accuracy but can fill any gaps in the GNSS data that are caused when connection is temporarily lost with the rover during a flight (Applanix, 2020). LiDARtools georeferences the point clouds by matching the timestamps from the LiDAR returns with the timestamps from the Applanix APX-15 data in the SBETs (VanValkenburgh et al., 2020; Jacobs et al., 2021). Before exporting the LAS files, we had to adjust the roll of the UAS to 86.8° and the pitch to 0.12° in LiDAR tools. The final output LAS files were projected in WGS84 UTM Zone 11N. (ESPG:32611).

Since the LiDAR data comes out of LiDAR Tools in a GPS time format specific to LiDAR Tools, the global encoding needs to be set and the GPS time translated to a format that can be read by other software using LASTools. This process is laid out in detail in Appendix II. Before continuing to process the point clouds in LASTools, the flightlines need to be aligned. In order to make sure that the flight lines of the UAS are as closely aligned as possible thereby increasing

the accuracy of the data and removing any bias from the repeat LiDAR, we used a stripping correction software called BayeStripAlign2.1 to align the flight strips. These point clouds were then processed in LASTools to classify the points as either vegetation or ground and create the bare earth models and digital surface models which were exported as TIFFs.

3.2.2 OBIA Analysis

3.2.2.1 Generate Map Layers

To begin the OBIA process, we created the individual map layers of the different environmental factors that influence landslide susceptibility. Based on the surrounding environment of the sites we chose the following environmental parameter data layers for analysis: canopy height, slope, aspect, plan curvature, profile curvature, and flow accumulation. We imported the DSM and DEM TIFFs into ArcGIS Pro with a projected coordinate system of WGS 1984 UTM Zone 11N. The Extract by Mask tool was used to clean up the TIFFs and reduce any edge effects in the analysis. We carefully reviewed the TIFFs for each site and any local noise was removed with a pixel editor. We ran the fill tool on the rasters to fill in the smaller holes or gaps in the data. After cleaning and filling the two raster layers, we used the hillshade tool to create hillshade maps for both the DSM and DEM. Hillshade maps show the illumination and shadows of each pixel from a simulated light source which allows for better visualization of the terrain (Esri). These hillshade maps also helped illustrate what areas of the site had a higher resolution than others.

We generated a canopy height model that showed areas of the site that are covered in vegetation by subtracting the bare earth model from the DSM. Next, we calculated the slope of the site using the bare earth model and ArcGIS Pro's surface parameters tool. This surface

parameters tool improves on the issue of distance distortion inherent to projected coordinate systems by running all calculations in geodesic space. The last major improvement over the old slope and other surface tools is that a quadratic surface fit the neighborhood instead of a plane, which is more accurate for complex terrain (Kopp, 2021). Aspect was calculated using the surface parameter tool on the bare earth model to calculate the aspect of each cell in the raster. Often this would then be classified into the four cardinal directions, however, the aspect layer was left reclassified so that slopes with a south aspect have a value of 1 and all other aspects have a value of zero for the OBIA.

We also created two data layers for curvature at the site using the surface parameters tool in ArcGIS Pro: profile and plan curvature. Curvature is calculated on a cell by cell basis looking at the closest neighbors of the cell and calculating the ideal osculating circle that matches the curvature of the surface (Esri; Kopp, 2021). Consequently, a smaller circle means a larger curvature value (Kopp, 2021). A positive curvature value indicates a convex surface, whereas a negative curvature value indicates a concave ground surface (Esri).

To calculate the flow accumulation data layer, we first ran the flow direction tool followed by the flow accumulation tool on the filled bare earth raster. The flow direction tool uses the D-infinity method to create a raster that models the flow direction from every cell to the nearest downslope cell that has the steepest slope (Esri). ArcGIS Pro's flow accumulation tool uses the raster layer created by the flow direction tool to calculate the accumulated water flow in each cell with the D-infinity method (Esri). Lastly, the Extract by Mask tool was used to clean up the TIFFs and reduce any edge effects in the analysis.

3.2.2.2 Multiresolution Segmentation

We exported each of the individual raster layers from ArcGIS Pro as TIF files and imported them into Trimble eCognition. A multiresolution segmentation was then run on selected layers. A multiresolution segmentation, according to eCognition, is a segmentation method that starts with a single pixel object and, depending on spectral and shape characteristics, this single pixel is merged with neighboring pixels or objects with similar characteristics. The layers used in this process were chosen based on the weight of their influence on mass movements as well as the best way to reduce any collinearity. For the landslide initiation zone map, the layers used for the segmentation were the canopy height model and slope. CHM was given a weight of 1 and slope a weight of 2. The rockfall initiation map used the CHM, plan curvature, profile curvature, and slope layers for the segmentation. The CHM, plan curvature, profile curvature layers were weighted with 1 and the slope layer which was weighted as 2. The deposition model used the slope, CHM, and plan curvature layers for the segmentation. For this segmentation we gave a weight of 2 to the slope layer while the rest of the layers had a weight of 1 (Table 4).

Each segmentation used a set scale parameter, a shape weight, and a compactness weight. The scale parameter determines the size/number of segments. A smaller scale parameter leads to a noisy analysis, but too large of a scale parameter oversimplifies the site. The shape weight is given a value between 0 and 1 with a higher value indicating the influence of the pixel value compared to the average standard deviation in the segmentation (Akcay et al., 2018; Happ et al., 2010). The compactness weight is similar in that the values are between 0 and 1; the higher the number the more compact the segments based on the length of the borders. Other combinations of scale parameters, shape weight, and compactness weight values were tested before we settled on the respective values which provided the best segmentation (Trimble Inc., 2019). In this case,

the Landslide ruleset used a scale parameter of 12, a shape weight of 0.4, and a compactness weight of 0.2. The rockfall ruleset used a scale parameter of 10, a shape weight of 0.2, and a compactness weight of 0.4. Finally, the deposition ruleset used a scale parameter of 12, a shape weight of 0.2, and a compactness weight of 0.3 (Table 4).

Table 4. Segmentation Parameters

Ruleset Segmentation	Rockfall	Landslide	Deposition
Scale Parameter	10	12	12
Shape	0.2	0.4	0.2
Compactness	0.4	0.2	0.3
Layers (weight)	CHM (1) Plan Curvature (1) Profile Curvature (1) Slope (2)	CHM (1) Slope (2)	CHM (1) Plan Curvature (1) Slope (2)

3.2.2.3 Assign Classes with OBIA Ruleset

To develop the rulesets based on each site's characteristics; a separate ruleset was developed for landslide initiation zones, rockfall initiation zones, and debris deposition zones. We then assessed the layers in ArcGIS Pro to determine the cutoff values for each layer. A point system was then used to create the different susceptibility classes with each parameter given a weight or point value and a symbol. These weight values and rulesets were verified by expert opinion.

3.2.2.3.1 Landslide Initiation Ruleset

The first ruleset we created was for areas with a potential to initiate landslide. The parameters that we used for this ruleset were slope, vegetation, and flow accumulation. After conducting an in-depth literature review and with expert input, the weights or point values were assigned (Table 5. Landslide initiation weights and symbols). Moderate slopes have a weight of

4 while ideal slopes have a weight of 6. High vegetation areas we assigned a weight of -1 while areas of no vegetation have a weight of 1. Flow accumulation was the last parameter to be assigned a weight of 1.

Table 5. Landslide initiation weights and symbols

Parameters	Weight/Points
Moderate Slope ($40 \leq \text{Slope} \leq 50$)	+4
Ideal slope ($20 < \text{Slope} < 40$)	+6
Little to No Vegetation ($\text{CHM} \leq 10$)	+1
High Vegetation ($\text{CHM} \geq 20$)	-1
Flow Accumulation ($\text{Flow Accumulation} \geq 1000$)	+1

The most important parameter for landslide initiation was slope, which was given the largest weight followed by vegetation and flow accumulation, which were given the same weight. With the exception of areas of tall vegetation which were assigned a weight of -1, the other parameters had a weight of 1.

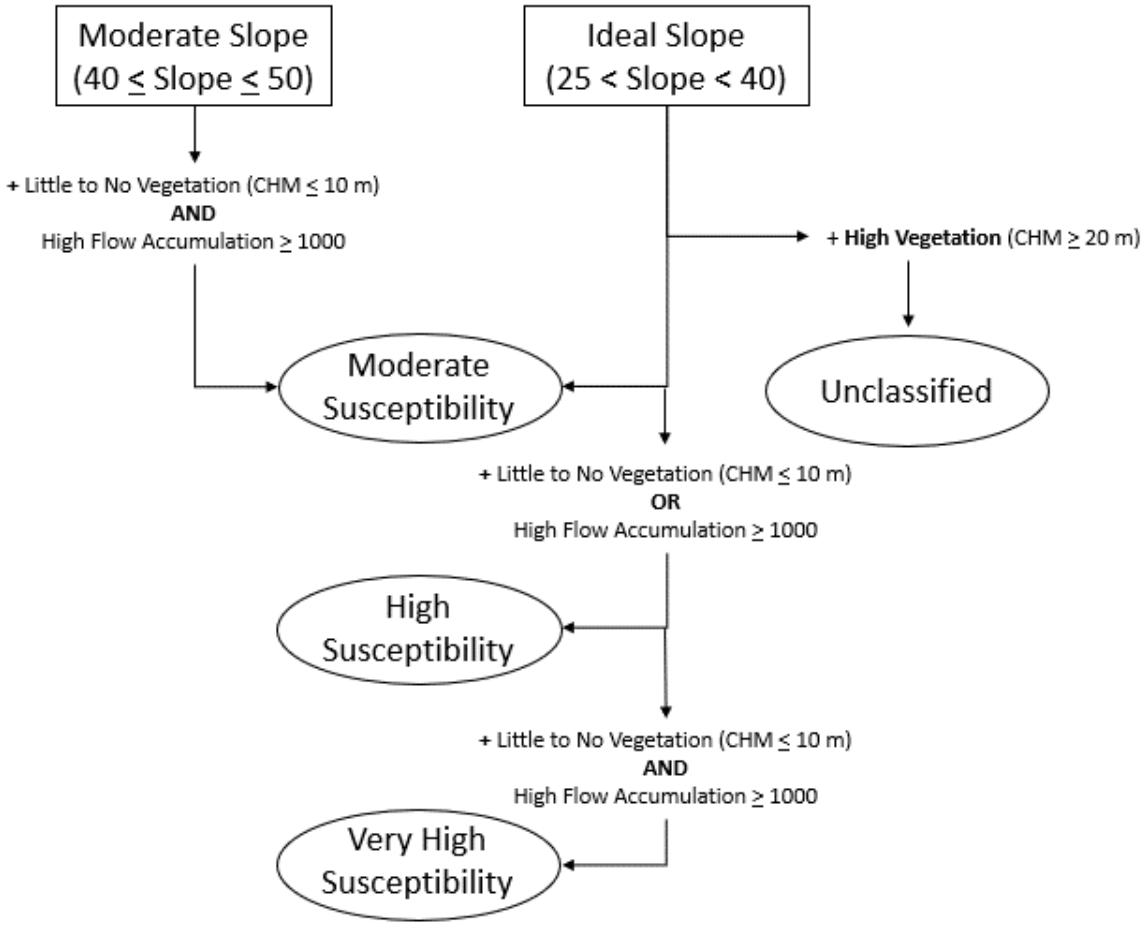

Figure 24. Landslide ruleset workflow for initial classification

This initial classification is shown in Figure 24 where the slope is the initial parameter used for classification followed by vegetation height and flow accumulation. The more parameters the object met, the higher the classification.

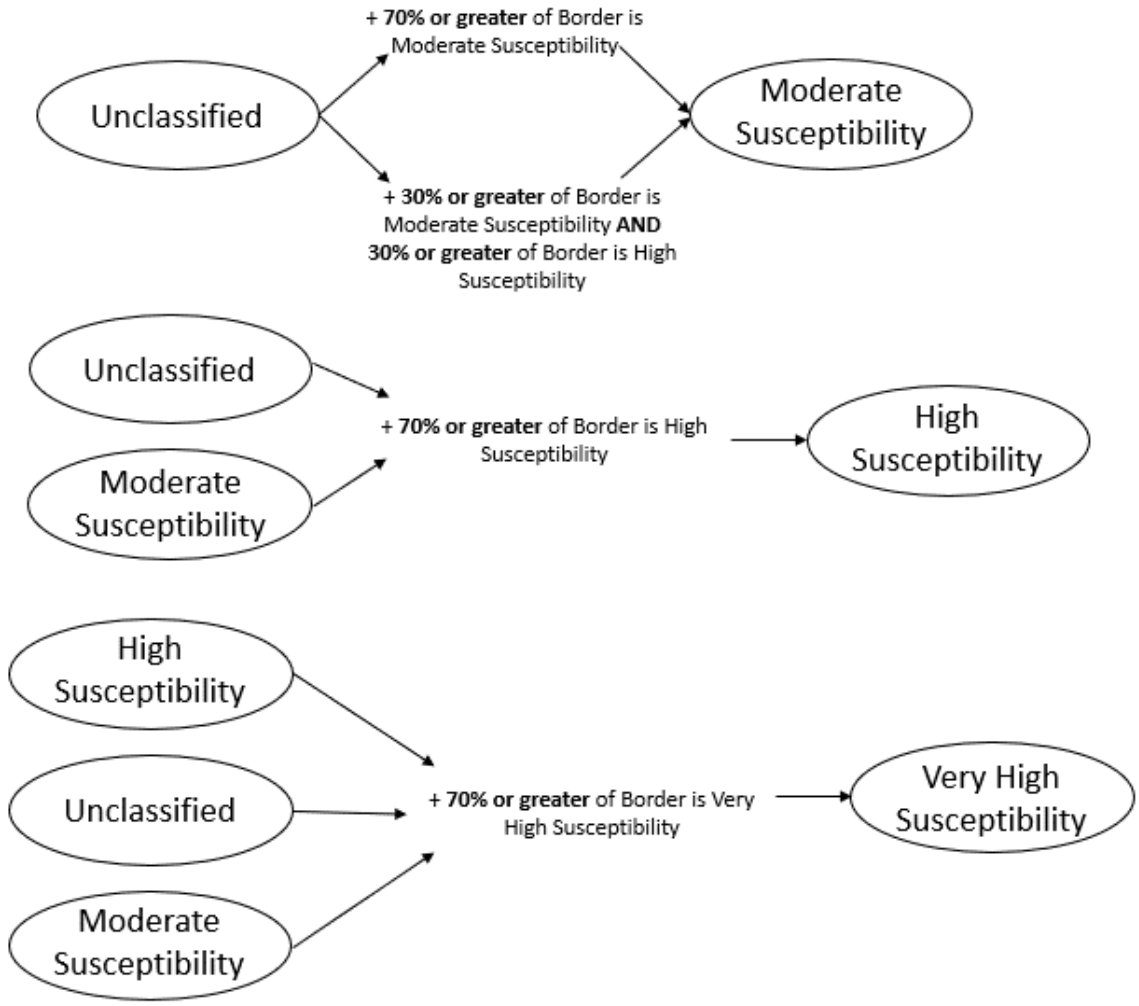

Figure 25. Continuation of landslide ruleset where the rules of this section are used to fill any holes in the classification.

The next section of the workflow is used to fill any holes in the model so polygons that almost entirely surrounded by other classified objects will be assigned to the same class (Figure 25). The last part of the ruleset removes the small, isolated polygons to reduce noise in the model (Figure 26).

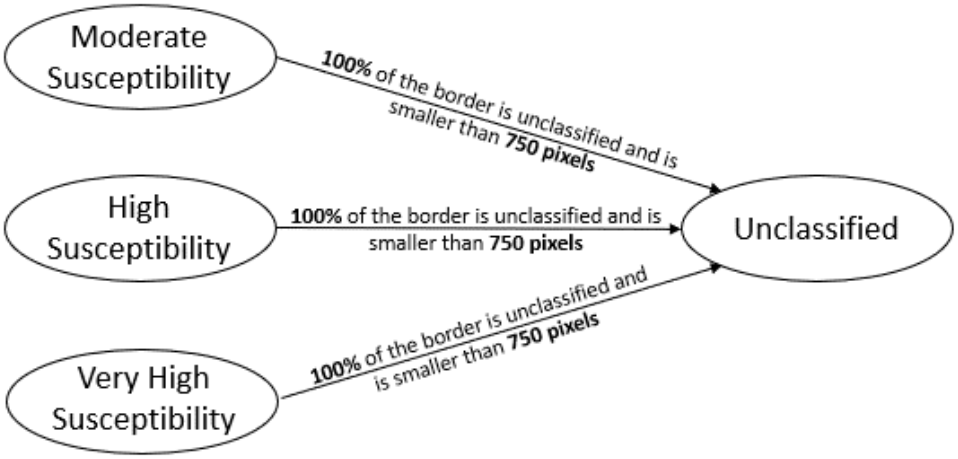

Figure 26. The last section of the Landslide Ruleset which reduces noise in the model by removing small isolated polygons.

3.2.2.3.2 Rockfall Initiation Ruleset

The second ruleset we created was for areas with a potential to initiate rockfall. After reviewing the literature and expert input, the weights or point values we assigned to the following parameters: slope, vegetation, aspect, profile curvature, and plan curvature. (Table 6. Parameter weights for rockfall initiation areas). Steep slopes have a weight of 5 while very steep slopes had a weight of 6. The rest of parameters were assigned a weight of 1.

Table 6. Parameter weights for rockfall initiation areas

Parameter	Weight/Points
Steep Slope (50 < Slope < 60)	+5
Very Steep Slope (Slope $\geq$ 60)	+6
Little to No Vegetation (Canopy Height $\leq$ 10)	+1
South Aspect	+1
Profile Curvature $\geq$ 0.06	+1
Plan Curvature $\leq$ 0.1	+1

Based on the weights of the parameter, the ruleset was written to first separate steep slope and the very steep slope into separate classes. Then based on how many of the additional parameters were met, the objects were placed into a rockfall susceptibility class (Figure 27).

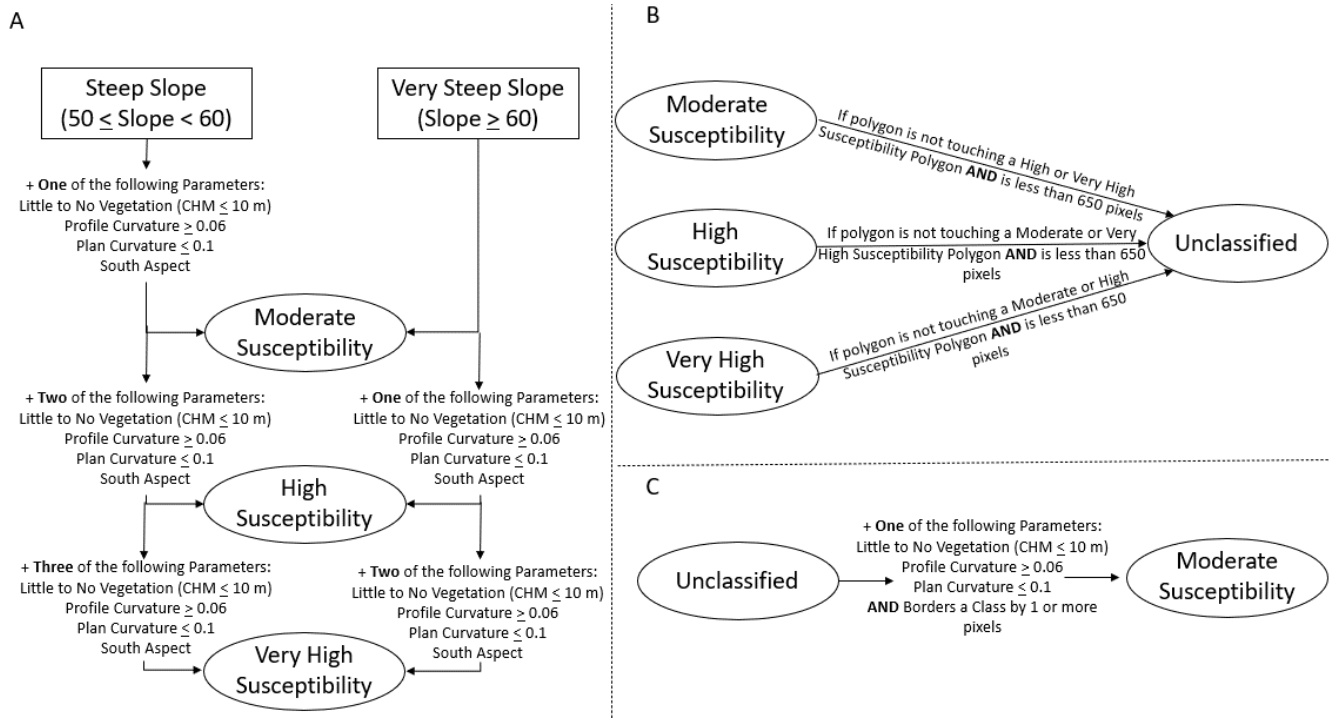

Figure 27. Rockfall initiation ruleset workflow. A. Initial classification based on slope and how many other environmental factor thresholds the object meets B. Remove small, isolated polygons C. Add in bordering objects that meet one of the rockfall susceptibility factors

After the initial classification, additional rules were used to close up any holes in the classification and reduce noise. To reduce noise small, isolated objects were removed while the "relative border to" and "border to" tools were used to fill gaps in large polygons (Figure 27 and Figure 28).

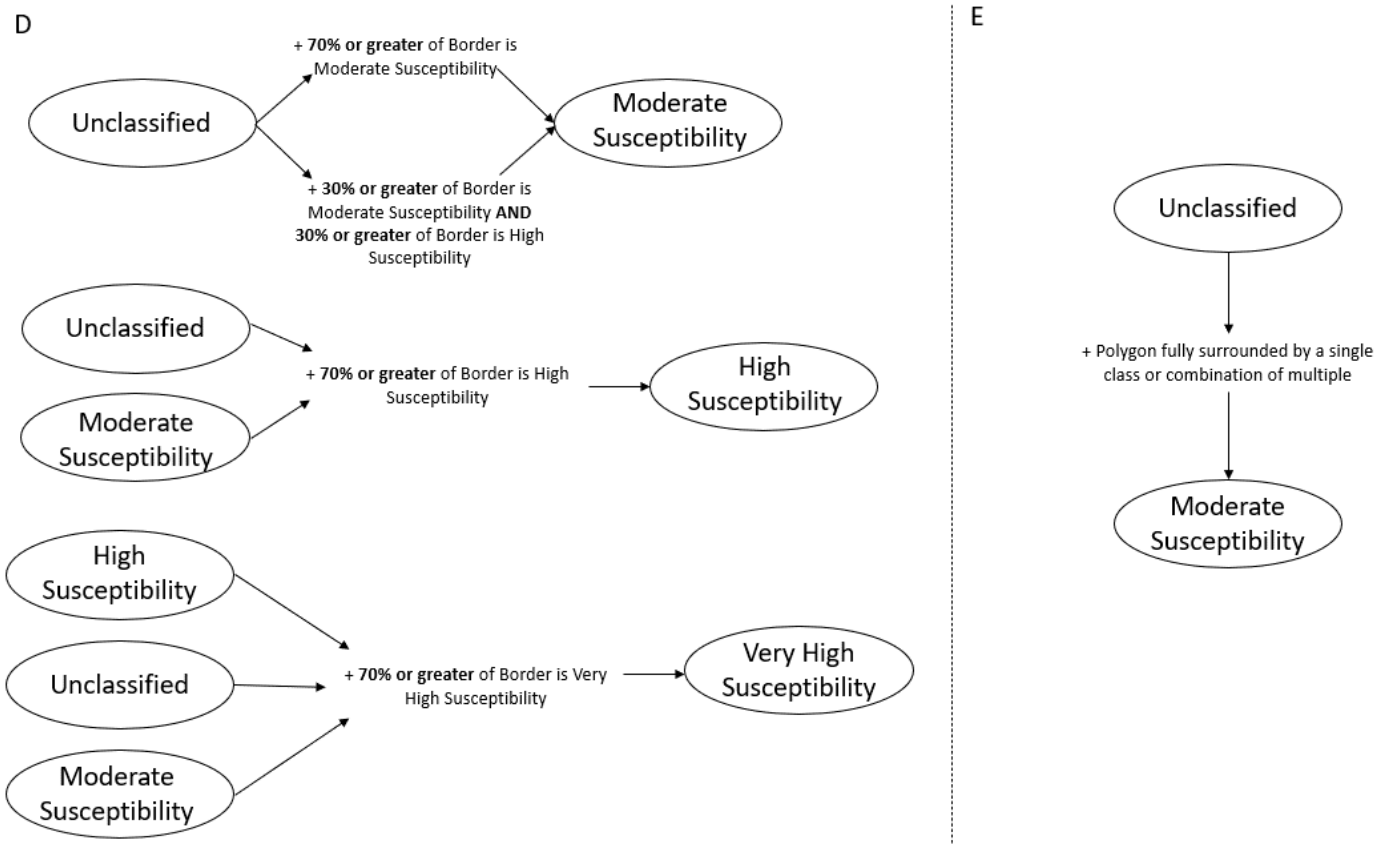

Figure 28. Rockfall ruleset continued. D. Continue to fill holes in the data set based on how much of an objects border is already classified E. fill in any polygons that are fully surrounded by other classified objects

3.2.2.3.3 Deposition Areas Ruleset

The last ruleset we created was for areas with where debris is likely to be deposited. The parameters that we used for this ruleset were slope, vegetation, plan curvature, and flow accumulation. After conducting an in-depth literature review and expert input, the weights or point values we assigned and can be seen in Table 7 . A weight of four was assigned to areas of low slope while the rest of the parameters were weighted with a value of 1.

Table 7. Parameter weights for debris deposition areas

Parameters	Weight/Points
Low Slope (10 °< Slope < 35°)	+4
Not Vegetated (Canopy Height ≤ 10)	+1
Plan Curvature ≤ -0.2	+1
Flow Accumulation ≥ 1000	+1

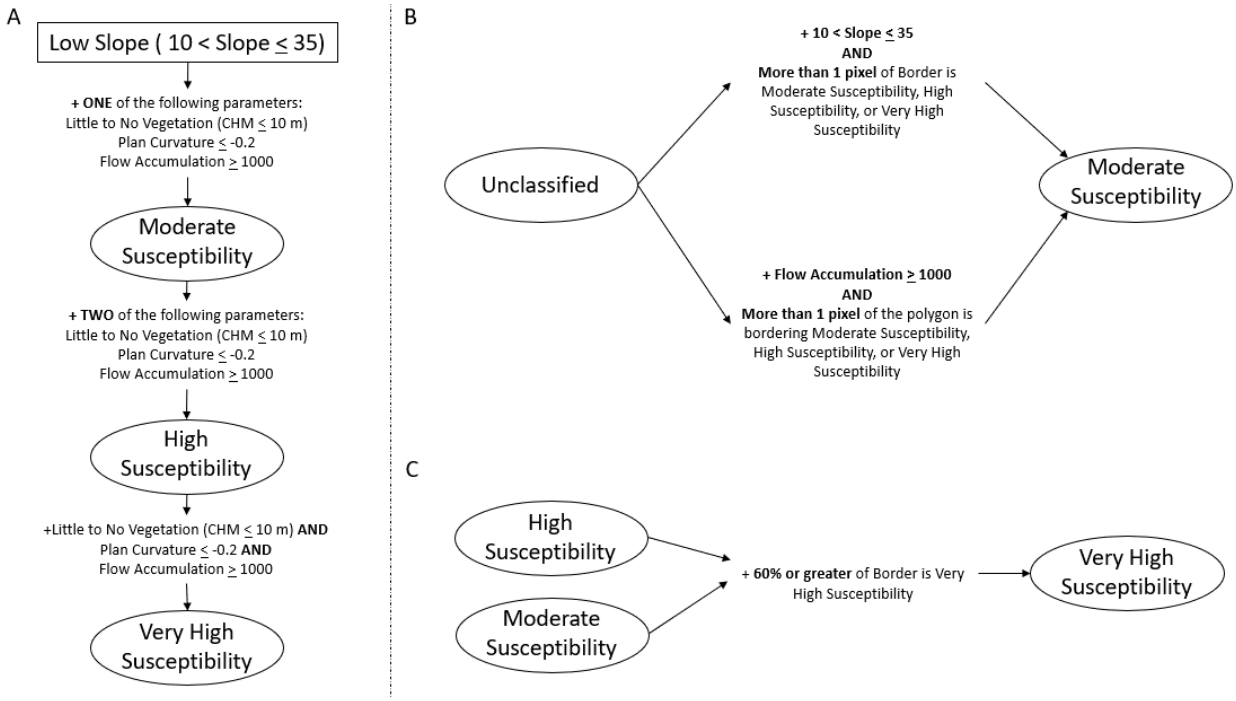

Figure 29. First part of the deposition workflow. A. Classify first based on slope and the presence of the other environmental parameters B. Add in bordering objects with a low slope or high flow accumulation C. Reclassify moderate or high objects into very high susceptibility category if they are mostly surrounded by very high susceptibility

The first part of the ruleset involves isolating slopes that are between 10° and 35° as slope angles were low enough for material to settle on (Figure 29). Then depending on how many of the environmental parameters are met, the susceptibility classification is determined. A low slope with one environmental factor is classified as a moderate deposition susceptibility, while a low slope with two parameters is classified as a high deposition susceptibility, and an object with all three influencing factors is classified as a very high deposition susceptibility.

The next step was to start filling in the holes of the model so an object that borders a classified polygon that has either a low slope or a high flow accumulation is classified as moderate susceptibility (Figure 30). Objects currently classified as moderate or high susceptibility with 60% or more of their border as very high susceptibility was classified as high susceptibility.

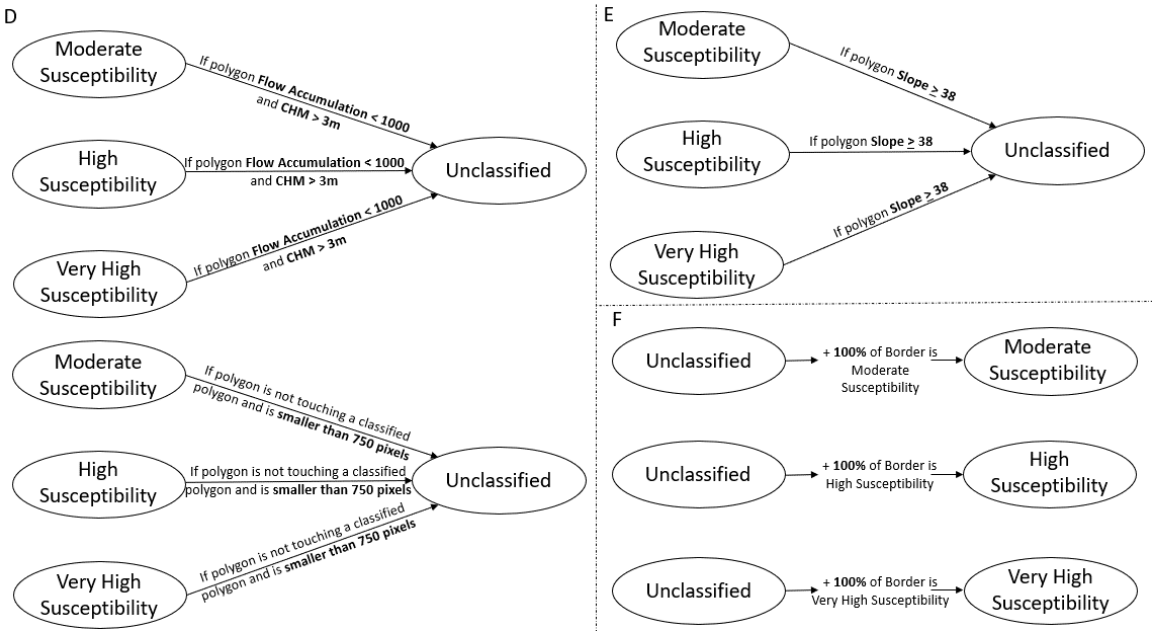

Figure 30. Deposition susceptibility model workflow continued. D. uses flow accumulation and CHM, and object size to remove noise E. Removes steep slopes greater or equal to 38° F. Fill holes in larger classified objects

The ruleset then reduced noise in the model by eliminating polygons with low flow accumulation and high vegetation as well as isolated pixels that are smaller than 750 pixels. Since the previous rules have introduced additional polygons with steeper slopes, the polygons in the same class were merged and any newly merged polygons with an average slope greater than 38° were removed. The last part of the ruleset eliminated any last holes in the model where an

unclassified polygon that is completely surrounded by one other class is then classified as that surrounding class.

3.3 OBIA Results

3.3.1 Landslide Initiation Ruleset Results

The landslide initiation ruleset was applied to each of the three sites, classifying the site into areas of moderate, high and very high landslide initiation susceptibility. These classifications shown in the figures below appear in yellow, orange, and red, respectively.

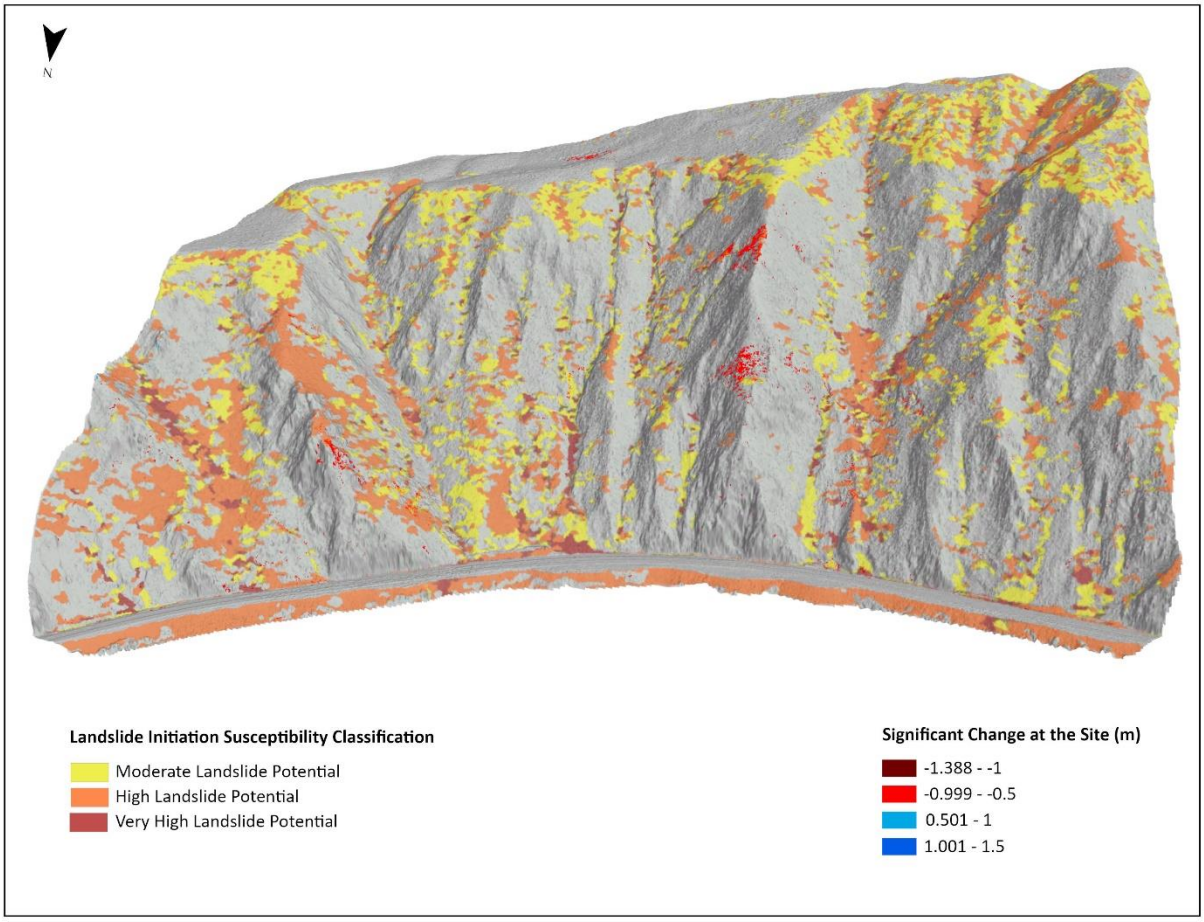

Figure 31. Landslide initiation model for the Kootenai River site

The first site the landslide initiation ruleset was applied to was the Kootenai River site (Figure 31). This model highlighted areas of concern along the ridge top as moderate to high landslide susceptibility. A steep slope on the eastern part of the site was classified as mostly high to very high susceptibility for the entire height of the slope. While those areas did not necessarily correspond with places of significant change, areas along the tracks where significant loss was observed often matched with one of the three classifications. An example of the matching of the significant loss with areas of landslide initiation zones can be seen below, where the area of significant change overlaps with the high landslide initiation susceptibility zone (Figure 32).

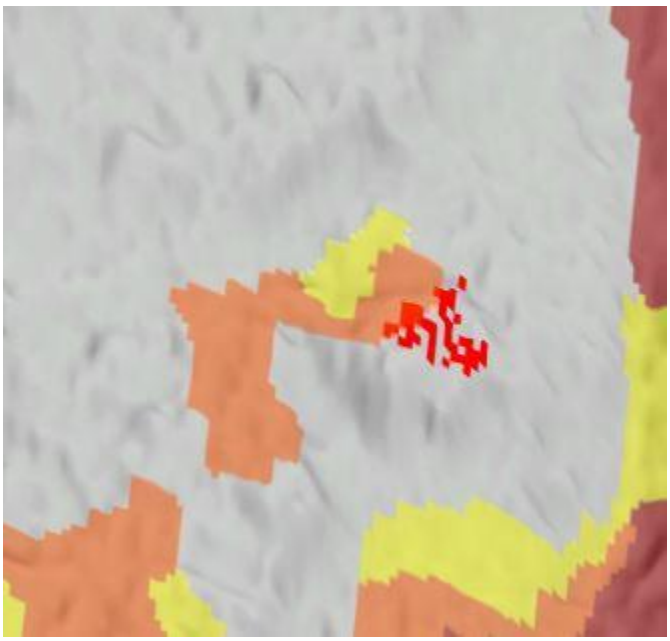

Figure 32. Site of significant loss at the Kootenai River site

The next site that the landslide initiation ruleset was run on was the Deep Creek site (Figure 33). The results of this model emphasized the areas of concern at the site. Highlighting the steep slopes of alluvium and colluvium material below the scarps indicated high landslide initiation

susceptibility. The model even partially overlayed an area classified as high landslide initiation susceptibility with a spot that had undergone significant material loss (Figure 34).

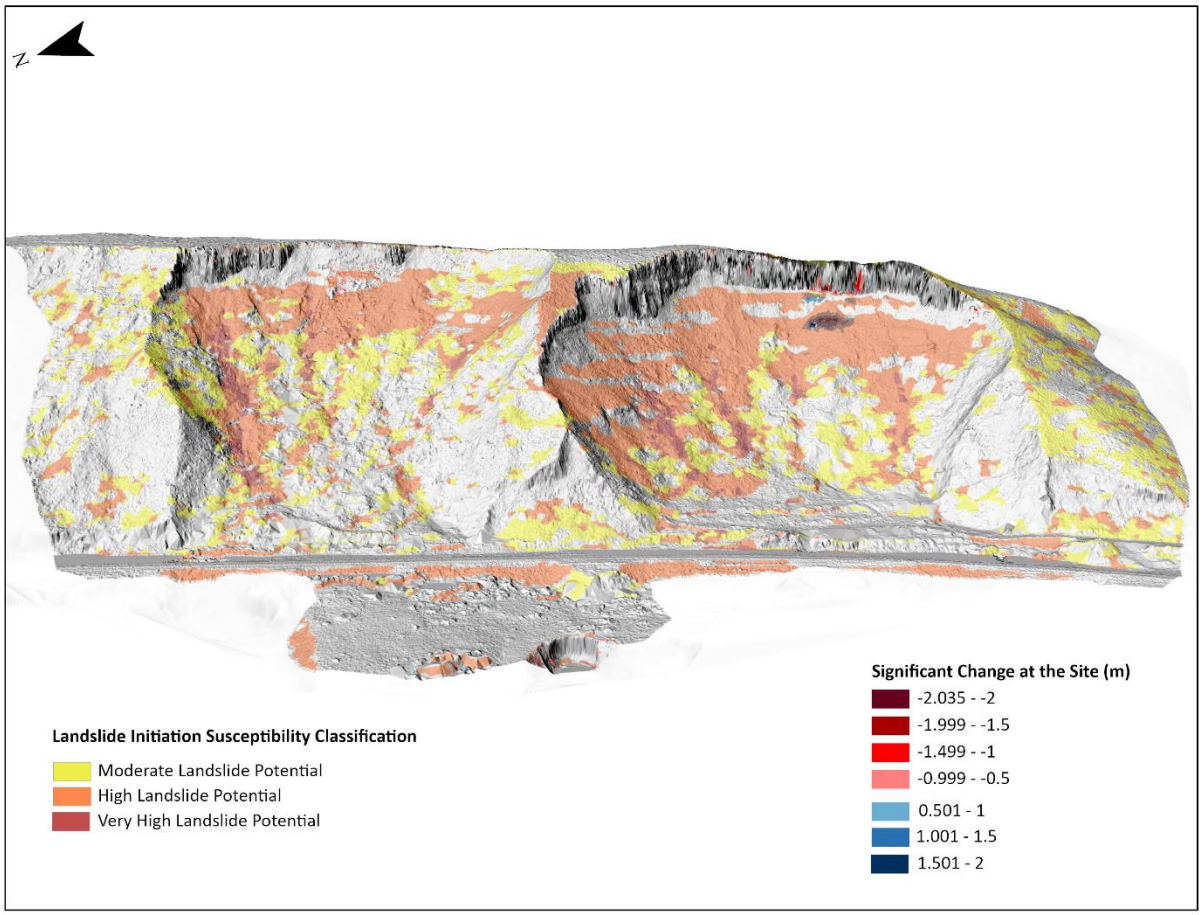

Figure 33. Deep Creek landslide initiation susceptibility model

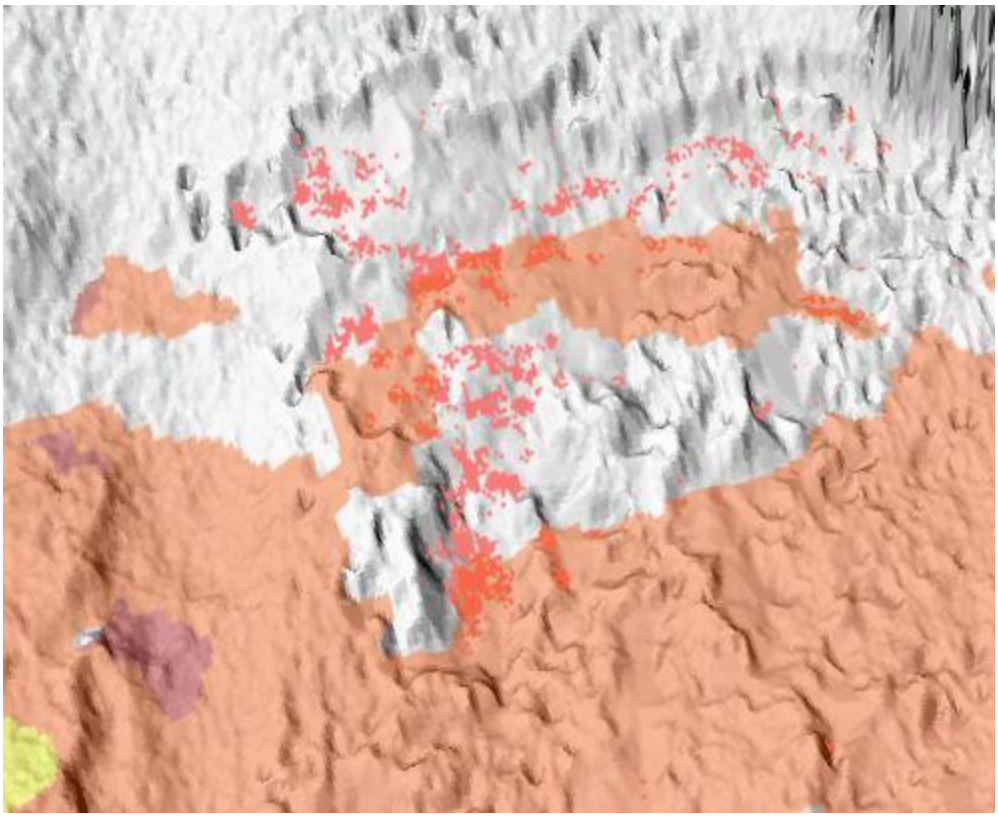

Figure 34. Areas of significant loss that are reflected in the high landslide initiation classification

Lastly, the landslide initiation ruleset was used on the Moyie River site (Figure 35). The output landslide susceptibility model classified much of the bottom half of the site as moderate or high landslide susceptibility. However, the area below the location of the 2017 derailment was classified as very high landslide initiation susceptibility despite most of the significant change at the site being linked to deposition (Figure 36). There were some areas above the railway that were also classified as moderate or high landslide susceptibility, but the majority was on the slope below the tracks.

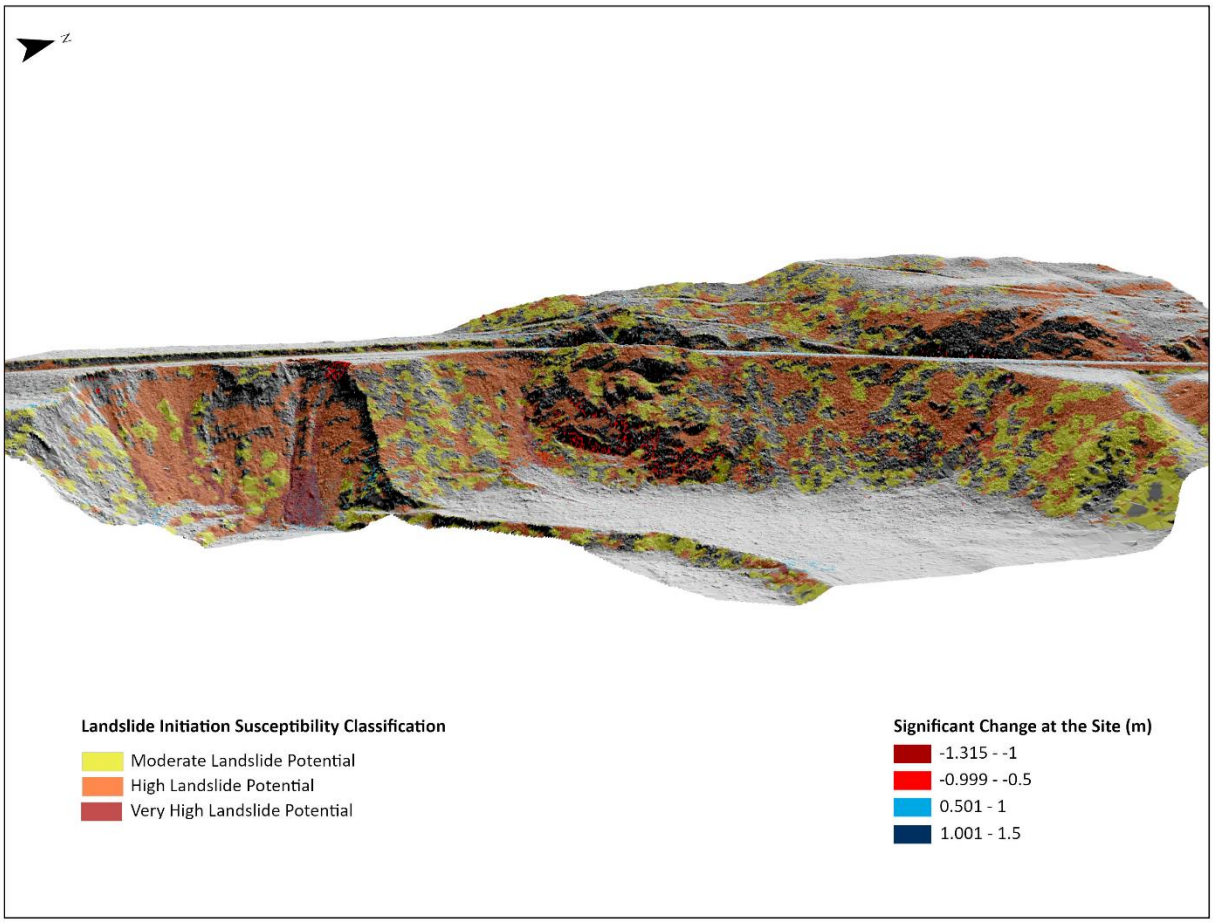

Figure 35. Moyie River landslide initiation model

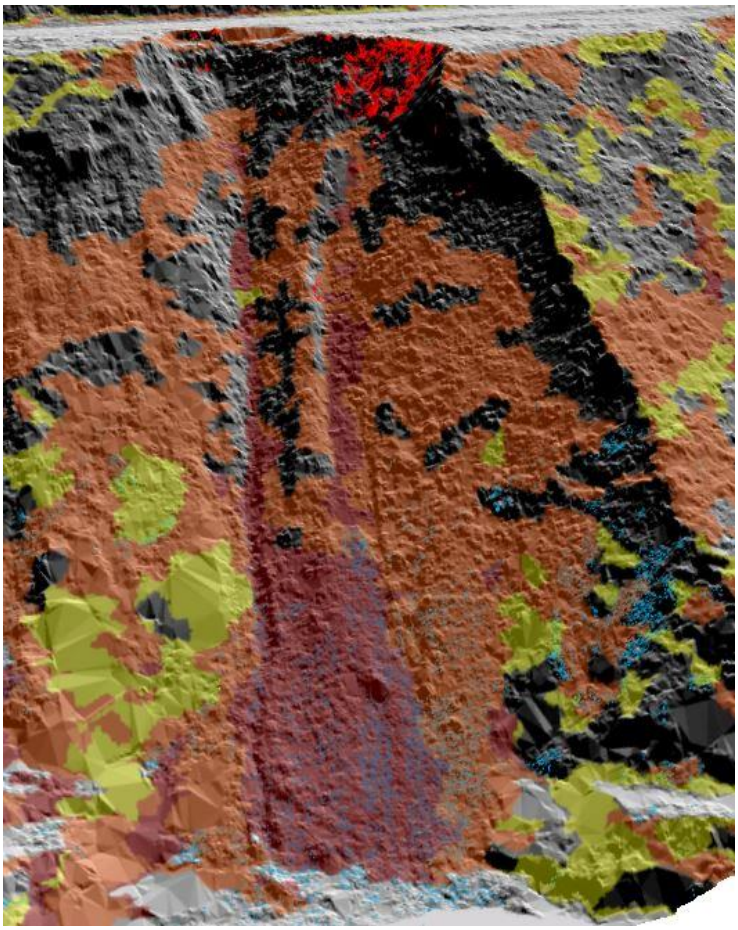

Figure 36. Area classified as having a very high susceptibility for landslide initiation at the Moyie River site.

3.3.2 Rockfall Initiation Ruleset Results

The next susceptibility model that was applied to the three sites was the rockfall initiation model. This model has the same three classifications and corresponding colors outlined in the landslide initiation model. The first model generated was for the Kootenai River site (Figure 37). The model identified the areas of exposed bedrock at the site that matched the areas of significant loss measured by the M3C2 algorithm.

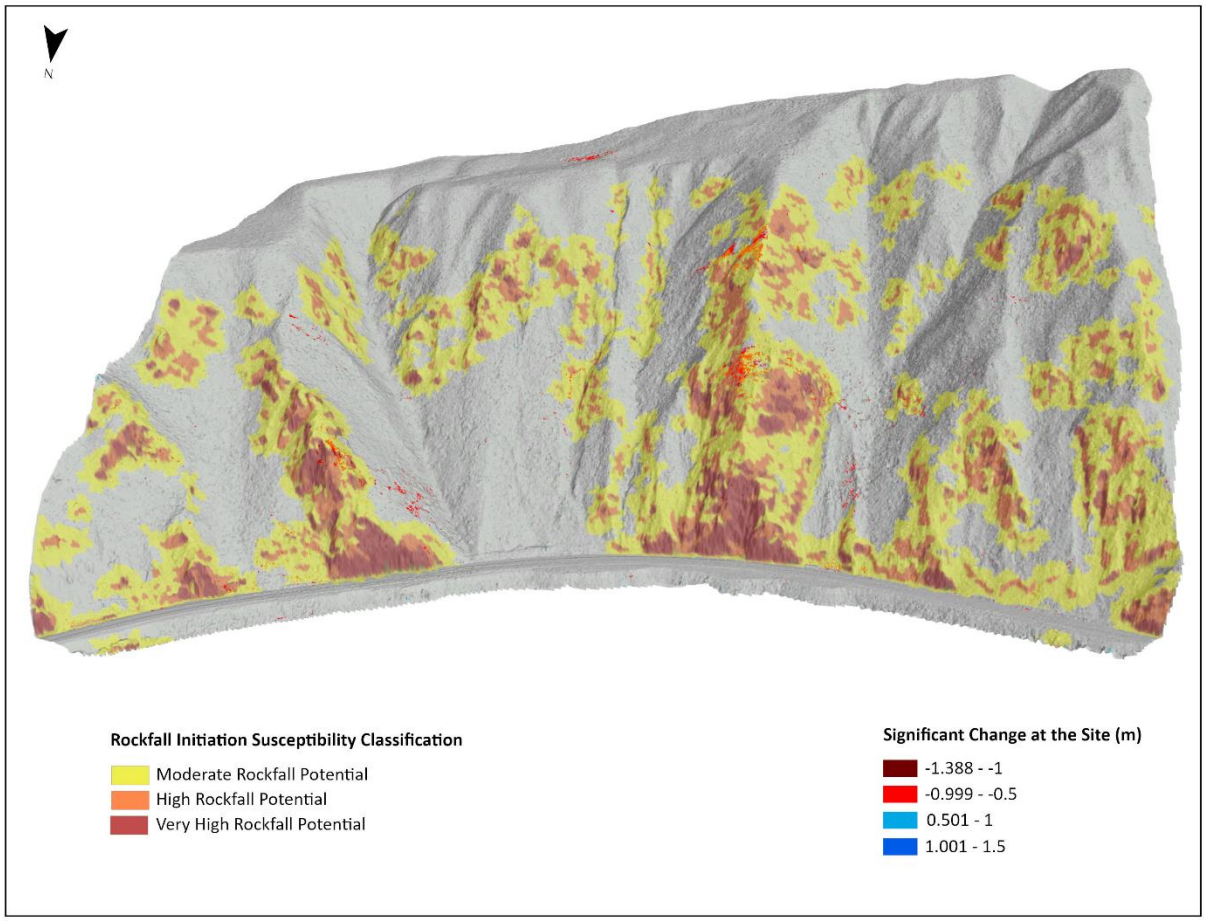

Figure 37. Rockfall initiation susceptibility model for the Kootenai River site

The areas of the highest rockfall susceptibility were located mostly at the shear rock faces along the railroad track and along the rocky ridges running upslope from the railroad. These steep rock faces along the tracks were classified mostly as high or very high rockfall susceptibility and the ridges were classified as a combination of all three classes. These classifications also lined up with the M3C2 results showing significant loss of material in classified areas. One such area is a rockfall section in the central portion of the site along one of

the ridges. This area was mostly classified as either moderate or high rockfall susceptibility in the sections of significant loss (Figure 38).

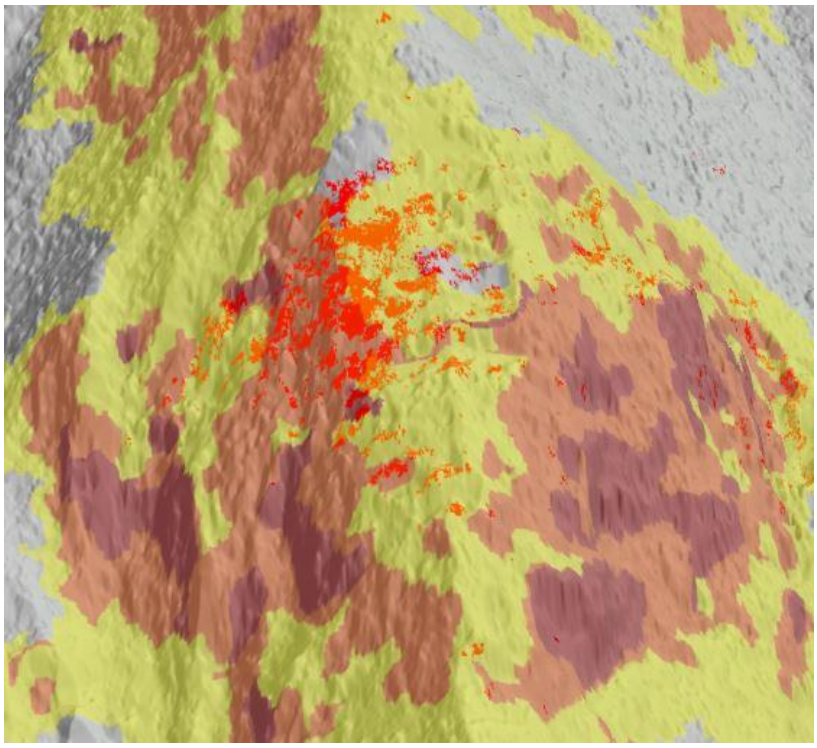

Figure 38. Area of rockfall susceptibility at the Kootenai River site

The Deep Creek site was the next site to have the rockfall susceptibility ruleset applied (Figure 39). The model created showed a majority of the rockfall or in this case earthfall susceptible areas at the site to be isolated along the near vertical scarps at the top of the site. Smaller more isolated areas of earthfall susceptibility were identified closer to the tracks but the

majority were located along the near vertical cliffs.

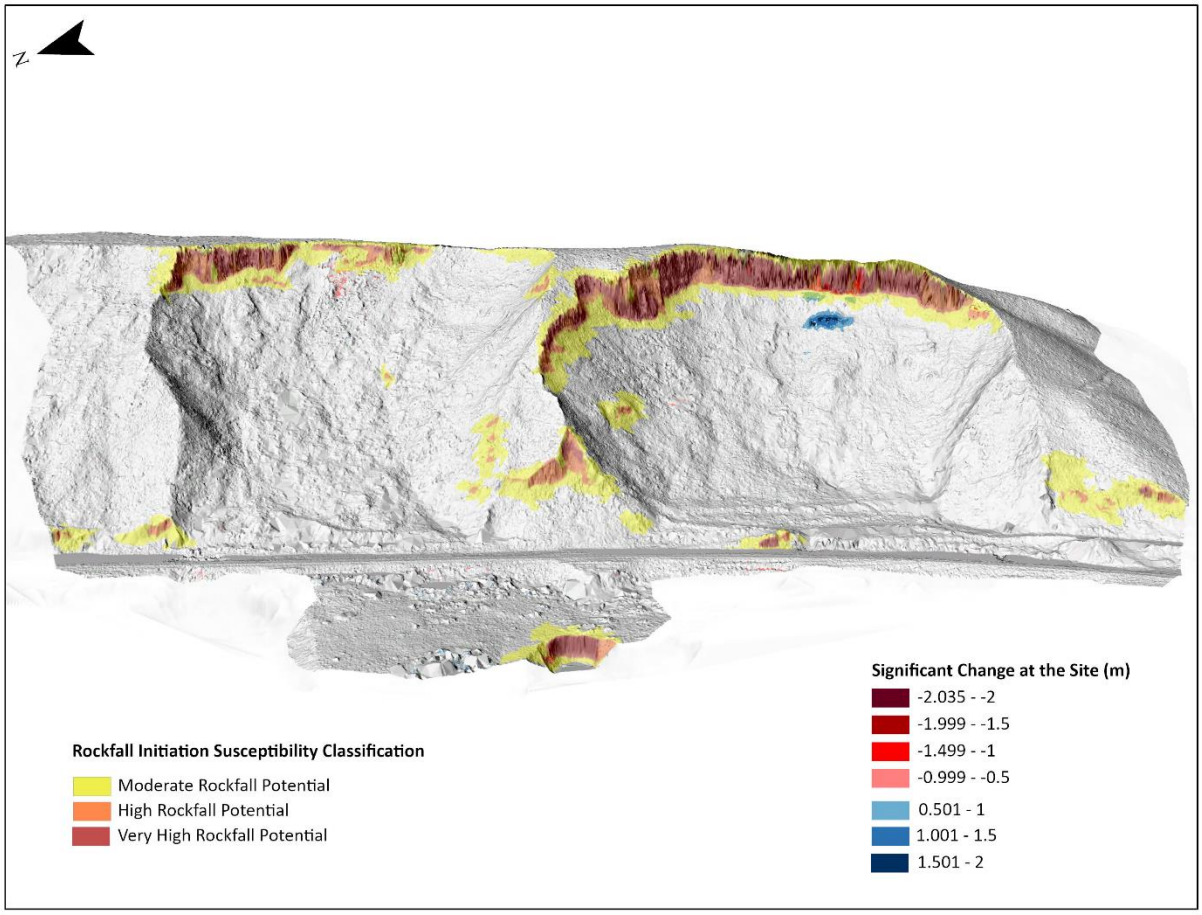

Figure 39. Rockfall initiation model for Deep Creek

The last rockfall model generated was for the Moyie River site (Figure 40). The model was able to classify the limited areas of exposed bed rock mostly located in the northern half to the site above the tracks into rockfall initiation susceptibility classes (Figure 41). However, very steep areas near the site of the 2017 derailment were also classified by the model as rockfall despite rock not being the main material in that section of the site.

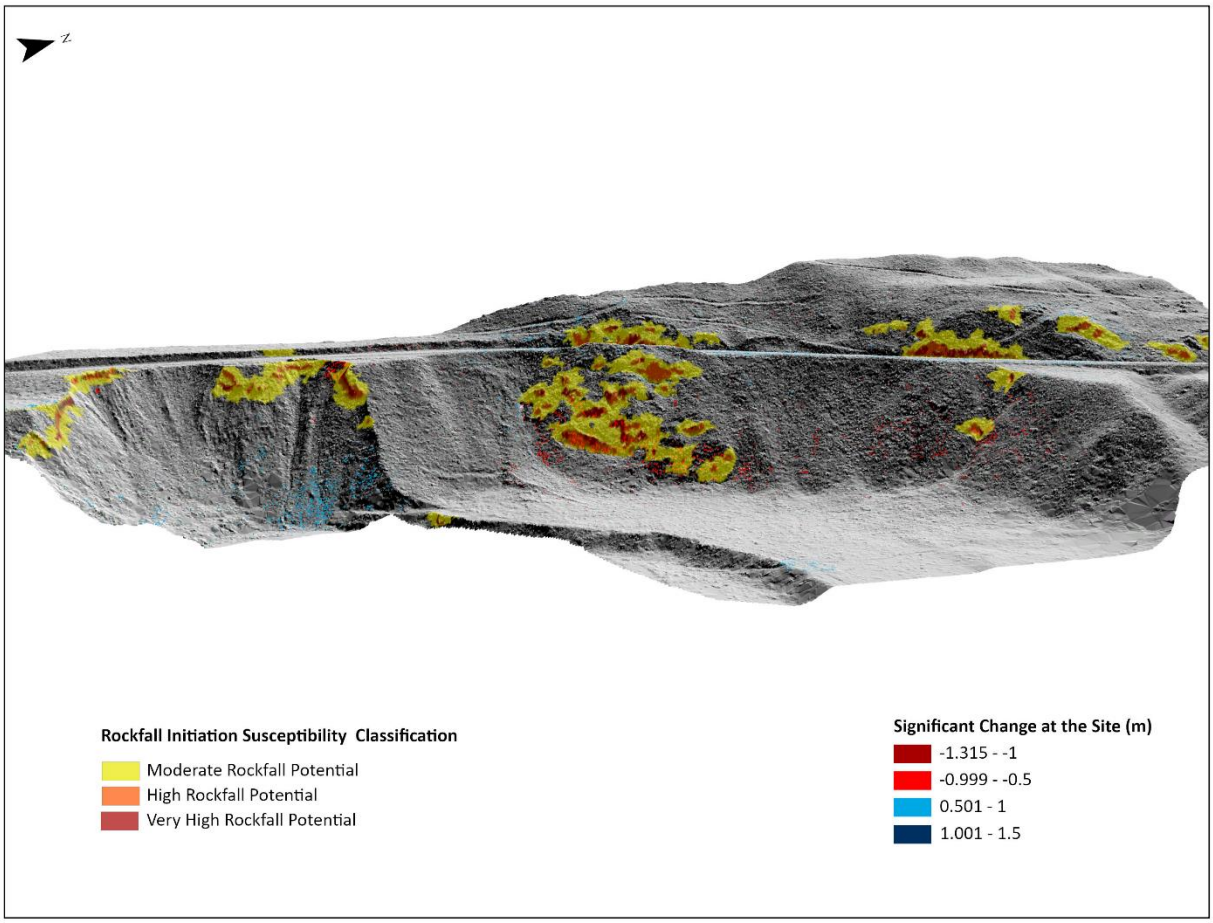

Figure 40. Rockfall initiation model for the Moyie River site

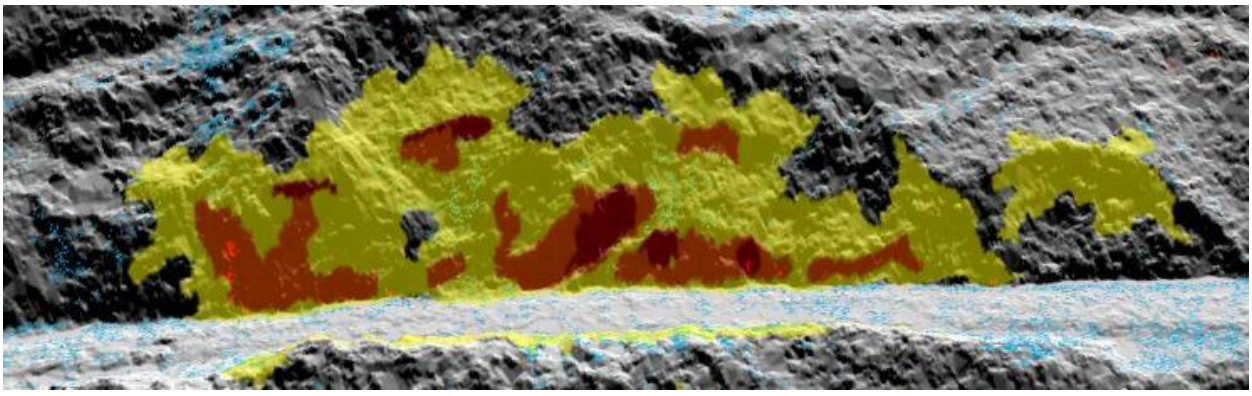

Figure 41. Section of the Moyie River site model classified as an area of rockfall initiation susceptibility

3.3.3 Deposition Ruleset Results

The last set of models created showed areas where debris would likely be deposited. As with the last two models, the deposition ruleset classifies areas into one of three susceptibility categories: moderate deposition susceptibility, high deposition susceptibility, and very high deposition susceptibility.

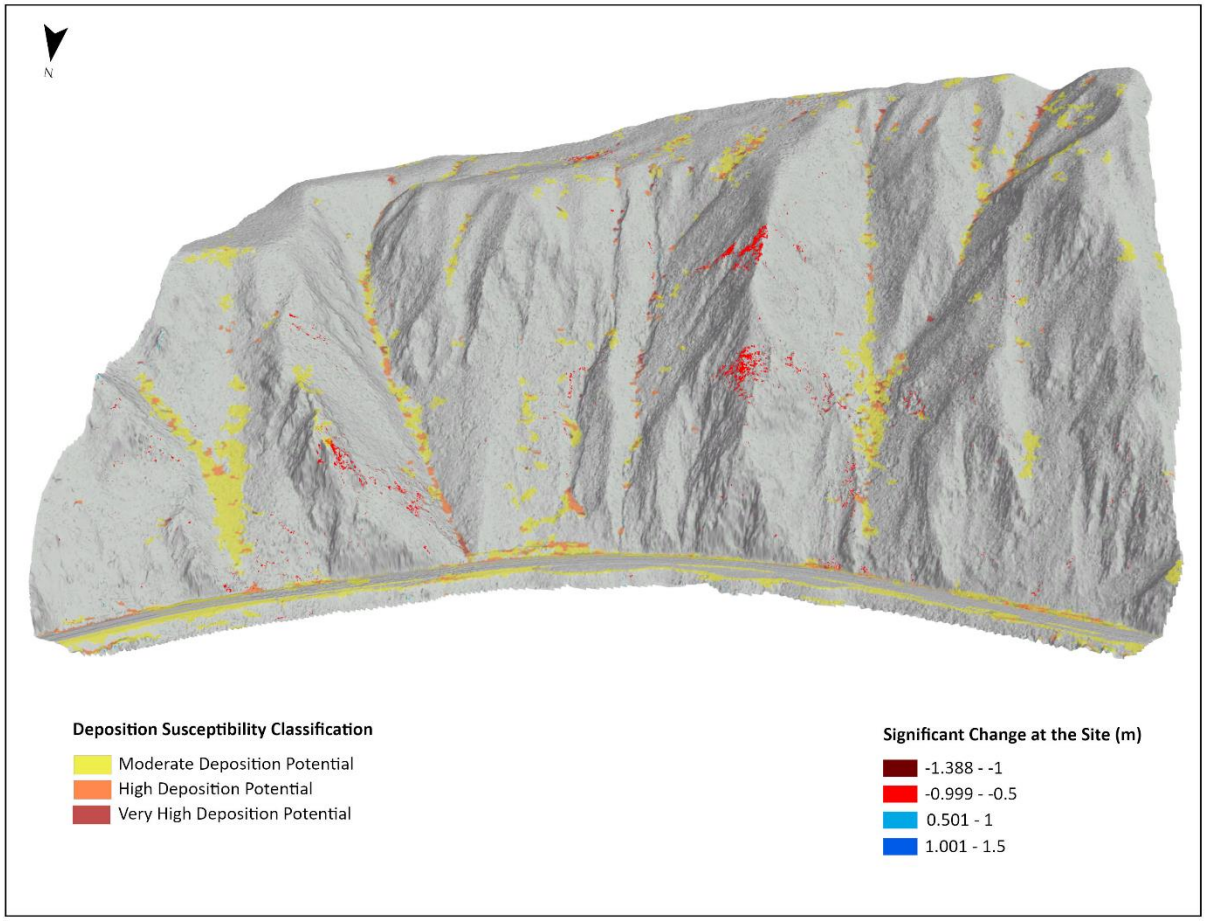

Figure 42. Deposition susceptibility model for the Kootenai River site.

The deposition model for the Kootenai river site shows that the areas of higher deposition susceptibility are mostly the gully areas in between the high ridges of the site. Most of the large gullies at the site are classified as moderate or high deposition susceptibility classification (Figure 42). This matches some of the areas marked as significant deposition from the M3C2

analysis (Figure 43). Another area highlighted by the deposition model are the sections of the slope where the gullies meet the railroad. These sections of the gully separating the railroad from the slope are classified as either moderate or high deposition susceptibility. Very little of the site was classified as very high deposition susceptibility.

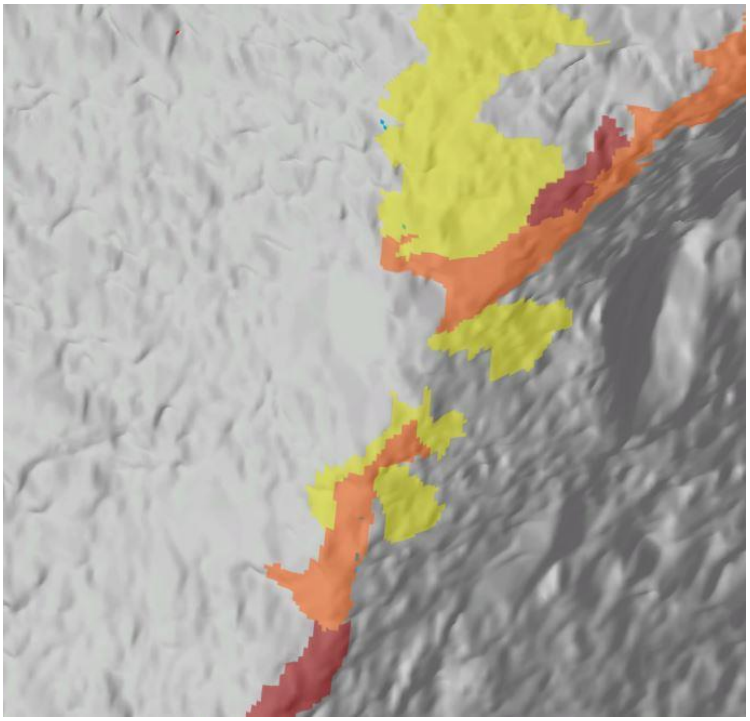

Figure 43. Section of the Kootenai deposition model that shows overlap between the classified polygons (yellow, orange, and red) with the M3C2 areas of significant deposition (blue dots)

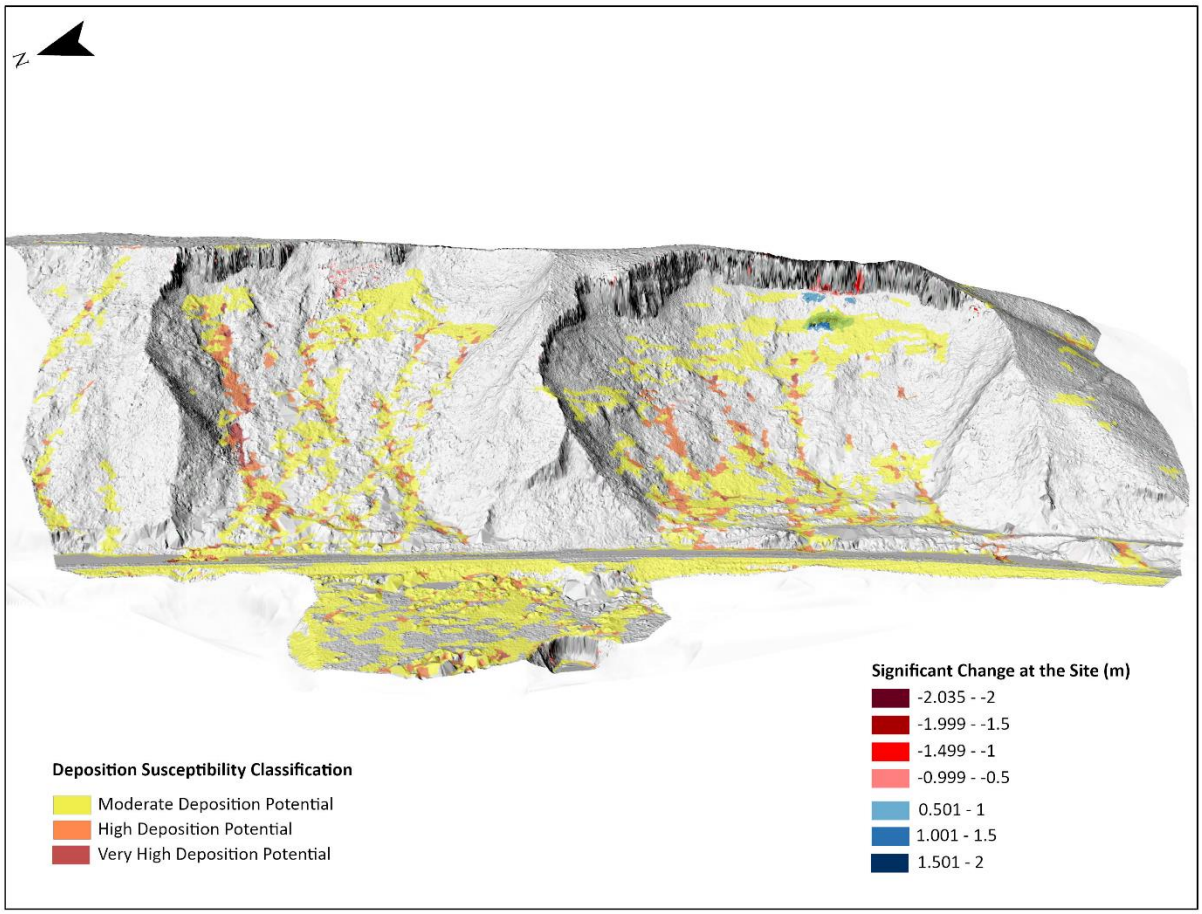

Figure 44. Deep Creek deposition susceptibility model

The deposition model for the Deep Creek site was generated in eCognition (Figure 44). The results of the model line up with the results from the M3C2 algorithm. The areas directly below the steep cliff faces are classified as a moderate deposition susceptibility with the gullies that run perpendicular to the railroad from the cliff face classified as high deposition susceptibility. One area on the north end of the train tracks intersects with one of these larger gullies and that section of the track is classified as a potential deposition area. The moderate deposition susceptibility area at the base of the southern scarp also overlays a large area of significant material deposition, showing the correspondence between the susceptibility model and the M3C2 results.

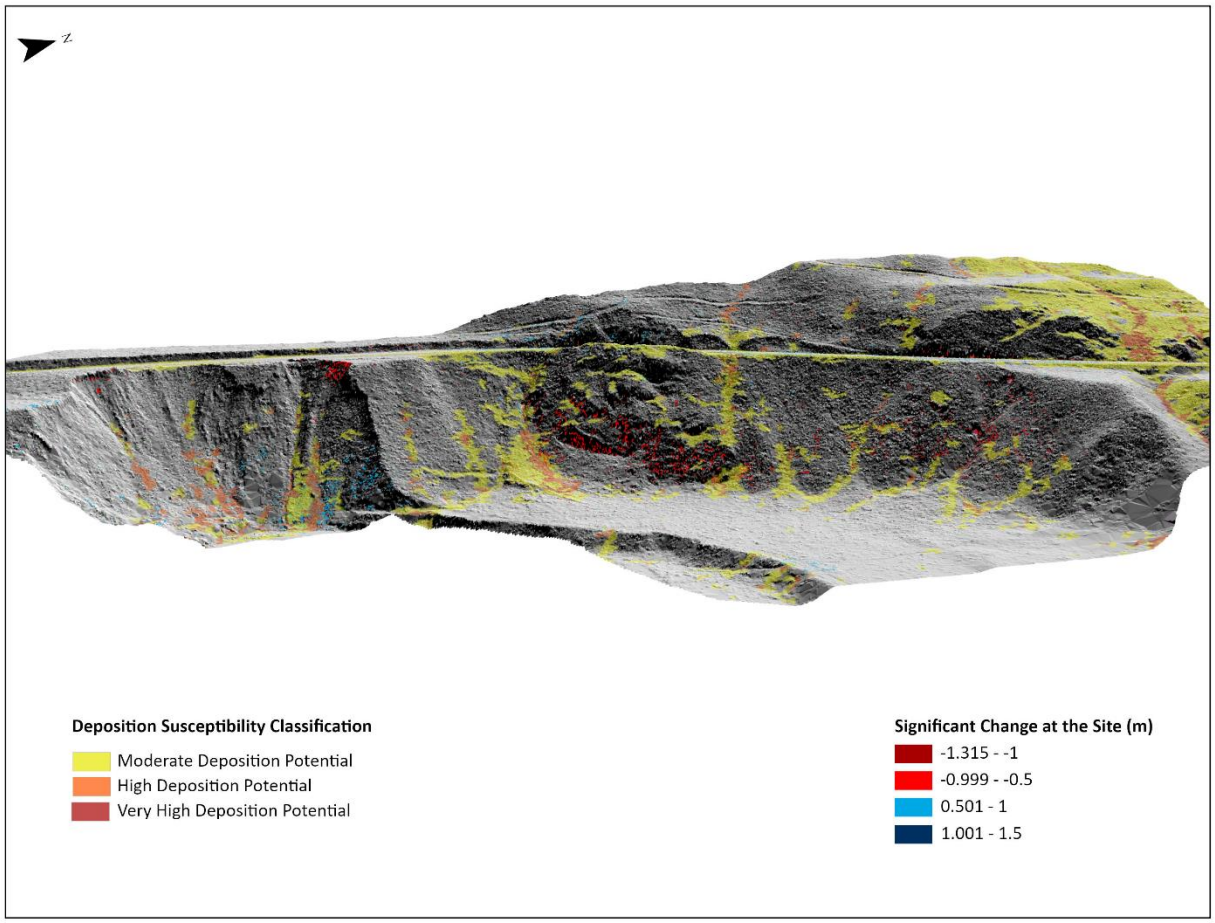

Figure 45. Moyie River site deposition susceptibility model

The last model was the deposition susceptibility model for the Moyie River site (Figure 45). The areas of highest deposition susceptibility are located along the bottom of the slope, along the railroad tracks, and in the northern edge of the site. The area below the 2017 derailment was classified as moderate or high deposition susceptibility matching the significant deposition from the M3C2 results. Another area highlighted by the deposition model is the bare area immediately to the north of the derailment sites where there is a large amount of debris and downed trees. This area is classified as a moderate to high deposition susceptibility. An interesting observation is the unusually large area of moderate susceptibility on the northern edge of the park that is dominated by relatively flat bare ground.

3.4 Ruleset validation

The accuracy of the ruleset was determined by looking at the areas of high slide or fall initiation susceptibility and how they corresponded with areas of documented change in the M3C2 results. Both the OBIA and significant change results were exported as TIFF files and imported into ArcGIS pro for comparison. All rulesets were reviewed by a geohazards expert. A traditional method of susceptibility modeling the relies on the qualitative knowledge of the geohazard expert in identifying areas of high landslide potential (Chung and Fabbri, 2003). A combination of all three models classified ~71.6% of all significant change at the Kootenai River site, ~73.4% of all significant change at the Deep Creek site, and 62.1% of significant change at the Moyie River site into moderate, high, or very high susceptibility. These sites will continue to be monitored over time for change and the collected data will be used to continually improve the models.

3.5 OBIA Discussion

The three susceptibility models generated with OBIA were compared to the M3C2 results for each of the sites. The rockfall initiation susceptibilty model was able to isolate areas of bedrock or areas where falls would be the mechanical process removing material. At the Kootenai River site, areas of significant loss along the rocky ridges of the site were correctly classified in one of the three rockfall susceptibility classes. The model identified areas of significant change and differentiated between rockfall and landslide susceptibility. A section of steep bedrock along the tracks on one side of the ridge was more prone to rockfall while landslides were more likely on the other side (Figure 46). Both the rockfall and landslide models were successful in identifying

the correct corresponding area of the site for each hazard type. In both models for this section, polygons with significant loss were successfully classified into one of the three classes.

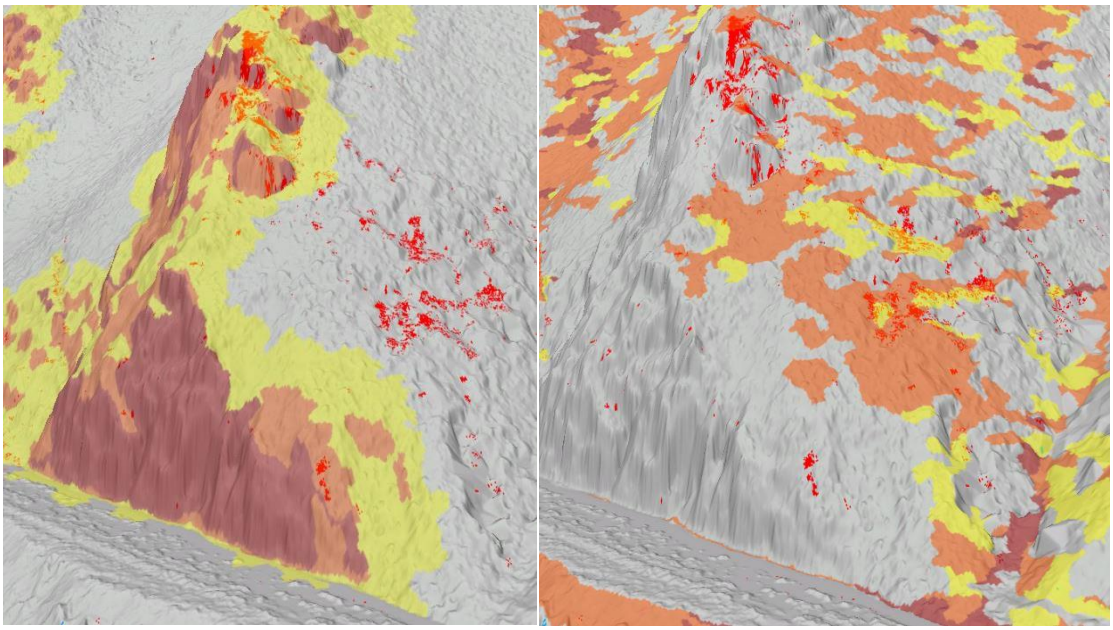

Figure 46. Comparison of rockfall (right) and landslide (left) models at the Kootenai site.

There was also correspondence between the rockfall model and deposition model at the Deep Creek site. From the M3C2 analysis we know that the southern scarp experienced a large amount (~1.5-1.9 m) of significant loss that corresponded with a significant amount of deposition on the slope below (~1-1.5 m). This same relationship is shown in a comparison of the rockfall initiation model and the deposition susceptibility model (Figure 47). The rockfall model clearly covers this area of significant change classifying it in the high and very high rockfall susceptibility classes while the significant deposition below is classified as a moderate deposition susceptibility.

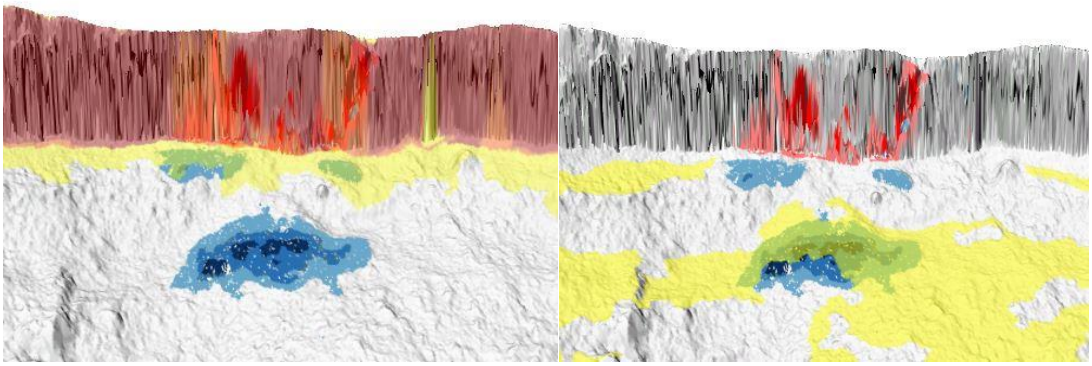

Figure 47. Comparison of the rockfall and deposition models at Deep Creek

The landslide initiation model also corresponded with the deposition model. An example from the Kootenai River site, showed a small area of landslide movement that corresponded with a classified area of deposition below (Figure 48). While the corresponding deposition measured by the M3C2 was not determined to be significant, the loss was, and is thus classified partially as a high landslide initiation susceptibility. The adjacent gully where the deposition likely traveled was classified as high and very high deposition susceptibility classes.

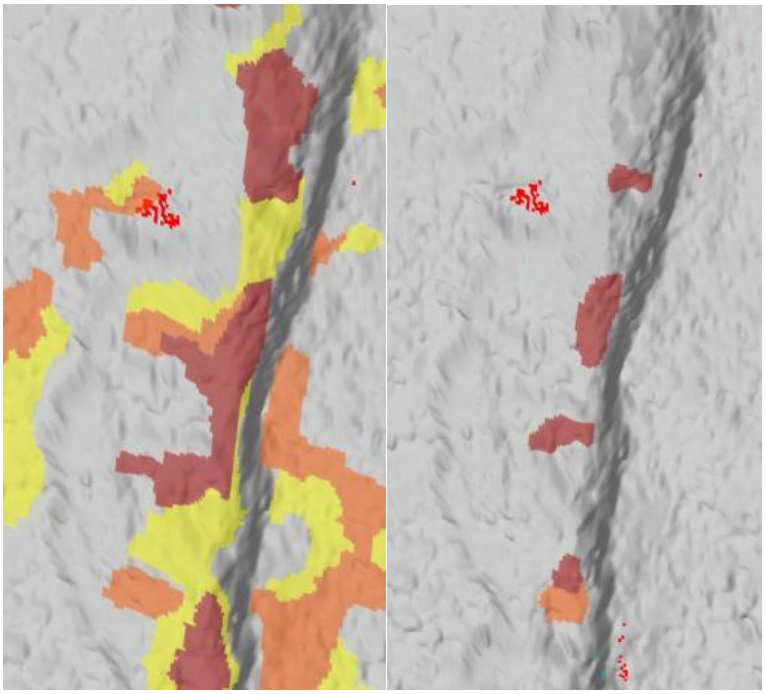

Figure 48. Section of Kootenai River site that shows correspondence between the landslide (left) and deposition (right) models.

Overall, the three models, identified areas of rockfall initiation, landslide initiation, and deposition susceptibility that corresponded with an average of 69% of significant change between the three sites. These classified areas overlapped with areas of significant change, either material loss or gain, at the site. Even areas that we did not expect to be classified in a certain model matched the areas of significant change. For reference, the northern section of Moyie River site was heavily classified as a potential deposition area which overlapped with areas of significant deposition from the M3C2 analysis.

Chapter 4: Conclusion

4.1 Multiscale Model-to-Model Cloud Comparison Conclusion

In the first half of this project, we used a cloud comparison method called the multiscale model-to-model cloud comparison to measure change between point clouds collected in 2017 and 2021. While similar studies have used repeat LiDAR for mass movement monitoring, there are intrinsic issues with this approach in regards to properly aligning two point clouds, changes in georeferencing, and differences in data quality. However, this methodology that we outlined avoids most of the pitfalls inherent to using repeat LiDAR for mass movement monitoring. Using a stripping correction software such as BayeStripAlign2.1 and properly calibrating the LiDAR sensors on the UAV the two point clouds can be initially aligned so close that only a fine registration tool was needed.

The M3C2 plugin from CloudCompare was able to measure the significant change at the three sites. Highlighting areas along the track where material had been removed at the Kootenai River site and a large amount of debris fall and deposition at the Deep Creek site. For most of these areas of significant change the erosion/deposition could also be observed in the RGB imagery of the site. Overall, the M3C2 analysis was able to successfully identify and measure areas of change as small as 40 cm but with the average ranging from 0.5m to 2 m. CloudCompare's 2.5D volume calculation tool was rather limited in its ability to measure volume change at the site. Future work could investigate other tools and software that would allow for a 3D computation of volume change at mass movement sites.

The one major limitation of this project are the holes in the point clouds caused by the sensors failure to penetrate dense vegetation with only two returns. This was the case with the older 2017 flight campaigns which were flown at a higher altitude than the 2021 flights. New

technology such as a LiDAR sensor with more than two returns would better penetrate the dense vegetation improving the coverage and accuracy of the point clouds. Additionally, using a set altitude above ground for further flight campaigns to match that of the previous flight campaigns would be an improvement to future repeat LiDAR studies.

Despite these few limitations, the methodology outlined in this study is an efficient method of identifying significant change at mass movement sites. BayesStripAlign2.1 was shown to be an effective method of resolving the common pitfalls of repeat LiDAR studies by the realigning flight lines. After processing the data with BayesStripAlign2.1 and classifying the point clouds only a simple fine registration was needed avoiding the necessity of ground control points for alignment. The ability to run an alignment without ground control points is necessary when the study sites are extremely remote or as with this case extremely hazardous. With this methodology the railroad companies can fly a site with a UAV, repeatedly over the course of a few years from a safe position and monitor for any change.

4.2 Object Based Image Analysis Conclusion

There are various environmental factors to consider when modeling mass movement susceptibility, including parameters such as slope, aspect, plan curvature, profile curvature, vegetation, and flow accumulation. The second half of this project involved using the gathered point clouds to generate susceptibility models with OBIA. OBIA fuses together these data layers of different environmental parameters that influence mass movement susceptibility or deposition, before segmenting them into objects and classifying those objects. This method creates a more accurate model for susceptibility assessment than traditional pixel-based methods like the weighted overlay model. With this method in Trimble eCognition we created three expert

validated models, one for landslide initiation zones, one for rockfall initiation zones, and one for material deposition zones.

These models were based on expert opinion and compared to the M3C2 results from the previous section. The results of the models are promising, sections of the classifications matched up with some of the significant change at the sites. The initiation susceptibility models also corresponded with the deposition models. The Deep Creek site was a prime example of the significant loss at the top of the scarp getting correctly classified as high to very high rockfall susceptibility while the deposition immediately below classified as a moderate deposition susceptibility. The two initiation zone models were also able to distinguish between landslide and rockfall along the steep ridges at the Kootenai site.

This expert-based model is an efficient method of mapping mass movement susceptibility at multiple sites. Once the ruleset is written and refined with expert knowledge it can be easily and quickly applied to numerous other sites. Creating these standard rulesets for landslides, rockfalls, and deposition is a useful method for railroad companies to identify and prioritize areas of higher mass movement susceptibility. With the models as a better method of prioritizing mass movement susceptibility, the results can be used to guide monitoring and mitigation measures to prevent future derailments.

The sites in this study were chosen based on their predisposition to mass movements with the presence of unconsolidated surficial deposits, the incision of nearby rivers forming steep slopes, and railroad construction. While only three sites were used for this project, further studies could refine the model by running the ruleset on additional sites. The sites we chose had also already undergone large mass movements, continually monitoring these sites for change would be a method to quantitatively test the susceptibility models.

References

Abbaszadeh Shahri, A., Spross, J., Johansson, F., and Larsson, S., 2019, Landslide susceptibility hazard map in southwest Sweden using artificial neural network: Catena, v. 183, p. 104225, doi:10.1016/j.catena.2019.104225.

Abdulwahid, W.M., and Pradhan, B., 2017, Landslide vulnerability and risk assessment for multi-hazard scenarios using airborne laser scanning data (LiDAR): Landslides, v. 14, p. 1057–1076, doi:10.1007/s10346-016-0744-0.

AEVEX Aerospace What is Geo-MMS?, https://geodetics.com/geo-mms-main-page/ (accessed October 2022).

Ahmad, D., Afzal, M., and Rauf, A., 2020, Farmers' adaptation decisions to landslides and flash floods in the mountainous region of Khyber Pakhtunkhwa of Pakistan: Environment, Development and Sustainability, v. 23, p. 8573–8600, doi:10.1007/s10668-020-00983-9.

Akcay, O., Avsar, E.O., Inalpulat, M., Genc, L., and Cam, A., 2018, Assessment of segmentation parameters for object-based land cover classification using color-infrared imagery: ISPRS International Journal of Geo-Information, v. 7, doi:10.3390/ijgi7110424.

Anders, N.S., Seijmonsbergen, A.C., and Bouten, W., 2013, Geomorphological change detection using object-based feature extraction from multi-temporal lidar data: IEEE Geoscience and Remote Sensing Letters, v. 10, p. 1587–1591, doi:10.1109/LGRS.2013.2262317.

Andrew Lassiter, H., Whitley, T., Wilkinson, B., and Abd-elrahman, A., 2020, Scan pattern characterization of velodyne VLP-16 lidar sensor for UAS laser scanning: Sensors (Switzerland), v. 20, p. 1–21, doi:10.3390/s20247351.

Applanix, 2020, POSPac UAV: , p. 2.

Arnous, M.O., and Green, D.R., 2011, GIS and remote sensing as tools for conducting geo-hazards risk assessment along Gulf of Aqaba coastal zone, Egypt: Journal of Coastal Conservation, v. 15, p. 457–475, doi:10.1007/s11852-010-0136-x.

Azarafza, M., Azarafza, M., Akgün, H., Atkinson, P.M., and Derakhshani, R., 2021, Deep learning-based landslide susceptibility mapping: Scientific Reports, v. 11, p. 1–16, doi:10.1038/s41598-021-03585-1.

Barnhart, T.B., Correa, G., and Montero, A.V., 2013, Morphodynamics of the Selawik Retrogressive Thawslump, Northwest Alaska: , p. 1–10.

Barton, G.J., Moran, E.H., and Berenbrock, C., 2004, Surveying Cross Sections of the Kootenai River Between Libby Dam, Montana, and Kootenay Lake, British Columbia Canada: U.S. Geological Survey Open-File Report 2004–1045, p. 35, https://pubs.usgs.gov/of/2004/1045/report.pdf.

BayesMap Solutions LLC, 2020, BayesStripAlign 2.1: , p. 1–83.

BayesMap Solutions LLC, 2022, Strip Alignment:, http://bayesmap.com/products/bayesstripalign/ (accessed April 2022).

Bernard, T.G., Lague, D., and Steer, P., 2021, Beyond 2D landslide inventories and their rollover: Synoptic 3D inventories and volume from repeat lidar data: Earth Surface Dynamics, v. 9, p. 1013–1044, doi:10.5194/esurf-9-1013-2021.

Boundary County, 2005, Boundary County All Hazards Mitigation Plan:, http://2016.boundarycountyid.org/emermgmt/mitigationplan/.

Breckenridge, R.M., Burmester, R.F., Lewis, R.S., McFaddan, M.D., and Lonn, J.D., 2012, Geologic Map of the Curley Creek Quadrangle Boundary County, Idaho and Lincololn

County Montana.:
Burke, M., Jorde, K., and Buffington, J.M., 2009, Application of a hierarchical framework for assessing environmental impacts of dam operation: Changes in streamflow, bed mobility and recruitment of riparian trees in a western North American river: Journal of Environmental Management, v. 90, p. S224–S236, doi:10.1016/j.jenvman.2008.07.022.
Burmester, R.F., Breckenridge, R.M., Mcfaddan, M.D., and Lewis, R.S., 2010a, Geologic Map of the Moyie Springs Quadrangle, Boundary County, Idaho:, https://www.idahogeology.org/pub/Digital_Data/Digital_Web_Maps/moyie_sprgs_DWM-118-m.pdf.
Burmester, R.F., Breckenridge, R.M., McFaddan, M.D., and Lewis, R.S., 2010b, Geologic Map of the Moyie Springs Quadrangle, Boundary County, Idaho.:
Cao, Y., Wei, X., Fan, W., Nan, Y., Xiong, W., and Zhang, S., 2021, Landslide susceptibility assessment using the Weight of Evidence method: A case study in Xunyang area, China: PLoS ONE, v. 16, p. 1–18, doi:10.1371/journal.pone.0245668.
Carey, J.A., Pinter, N., Pickering, A.J., Prentice, C.S., and Delong, S.B., 2019, Analysis of landslide kinematics using multi-temporal unmanned aerial vehicle imagery, La Honda, California: Environmental and Engineering Geoscience, v. 25, p. 301–317, doi:10.2113/EEG-2228.
Carson, M.A., 1977, Angles of repose, angles of shearing resistance and angles of talus slopes: Earth Surface Processes and Landforms, v. 2, p. 363–380, doi:https://doi.org/10.1002/esp.3290020408.
Chung, C.J.F., and Fabbri, A.G., 2003, Validation of spatial prediction models for landslide hazard mapping: Natural Hazards, v. 30, p. 451–472, doi:10.1023/B:NHAZ.0000007172.62651.2b.
CloudCompare, 2015, 2.5D Volume: CloudCompareWiki, https://www.cloudcompare.org/doc/wiki/index.php/2.5D_Volume (accessed November 2022).
CloudCompare, 2016, Align: CloudCompareWiki, https://www.cloudcompare.org/doc/wiki/index.php?title=Align (accessed October 2022).
Columbia Basin Trust, 2021, Kootenay River:, https://thebasin.ourtrust.org/geography/rivers/kootenay-river/#:~:text=In BC%2C Kootenay River is,Purcell and Selkirk mountain ranges. (Accessed February 2021).
Congressional Research Service, 2020, National Landslide Preparedness Act: 116th Congress 2D Session, p. 1–28, https://www.congress.gov/bill/116th-congress/senate-bill/529.
Cucchiaro, S., Maset, E., Cavalli, M., Crema, S., Marchi, L., Beinat, A., and Cazorzi, F., 2020, How does co-registration affect geomorphic change estimates in multi-temporal surveys? GIScience and Remote Sensing, v. 57, p. 611–632, doi:10.1080/15481603.2020.1763048.
DiFrancesco, P.M., Bonneau, D., and Hutchinson, D.J., 2020, The implications of M3C2 projection diameter on 3D semi-automated rockfall extraction from sequential terrestrial laser scanning point clouds: Remote Sensing, v. 12, doi:10.3390/rs12111885.
Doughty, P.T., and Price, R.A., 2000, Geology of the Purcell Trench rift valley and Sandpoint Conglomerate: Eocene en echelon normal faulting and synrift sedimentation along the eastern flank of the Priest River metamorphic complex, northern Idaho: GSA Bulletin, v. 112, p. 1356–1374, doi:10.1130/0016-7606(2000)1122.0.CO;2.
Egholm, D.L., Knudsen, M.F., and Sandiford, M., 2013, Lifespan of mountain ranges scaled by feedbacks between landsliding and erosion by rivers: Nature, v. 498, p. 475–478,

doi:10.1038/nature12218.
Eker, R., Alkan, E., and Aydın, A., 2021, A Comparative Analysis of UAV-RTK and UAV-PPK Methods in Mapping Different Surface Types: European Journal of Forest Engineering, v. 7, p. 12–25, doi:10.33904/ejfe.938067.
Eker, R., Aydın, A., and Hübl, J., 2018, Unmanned aerial vehicle (UAV)-based monitoring of a landslide: Gallenzerkogel landslide (Ybbs-Lower Austria) case study: Environmental Monitoring and Assessment, v. 190, p. 28, doi:10.1007/s10661-017-6402-8.
Ercanoglu, M., and Gokceoglu, C., 2002, Assessment of landslide susceptibility for a landslide-prone area (north of Yenice, NW Turkey) by fuzzy approach: Environmental Geology, v. 41, p. 720–730, doi:10.1007/s00254-001-0454-2.
Esposito, G., Salvini, R., Matano, F., Sacchi, M., Danzi, M., Somma, R., and Troise, C., 2017, Multitemporal monitoring of a coastal landslide through SfM-derived point cloud comparison: Photogrammetric Record, v. 32, p. 459–479, doi:10.1111/phor.12218.
Esri Curvature Function: ArcGIS Desktop, https://desktop.arcgis.com/en/arcmap/latest/manage-data/raster-and-images/curvature-function.html (accessed June 2022a).
Esri Flow Direction (Spatial Analyst):, https://pro.arcgis.com/en/pro-app/latest/tool-reference/spatial-analyst/flow-direction.htm (accessed October 2022b).
Esri How Aspect Works:, https://pro.arcgis.com/en/pro-app/latest/tool-reference/spatial-analyst/how-aspect-works.htm#:~:text=The Aspect tool identifies the,north)%2C coming full circle. (accessed October 2022c).
Esri How Flow Accumulation Works:, https://pro.arcgis.com/en/pro-app/latest/tool-reference/spatial-analyst/how-flow-accumulation-works.htm (accessed October 2022d).
Esri How Hillshade Works:, https://pro.arcgis.com/en/pro-app/latest/tool-reference/3d-analyst/how-hillshade-works.htm (accessed October 2022e).
Fanos, A.M., Pradhan, B., Mansor, S., Yusoff, Z.M., Abdullah, A.F. bin, and Jung, H.-S., 2019, Rockfall source identification using a hybrid Gaussian mixture-ensemble machine learning model and LiDAR data: Korean Journal of Remote Sensing, v. 35, p. 93–115, doi:https://doi.org/10.7780/kjrs.2019.35.1.7.
Francou, B., and Manté, C., 1990, Analysis of the segmentation in the profile of alpine talus slopes: Permafrost and Periglacial Processes, v. 1, p. 53–60, doi:10.1002/ppp.3430010107.
Gariano, S.L., and Guzzetti, F., 2016, Landslides in a changing climate: Earth-Science Reviews, v. 162, p. 227–252, doi:10.1016/j.earscirev.2016.08.011.
Glenn, N.F., Streutker, D.R., Chadwick, D.J., Thackray, G.D., and Dorsch, S.J., 2006, Analysis of LiDAR-derived topographic information for characterizing and differentiating landslide morphology and activity: Geomorphology, v. 73, p. 131–148, doi:10.1016/j.geomorph.2005.07.006.
Golly, A., Turowski, J.M., Badoux, A., and Hovius, N., 2017, Controls and feedbacks in the coupling of mountain channels and hillslopes: Geology, v. 45, p. 307–310, doi:10.1130/G38831.1.
Gorsevski, P. V., Brown, M.K., Panter, K., Onasch, C.M., Simic, A., and Snyder, J., 2016, Landslide detection and susceptibility mapping using LiDAR and an artificial neural network approach: a case study in the Cuyahoga Valley National Park, Ohio: Landslides, v. 13, p. 467–484, doi:10.1007/s10346-015-0587-0.
Hanrahan, M., 2020, Derailed train plunges into river in Idaho, crew rescued by boat: abc News, https://abcnews.go.com/US/derailed-train-plunges-river-idaho-crew-rescued-boat/story?id=68045919#:~:text=The derailment was reportedly caused by a rock

slide.&text=The Burlington Northern Railroad train,crew may be trapped inside (Accessed November 2020).
Happ, P.N., Ferreira, R.S., Bentes, C., Costa, G.A.O.P., and Feitosa, R.Q., 2010, Multiresolution segmentation: a parallel approach for high resolution image segmentation in multicore architectures: The International Archives of the Photogrammetry, Remote Sensing and Spatial Information Sciences, v. 38, p. C7, https://www.researchgate.net/publication/267784147.
Highland, L.M., and Bobrowsky, P., 2008, The Landslide Handbook — A Guide to Understanding Landslides: Reston, Virginia, U.S. Geological Survey Circular 1325, p. 129.
Hossain, M.D., and Chen, D., 2019, Segmentation for Object-Based Image Analysis (OBIA): A review of algorithms and challenges from remote sensing perspective: ISPRS Journal of Photogrammetry and Remote Sensing, v. 150, p. 115–134, doi:10.1016/j.isprsjprs.2019.02.009.
Hung, C.L.J., Tseng, C.W., Huang, M.J., Tseng, C.M., and Chang, K.J., 2019, Multi-temporal high-resolution landslide monitoring based on uas photogrammetry and uas lidar geoinformation: International Archives of the Photogrammetry, Remote Sensing and Spatial Information Sciences - ISPRS Archives, v. 42, p. 157–160, doi:10.5194/isprs-archives-XLII-3-W8-157-2019.
Hussin, H.Y., Quan Luna, B., Van Westen, C.J., Christen, M., Malet, J.P., and Van Asch, T.W.J., 2012, Parameterization of a numerical 2-D debris flow model with entrainment: A case study of the Faucon catchment, Southern French Alps: Natural Hazards and Earth System Science, v. 12, p. 3075–3090, doi:10.5194/nhess-12-3075-2012.
Hyper-Tech Systems, 2017, Velodyne LiDAR Puck:, www.velodynelidar.com.
Idaho Geological Survey, 2020, Annual Report Fiscal Year 2020:, https://www.idahogeology.org/pub/Annual_Reports/IGS_Annual_Report_FY2020.pdf.
Idaho Office of Emergency Management Chapter 3.7 Risk Assessment: Landslide:, https://ioem.idaho.gov/wp-content/uploads/sites/57/2018/12/ID-SHMP-Chapter-3.7-Landslide.pdf (accessed February 2022).
Idaho Office of Emergency Management, 2018, Chapter 3.7 Risk Assessment: Landslide:, https://ioem.idaho.gov/wp-content/uploads/sites/57/2018/12/ID-SHMP-Chapter-3.7-Landslide.pdf (accessed February 2022).
IPCC, 2012, Managing the Risks of Extreme Events and Disasters to Advance Climate Change Adaptation:, doi:10.1017/CBO9781139177245.009.
Jaboyedoff, M., and Labiouse, V., 2011, Technical note: Preliminary estimation of rockfall runout zones: Natural Hazards and Earth System Science, v. 11, p. 819–828, doi:10.5194/nhess-11-819-2011.
Jacobs, J.M., Hunsaker, A.G., Sullivan, F.B., Palace, M., Burakowski, E.A., Herrick, C., and Cho, E., 2021, Snow depth mapping with unpiloted aerial system lidar observations: A case study in Durham, New Hampshire, United States: Cryosphere, v. 15, p. 1485–1500, doi:10.5194/tc-15-1485-2021.
Jakob, M., 2022, Chapter 14 - Landslides in a changing climate, *in* Davies, T., Rosser, N., and Shroder, J.F. eds., Landslide Hazards, Risks, and Disasters, Elsevier Inc., p. 505–579, doi:10.1016/b978-0-12-818464-6.00003-2.
Karantanellis, E., Marinos, V., Vassilakis, E., and Christaras, B., 2020, Object-based analysis using unmanned aerial vehicles (UAVs) for site-specific landslide assessment: Remote Sensing, v. 12, doi:10.3390/rs12111711.

Karantanellis, E., Marinos, V., Vassilakis, E., and Hölbling, D., 2021, Evaluation of machine learning algorithms for object-based mapping of landslide zones using UAV data: Geosciences (Switzerland), v. 11, p. 1–19, doi:10.3390/geosciences11080305.

Kim, H.G., Lee, D.K., and Park, C., 2018, Assessing the cost of damage and effect of adaptation to landslides considering climate change: Sustainability (Switzerland), v. 10, doi:10.3390/su10051628.

Kopp, S., 2021, New Surface Analysis Capabilities in ArcGIS Pro 2.7: ArcGIS Blog, https://www.esri.com/arcgis-blog/products/arcgis-pro/analytics/new-slope-aspect-curvature/ (accessed May 2022).

Lague, D., Brodu, N., and Leroux, J., 2013, Accurate 3D comparison of complex topography with terrestrial laser scanner: Application to the Rangitikei canyon (N-Z): ISPRS Journal of Photogrammetry and Remote Sensing, v. 82, p. 10–26, doi:10.1016/j.isprsjprs.2013.04.009.

Larsen, I.J., and Montgomery, D.R., 2012, Landslide erosion coupled to tectonics and river incision: Nature Geoscience, v. 5, p. 468–473, doi:10.1038/ngeo1479.

Lifton, Z.M., Ducar, S.D., Tate, C.A., and Idaho Geological Survey, 2020, Landslide Inventory Database for Idaho:, https://idahogeology.org/pub/Digital_Data/Digital_Databases/DD-10_report.pdf.

Link, P.K., 2002, Boundary County, Idaho: Digital Atlas of Idaho, https://digitalatlas.cose.isu.edu/counties/boundary/geomap.htm.

Mahalingam, R., Olsen, M.J., and O'Banion, M.S., 2016, Evaluation of landslide susceptibility mapping techniques using lidar-derived conditioning factors (Oregon case study): Geomatics, Natural Hazards and Risk, v. 7, p. 1884–1907, doi:10.1080/19475705.2016.1172520.

McClelland, D.E., Foltz, R.B., Falter, C.M., Wilson, W.D., Cundy, T., Schuster, R.L., Saurbier, J., Rabe, C., and Heinemann, R., 1999, Relative effects on a low-volume road system of landslides resulting from episodic storms in northern Idaho: Transportation Research Record, v. 2, p. 235–243, doi:10.3141/1652-63.

Mcfaddan, M.D., Breckenridge, R.M., Burmester, R.F., and Lewis, R.S., 2009, Geologic Map of the Naples Quadrangle, Boundary and Bonner Counties, Idaho:, https://www.idahogeology.org/pub/Digital_Data/Digital_Web_Maps/Naples_DWM-109-m.pdf.

Murray, J.R., and Svarc, J., 2017, Global Positioning System data collection, processing, and analysis conducted by the U.S. Geological Survey Earthquake Hazards Program: Seismological Research Letters, v. 88, p. 916–925, doi:https://doi.org/10.1785/0220160204.

Oktorie, O., 2017, A Study of Landslide Areas Mitigation and Adaptation in Palupuah Subdistrict, Agam Regency, West Sumatra Province, Indonesia: Sumatra Journal of Disaster, Geography and Geography Education, v. 1, p. 43–49, doi:10.24036/sjdgge.v1i1.34.

Omran, A., Fahmida, K., Schröder, D., Arnous, M.O., El-Rayes, A.E., and Hochschild, V., 2021, GIS-based rockfall hazard zones modeling along the coastal Gulf of Aqaba Region, Egypt: Earth Science Informatics, v. 14, p. 691–709, doi:10.1007/s12145-021-00580-y.

Ouimet, W.B., Whipple, K.X., Royden, L.H., Sun, Z., and Chen, Z., 2007, The influence of large landslides on river incision in a transient landscape: Eastern margin of the Tibetan Plateau (Sichuan, China): Bulletin of the Geological Society of America, v. 119, p. 1462–1476, doi:10.1130/B26136.1.

Peters, J.L., 2012, Late Pleistocene evolution of glacial Lake Purcell: a potential floodwater

source to the Channeled Scabland: Simon Fraser University, Vancouver, Canada, 288 p.
Peters, J.L., and Brennand, T.A., 2020, Palaeogeographical reconstruction and hydrology of glacial Lake Purcell during MIS 2 and its potential impact on the Channeled Scabland, USA: Boreas, v. 49, p. 461–476, doi:10.1111/bor.12434.
Polzin, M.L., and Rood, S.B., 2000, Effects of Damming and Flow Stabilization on Riparian Processes and Black Cottonwoods along the Kootenay River: Rivers, v. 7, p. 221–232.
Raghuvanshi, T.K., Negassa, L., and Kala, P.M., 2015, GIS based Grid overlay method versus modeling approach - A comparative study for landslide hazard zonation (LHZ) in Meta Robi District of West Showa Zone in Ethiopia: Egyptian Journal of Remote Sensing and Space Science, v. 18, p. 235–250, doi:10.1016/j.ejrs.2015.08.001.
rapidlasso lasindex.:
rapidlasso, 2012, LASindex -spatial indexing of LiDAR data: rapidlasso GmbH, https://rapidlasso.com/2012/12/03/lasindex-spatial-indexing-of-lidar-data/ (accessed October 2022).
Sarkar, S., and Kanungo, D.P., 2004, An integrated approach for landslide susceptibility mapping using remote sensing and GIS: Photogrammetric Engineering and Remote Sensing, v. 70, p. 617–625, doi:10.14358/PERS.70.5.617.
Saroglou, C., 2019, GIS-based rockfall susceptibility zoning in Greece: Geosciences (Switzerland), v. 9, doi:10.3390/geosciences9040163.
Sokol, C., 2017, Mudslide causes train to derail in Boundary County: The Spokesman-Review, https://www.spokesman.com/stories/2017/mar/15/mudslide-causes-train-to-derail-in-boundary-county/ (Accessed November 2020).
Trimble, 2019, APX-15 UAV:, https://www.applanix.com/downloads/products/specs/APX15_UAV.pdf.
Trimble Inc., 2019, Basic Rule Set Editing:, https://docs.ecognition.com/v9.5.0/eCognition_documentation/User Guide Developer/4 Basic Rule Set Editing.htm.
U.S. Climate Data, 2022, Weather History Bonners Ferry:, https://www.usclimatedata.com/climate/bonners-ferry/idaho/united-states/usid0026 (accessed October 2022).
United States Congress, 2020, Public Law 116 - 323 - National Landslide Preparedness Act: Congressional Record, Vol. 166, https://www.govinfo.gov/app/details/PLAW-116publ323.
United States Department of Agriculture Forest Service, and Boise National Forest, 1995, Final Environmental Impact Statement Thunderbolt Wildfire Recovery:, https://books.google.com/books?id=Gaw2AQAAMAAJ&pg=RA1-PA39&lpg=RA1-PA39&dq=Slope+%22aspect%22+prone+to+rockfall+%22Idaho%22&source=bl&ots=7-XKDvzRST&sig=ACfU3U1bTRgtNq__dC7Kc0x69pMiMGagVQ&hl=en&sa=X&ved=2ahUKEwipoLi2x4_4AhXWFzQIHYVqAjoQ6AF6BAgcEAM#v=onepa.
United States Geological Survey, 2020, President Proposes $971.2 Million FY 2021 Budget for USGS:, https://www.usgs.gov/news/president-proposes-9712-million-fy-2021-budget-usgs (accessed February 2021).
VanValkenburgh, P., Cushman, K.C., Butters, L.J.C., Vega, C.R., Roberts, C.B., Kepler, C., and Kellner, J., 2020, Lasers Without Lost Cities: Using Drone Lidar to Capture Architectural Complexity at Kuelap, Amazonas, Peru: Journal of Field Archaeology, v. 45, p. S75–S88, doi:10.1080/00934690.2020.1713287.
Varnes, D., 1978, Slope Movement Types and Processes:,

http://onlinepubs.trb.org/Onlinepubs/sr/sr176/176-002.pdf.
Volkwein, A., Schellenberg, K., Labiouse, V., Agliardi, F., Berger, F., Bourrier, F., Dorren, L.K.A., Gerber, W., and Jaboyedoff, M., 2011, Rockfall characterisation and structural protection - A review: Natural Hazards and Earth System Science, v. 11, p. 2617–2651, doi:10.5194/nhess-11-2617-2011.
Vorpahl, P., Elsenbeer, H., Märker, M., and Schröder, B., 2012, How can statistical models help to determine driving factors of landslides? Ecological Modelling, v. 239, p. 27–39, doi:10.1016/j.ecolmodel.2011.12.007.
Wachal, D.J., and Hudak, P.F., 2000, Mapping landslide susceptibility in Travis County, Texas, USA: GeoJournal, v. 51, p. 245–253, doi:10.1023/A:1017524604463.
Wang, B., Ruel, M., Couture, R., Bobrowsky, P.T., and Blais-Stevens, A., 2012, Review of existing landslide guidelines National technical guidelines and best practices on landslides:, doi:10.4095/289864.
Wubalem, A., 2021, Landslide Inventroy, Susceptibility, Hazard and Risk Mapping:, doi:10.5772/intechopen.100504.

Appendices

Disclaimer

This thesis and its associated data and models are meant for research purposes only. These models and workflows were created as an isolated susceptibility case study for a few sites and are not a substitute for hazard or risk assessment analysis. The authors and contributors disclaim responsibility or liability for any injury to people or property resulting from any ideas, instructions, methods, or products referred to in this thesis.

Appendix I LiDAR Tools Workflow

Before opening LiDAR tools make sure the SBET files are in the same folder as the "lidar.pcap.idx"

Step 1
Select the "lidar.pcap.idx" for the site as the "input file"

Step 2
Choose your output file destination and name in the "output file" box. Make sure that the output file format is a LAS file.

Step 3
Change the "From:" and "To:" box values to reflect the start and end of data collection at the site.

Step 4
Change the Roll to 86.8 and the Pitch to 0.12

Step 5
Make sure the boxes for "right positive", "Northeast positive", "use post process file", "use pps.txt", and "save timestamps" are checked on. Leave the GPS Offsets set to zero.

Step 6
Click on the "LiDAR rotation, offsets and filters" tab. The following settings should be shown: "Laser angle rotation (deg)" set to 0, "Rotational offset (deg)" set to -90, Minimum Rotational angle (deg) set to 0, "Maximum rotational angle (deg)" set to 360, "Minimum Distance (m)" set to 1, "Minimum laser angle (deg)" set to -20, "Maximum laser angle (deg)" set to 20, and "Maximum Intensity" set to 128.

Step 7
Click the start button

Appendix II Strip Align and LASTools Workflow for Headwall Processing

---

Create file folders for cuts, laz, po, products, results, and temp (these will be used for outputs in the code below). Place all of your SBET files in the "po" file. Make sure your LAS file has the exact same name as your SBET file. Make Sure a channel map file is also in the directory.

Open powershell window in the directory you will be working out of (ctrl +shift+rt click mouse)

Step 1 (LAStools)
sets global encoding and shift gps timestamps to Adjusted,
Type in:
las2las -i *.las -set_global_encoding_gps_bit 1 -translate_gps_time -1000000000 -set_version 1.4 -set_point_type 6 -set_ogc_wkt -olaz -odir .\laz

Step 2 (Stripalign - cut swaths)
This cuts the flight into individual strips
Type in:
stripalign -UAS -cut -cut_buf 3 -po .\po\(flightline).out -i .\laz\(flightline).laz -T .\temp -O .\cuts -lax_append

Insert your file name in place of "(flightline)", for example \po\Kootenai_Site1.out -i

**command -cut needs only one PO file, do one flightline at a time with this command

***Inspect the cut swaths with lasview -i *.laz

Step 3 (Stripalign - align swaths):
This realigns the cut swaths
Type in:
stripalign -align -UAS -x 2 -i .\cuts*.laz -po .\po*.out -split ud 4 4chan.map -ics -O .\results\ -rmap -zmap -dmap -M -sub 2 -lax_append -full -qc -merge -T .\temp -ot -oa -op -opo -c

Step 4 (index- the results)
Adds indexing information
Type in:
lasindex
Use the default settings with the exception of:
-run on all cores -1 -check "verbose"
-select mobile or UAS-check "append to LAS

Step 5 (break the site up into tiles)
Lastile

Use the default settings with the exception of:
-run on all cores -1 -check “verbose” -set an output file location
-set the tile size to 100 -set the buffer to 10
-set an output file location

Step 6 (classify the noise)
Type in:
Lasnoise
Use the default settings with the exception of:
-run on all cores -1 -check “verbose” -set an output file location

Step 7 (classify ground points)
Type in:
Lasground
Use the default settings with the exception of:
-run on all cores -1 -check “verbose” -set an output file location
-select “wilderness” or “nature” -select “ultra” -check “compute height”
Before Pressing Start: In the command window add a space then “-all_returns” to make sure you are not only getting the second return which is the default.

Step 8 (classify the vegetation points)
Type in:
Lasclassify
Use the default settings with the exception of:
-run on all cores -1 -check “verbose” -set an output file location
-select “ignore low noise (7)” -set the ground offset to1

Step 9 (remove the buffers)
Type in:
Lastile
Use the default settings with the exception of:
-run on all cores -1 -check “verbose” -set an output file location
-Check “remove buffer points”

Step 10 (Rerun las noise to eliminate high noise)
Type in:
Lasnoise
Use the default settings with the exception of:
-run on all cores -1 -check “verbose” -set an output file location
-set the step value to 1 -set the nearest neighbor value to 20

Step 11 (edit the tiles)
Type in:
Lasview

In las view click “process select file”, now you go through the tiles along the edge of the site and manually reclassify incorrectly classified or edge noise. For this study we reclassified noisy ground points as unclassified (1). Save the edited layer as a “.lay” file.

Hot keys for editing:
-Space bar: switch between pan, translate, zoom, and tilt modes
-click and drag the mouse up and down to zoom
-<e> enter edit mode -<s> save as “.lay”
-<g> shows ground points -<t> triangulate ground points -<v> shows vegetation
-<a> shows all points -hold shift <t> to un triangulate
-rt click mouse scroll to reclassify points, select new class, <r> to reclassify points

Step 12 (Convert “.lay” File to “.laz”)
This next command converts all the “.lay” files to *_1.laz”
Type in:
Laslayers -i *.laz -ilay -olaz
After running this tool you need to go back through and delete the original “.laz” files for the tiles you edited. Delete the file right above any that end in “_1.laz”
From this point you can either export as a point cloud (Step 12A) or as a DEM/DSM (Step 12b)

Step 13A (merge the tiles together)
To export the site as a complete point cloud you need to merge the tiles together. And export as a “.laz” or “.las” file.
Type in:
Lasmerge
Use the default settings with either laz or las selected

Step 13B (create DEM and DSM)
To generate a DEM of the site the blast2DEM is used.
Type in:
blast2dem
Use the default settings with the exception of:
-run on all cores -1 -check “verbose” -set an output file location
-Set the step value to the scale you want (0.10 =10 cm, 0.5 = 50 cm)
-check “merge into one file”
-set the output to “tiff”
Before Pressing Start: In the command window add a space then “-keep_class 2” to make sure you are only getting the ground points.
To generate a DSM use the same workflow but type “-keep_class 2 3 4 5” this limits the points to just vegetation and ground.

Appendix III M3C2 and Volume Calculation in Cloud Compare

Open Cloud Compare and load in the two DEM Point clouds

Click "apply all" on the first pop up dialog box

On the second dialog box, make sure the box that says "preserve global shift" is checked off before selecting "apply all".

Part I Align the two point clouds

1. Once both point clouds are loaded in use the min-max tool to export just the ground points (class 2)
2. Since the two clouds are closely aligned already, simply select both layers and click on the fine registration tool under "Tools>Registration>Fine Registration (ICP)"
3. In the pop up window the 2017 point cloud will be the reference cloud, under the parameters window select number of iterations. In this study 10,000 iterations were used for the Deep Creek and Kootenai River site while 20,000 iterations were needed for the Moyie site due to the sparseness of the dense clouds. The percent overlap was adjusted for each site; Deep creek had a 40% overlap, Moyie had a 20% overlap, and Kootenai river had a 15%. The box for adjust scale was checked in each case. Under the research tab the random sampling limit was increased to 2 million points, the rotation was xyz, and enable farthest points removal was checked.
4. Record the final RMS error

Part II Run M3C2

1. Select the newly registered point clouds and click on the M3C2 plugin
2. In the pop up window select the 2017 cloud as the reference cloud
3. Under the main parameters tab change the “Normals” scale and “Projection” scale to 1, Then change the “max depth” to either 1 or 2 depending on the amount of change that you are expecting to see.
4. Check the box for registration error and input the RMS error from the fine registration
5. Instead of subsampling cloud 1 you want to select use cloud 1
6. Under the normal tab select multiscale
7. Under the output tab check both boxes for standard deviation and point density information
8. Leave everything else as default.

Part III Volume Calculation

1. When selecting an area to calculate the volume over make sure you are perfectly nadir in your view of the site
2. Highlight layers for both years and use the segmentation tool to outline the area of interest
3. Go to Tools>Volume> 2.5D volume
4. Set the 2017 layer as the ground layer and the 2021 layer as the ceiling
5. Change empty cells to interpolate
6. Change the step to 0.15 and the projection to z
7. Click update grid
8. Take screen shot of result

Part IV Exporting M3C2 layers into ArcGIS Pro

1. Highlight the final point cloud and select the rasterize tool.
2. In the rasterize window:
    a. Change “step” to 1 m
    b. The “active layer” can be either significant change or M3C2
    c. The “projection direction” should be Z
    d. “cell height” is minimum and interpolate SF is left as “average value”
    e. Empty cells should be left empty
    f. Click on update grid
    g. Select “Mesh”
    h. Select “Raster”
    i. In the pop up window check the boxes for “Export heights” and “Export all scalar fields” before clicking “OK”
3. Once the geotiff is created load it into ArcGIS Pro selecting the options to calculate statistics and build pyramids
4. You will need to use the “Define Projection Tool” to define the coordinate system as WGS 1984 UTM 11N
5. Since the exported raster will show up as a multiband raster the “Make Raster Layer” tool to create individual rasters for the M3C2 and Significant Change layers
6. These rasters will be very large and ArcGIS may have trouble displaying them, in order to improve the display the “Extract by Mask” tool to cut the larger raster into a more easily displayed size that focuses on the areas of interest

Appendix IV Data Layers in ArcGIS Pro

1. Upload both the DEM and DSM tiff files into ArcGIS Pro
    a. Build pyramids and calculate the statistics

2. Run the fill tool on both the DEM and DSM, with a z limit of 1

3. Save all layers you generate in a TIFF Format

4. Run the hillshade tool on each of the clipped DEMs
    a. Set the "Azimuth" to 315, "Altitude" to 45, and "z factor" to 1

5. Generate the canopy height model using raster calculator to subtract the DEM from the DSM

6. Open the Surface Parameters to create a slope layer with the DEM as the input raster, "Quadratic" as the local surface type, a minimum neighborhood distance of 1 m, and z unit of meter. The box for "use adaptive neighborhood" should be unchecked.

7. Using the Surface Parameters tool generate the aspect layer with the DEM as the input raster, "Quadratic" as the local surface type, a minimum neighborhood distance of 1 m, and z unit of meter. The box for "use adaptive neighborhood" should be checked.

8. With the reclassify tool change the values of the aspect layer so the southern facing slopes have a value of 1 and all other aspects have a value of 0.

9. With the Surface Parameter tool create two curvature layers: plan curvature, and profile curvature used the DEM as the input layer, "Quadratic" as the local surface type, a minimum neighborhood distance of 1 m, and z unit of meter. The box for "use adaptive neighborhood" should be unchecked.

10. The DEM is then input into the flow direction tool. The flow direction type is D-infinity and the box that states "force all edge cells to flow outward" is unchecked.

11. The next step is to calculate the flow accumulation for the site. The flow accumulation was calculated using the flow direction layer as the input a D-infinity flow direction type with the output data type of "float"

Run everything through OBIA in eCognition – view results. If desired and for final products do the following.

12. Create a polygon class feature for the site boundary that masks out the areas where the dense cloud is really sparse

13. Now that all of the layers have been created they need to be exported as TIFF files. This is done by using the Extract by Mask tool with the site boundary as the mask and each layer as an input. When selecting the output location make sure that the output format is TIFF.